

**Corrosion Inspection in High Temperature Surfaces  
using EMAT Technology**

**Bernardo Filipe Alves Vicente Farias de Sousa**

Thesis to obtain the Master of Science Degree in  
**Mechanical Engineering**

Supervisor: Prof. Maria Luisa Coutinho Gomes de Almeida

**Examination Committee**

Chairperson: Prof. Rui Manuel dos Santos Oliveira Baptista

Supervisor: Prof. Maria Luisa Coutinho Gomes de Almeida

Members of the Committee: Prof. Telmo Jorge Gomes dos Santos

Eng. José Pedro dos Santos Pereira de Sousa

**June 2019**



# Acknowledgments

First, I would like to thank my parents and near family, who tried their best to give me the very basis for this work to be done, through discipline, through control, through workforce and through motivation, because as someone said to me one day, “It takes work to have Luck”.

Then, I would like to thank all my teachers, for opening the doors to Knowledge. Not all lessons are easy to learn, but fortunately, one of the most profound laws of life is that “patience pays”.

And before going further, I would like to thank all my friends – the dear, the not so dear, the long gone and the long forgotten, because for every single one there was at least one story, and for every single story there was at least one meaning.

I would like to thank Prof. Luisa Coutinho, for establishing the necessary bridges between me and *ISQ Group*, and for all the support during this journey.

I would like to thank all *ISQ* members, who provided the necessary conditions for the following work to be created: Dr. Ana Cabral, Eng. Hugo Carrasqueira, Eng. Gonçalo Silva, Eng. Liliana Silva, Eng. David Santos. And specially Eng. José Pedro Sousa, a true leader, for all the dedication and endeavour – you taught me much more than Engineering.

And last but not least, to my dear colleagues of *IST*, Eng. Ana Albuquerque and Eng. João Lameiras, without whom the academic path would have been significantly more difficult.



## Abstract

The present work, developed by *IST* in collaboration with *ISQ*, aimed create a solution to inspect Carbon Steel specimens of thicknesses between 10 mm and 30 mm, for corrosion mapping of defects of  $\varnothing 16$  mm minimum at critical depths, and thickness discontinuities of 4 mm minimum, in bottom, vertical and bottom-up positions, as well as circular and axial inspections on tubes of  $\varnothing 350$  mm minimum, between 25 °C and 400 °C, for the Petrochemical Industry.

The created prototype, *EMAT Heat Inspection*, consisted of a scanner functioning with an EMAT probe (*Innerspec High Temperature Sensor SH Spiral*) and an encoder (*Hengstler RI32-O/360AR.14KB*) that was air cooled and connected to a dedicated device, *Innerspec PowerBox H*, in order to generate corrosion mapping reports.

Proper test apparatus and procedures were also created to validate the prototype, studying the amplitude behaviour of back wall and defect signal echoes for different testing blocks regarding desired temperatures.

Despite the natural attenuation along increasing temperatures due to scattering effects caused by defect geometries, vibrational interactions between travelling ultrasonic waves and the microstructures of Carbon Steel, and the different behaviour of cementite vibrational interactions with the ultrasonic waves after reaching its Curie Temperature, the developed prototype fulfilled all the customer requirements, which validated its capacity to inspect, on the given conditions, flaws due to uniform corrosion and erosion corrosion, and defects of critical depth due to pitting corrosion, generating corrosion mapping reports at service temperatures from 25 °C to 400 °C in a practical and reliable manner.

## Keywords

EMAT, High Temperature, Corrosion, Attenuation, Non Destructive Testing.



## Resumo

O presente trabalho, realizado pelo *IST* e *ISQ*, teve como objectivo desenvolver uma solução para inspeccionar espécimens de Aço Carbono de espessuras entre 10 e 30 mm, para mapeamento de corrosão de defeitos com  $\varnothing 16$  mm mínimo, a profundidades críticas, descontinuidades de espessura mínima de 4 mm, posições ao baixo, na vertical e ao alto, e inspecções circunferenciais e axiais a tubos de  $\varnothing 350$  mm mínimo, entre 25 °C e 400 °C para a Indústria Petroquímica.

O protótipo criado, *EMAT Heat Inspection*, consistiu num scanner composto por uma sonda EMAT (*Innerspec High Temperature Sensor SH Spiral*) e um encoder (*Hengstler RI32-O/360AR.14KB*), arrefecido a ar e ligado ao equipamento *Innerspec PowerBox H*, gerando relatórios de mapeamento de corrosão.

Foi projectado e construído um equipamento específico para validar o protótipo, estudando o comportamento da amplitude de ecos de fundo e de defeitos em vários blocos de teste face às temperaturas desejadas.

Os estudos revelaram que as ondas ultrasónicas sofrem atenuação natural ao longo de temperaturas crescentes, devido a efeitos de dispersão causados pela geometria dos defeitos, interacções vibracionais entre as ondas vigentes e as microestruturas do Aço Carbono, e o diferente comportamento entre microestruturas da cementite e as ondas após a Temperatura de Curie.

O protótipo cumpriu todos os requisitos, validando a sua capacidade para inspeccionar, nas condições estipuladas, defeitos de corrosão uniforme, corrosão erosiva e corrosão por pitting, gerando relatórios de mapeamento de corrosão a temperaturas de serviço entre 25 °C e 400 °C de uma forma prática e fiável.

## Palavras Chave

EMAT, Alta Temperatura, Corrosão, Atenuação, Ensaio Não Destrutivo.

# Contents

- 1. Introduction ..... 1
  - 1.1. Economic impact of corrosion incidents..... 1
  - 1.2. Industrial disasters due to corrosion in high temperature structures ..... 1
  - 1.3. Challenge Assessment and Work Methodology ..... 3
- 2. State of the Art ..... 5
  - 2.1. Main corrosion defects at high temperature structures ..... 5
    - 2.1.1. Uniform Corrosion ..... 5
    - 2.1.2. Pitting Corrosion..... 5
    - 2.1.3. Erosion Corrosion ..... 6
    - 2.1.4. Cavitation Corrosion ..... 6
    - 2.1.5. Microbiologically Influenced Corrosion ..... 7
  - 2.2. Technologies used in high temperature Carbon Steel inspections..... 7
    - 2.2.1. Conventional Ultrasonic Testing ..... 8
    - 2.2.2. Eddy Current ..... 11
    - 2.2.3. EMATs - Electromagnetic Acoustic Transducers ..... 12
  - 2.3. Market survey ..... 18
- 3. Design and construction of *EMAT Heat Inspection* prototype ..... 24
  - 3.1. Scanner prototype buildup ..... 24
    - 3.1.1. Presentation of the main components..... 24
    - 3.1.2. Connections schematics..... 25
    - 3.1.3. Scanner prototype design..... 26
    - 3.1.4. Scanner prototype production..... 31
  - 3.2. Scanner prototype validation..... 33
    - 3.2.1. Construction of validation equipment ..... 33
    - 3.2.2. *PowerBox H* set up ..... 36
    - 3.2.3. Probe and Encoder calibration..... 40
    - 3.2.4. Prototype Testing Plan ..... 41
    - 3.2.5. General Test Procedure ..... 42
    - 3.2.6. Study of results..... 43
- 4. Conclusion ..... 57
- 5. Marketing and suggestions for future work ..... 59
- 6. References ..... 60
- 7. Annexes ..... 65
  - 7.1. Results from validation tests ..... 65
  - 7.2. *Innerspec* probe Exploded View..... 69
  - 7.3. *EMAT Heat Inspection* Marketing Brochure ..... 70



7.4. *EMAT Heat Inspection User's Guide*.....72

# List of Figures

Fig. 1 - Image from the *Santa Cruz Sentinel* newspaper (8th May 1988) reporting what happened in Norco [11]. ..... 2

Fig. 2 - Fire in *Silver Eagle* refinery after hydrogen explosion [12]. ..... 2

Fig. 3 - Left: The fire being extinguished at *Chevron* refinery [15]. Right: The big cloud of smoke that emerged after the refinery explosion [16]. ..... 3

Fig. 4 - Left: different shapes of pitting corrosion defects in cross sectional view [26]. Right: pitting corrosion due to dissolved oxygen in Carbon Steel boiler tube [21]. ..... 5

Fig. 5 - Erosion corrosion in the middle of a reducer [27]. ..... 6

Fig. 6 - Cavitation corrosion in a Carbon Steel pipe of a steam condensate system (detail of the upper part) [28]. ..... 6

Fig. 7 - Massive microbial corrosion on a pump housing [30]. ..... 7

Fig. 8 - Left: Longitudinal wave. Right: Transversal wave (adapted from [34];  $\lambda$  corresponds to the respective wavelengths) ..... 9

Fig. 9 - General representation of the basic functioning principle of UT Pulse Echo inspection [32]. .. 10

Fig. 10 - a) UT Pulse Echo inspection with no defects; b) UT Pulse Echo inspection with a defect wider than the ultrasonic beam (adapted from [39]). ..... 10

Fig. 11 - Scheme of a C-Scan representation (adapted from [34]). ..... 10

Fig. 12 - General representation of Eddy Current generation on a given test specimen by a coil in AC (adapted from [35]). ..... 11

Fig. 13 - Left: scheme of influence of the magnetic field generated by a vertical bias magnet on an inspected material (adapted from [41]). Right: scheme of generation of Eddy Currents on a material by a meander coil (adapted from [44]). ..... 13

Fig. 14 - Generation of a SH Wave (adapted from [46]). Note that the Eddy Current density vector is normal to the image plane. .... 14

Fig. 15 - Generation of a Longitudinal Wave (adapted from [46]). Note that the Eddy Current density vector is normal to the image plane. .... 14

Fig. 16 - Simultaneous generation of SH and L waves with a periodical bias magnet and a racetrack coil (adapted from [41]). Note that the coil and Eddy Current density propagate in a direction normal to the reading plane. .... 15

Fig. 17 - Scheme of the magnetostrictive effect on materials when exposed to an external magnetic field H, explained with a chain of magnets connected by elastic springs [41]. ..... 15

Fig. 18 - Magnetostrictive effect in polycrystalline materials subjected to an external magnetic field [41]. ..... 16

Fig. 19 - Example of SH wave generation in an inspected material due to magnetostrictive force, with a periodical bias magnet and racetrack coil (adapted from [41]). ..... 16

Fig. 20 - Left, up: *RMS2 450* equipment. Left, down: *RMS2 ARC 24-36* equipment [57]. Right: industrial application of *RMS2 450* [58]. ..... 19

Fig. 21 - From left to right: Phoenix SSHTC 4/10 and SSHTC 4/6 - High Temperature Twin Crystal Compression Wave Transducers [62]. ..... 19

Fig. 22 - Left: scheme of permanent magnet and spiral coil (adapted from [50]); N and S stands for North and South poles of the magnet. Right: side view of Lorentz Force generation with permanent magnet and spiral (or pancake) coil (adapted from [41]). ..... 20

Fig. 23 - Ultrasonic beam profiles of *Innerspec High Temperature Sensor SH Spiral* [64]. X1 stands for length, X2 for width and X3 for thickness. The colour grade chart (which goes from 0% to 100%) is related to the ultrasonic signal strenght. .... 20

Fig. 24 - Left: *PowerBox H* frontal view [51]. Right: *Powerbox H* used with an arness [67]. ..... 21

Fig. 25 - *Innerspec High Temperature Sensor SH Spiral* in different views [64]. ..... 21

Fig. 26 - *Eddyfi Lyft* with *Single Element PEC Probe* being used at on-site inspections [70]. ..... 22

Fig. 27 - *Hengstler RI32-O/360AR.14KB* encoder [75]. ..... 24

Fig. 28 - General schematic of *EMAT Heat Inspection* equipment. .... 25

Fig. 29 - Connection schematic with information on connectors and cables (not on scale). ..... 25

Fig. 30 - Cylindrical grip with thumb pointing in axial direction (adapted from [82]). ..... 27

Fig. 31 - Left: preliminary drawing of the different handle parts. Right: preliminary drawing of handle subassembly (invisible lines are present in order to better perceive that the handle was hollow).....	27
Fig. 32 - Left: first angle view of casing prototype drawing. Right: isometric view of casing prototype drawing.....	27
Fig. 33 - Preliminary drawings of the different casing parts. Left, up: Aluminium top. Left, down: Aluminium base. Middle: two Stainless Steel sheet metal parts. Right: casing subassembly, held together with screws.....	28
Fig. 34 - Scheme of probe cup functioning principle.....	29
Fig. 35 - Cup subassembly exploded view. 1: probe; 2: <i>Lemo FGG.0B.302.CLAD52Z</i> plug; 3: nuts to fix the cup; 4: screws to fix the cup; 5: cup; 6: nuts to fix the top screws; 7: top screws to fix the springs; 9: L air connector; 10: set screws to fix the springs.....	29
Fig. 36 - Drawing of the different cup parts.....	29
Fig. 37 - Exploded view of the encoder subassembly. 1: encoder; 2: encoder holder; 3: plug which fits in the encoder spindle; 4: encoder holder lid; 5: screws to fix the plug; 6: screws to fix the encoder lid; 7: o-ring; 8: screws to fix the encoder holder.....	30
Fig. 38 - Simplified scheme of scanner section including the encoder, o-ring and coupled wheel.....	30
Fig. 39 - Scheme of wheels subassembly in exploded view. 1: wheel supports; 2: spindles; 3: normal wheel; 4: wheel to couple with encoder; 5: screws to fix the wheel supports; 6: retention rings; 7: roller bearings.....	30
Fig. 40 - Right and left: two external views of the final scanner prototype model. Middle: internal view of the final scanner prototype model (made with <i>Solidworks 2017</i> software).....	31
Fig. 41 - From left to right: welding of the handle base; welding of the handle rods; welding of the casing middle; welding of the cup top; welding of the cup base.....	32
Fig. 42 - Left: the casing middle frame after being welded. Center: the casing middle frame during the passivation process. Right: the casing middle frame after the passivation process.....	32
Fig. 43 - Peli 1610 Case.....	32
Fig. 44 - Left: scanner prototype inside view. Center: the equipment in its respective travelling case. Right: scanner prototype outside view.....	33
Fig. 45 - Left: various testing blocks on top of the heating box. Right: structure of aluminium profiles on the heating box.....	34
Fig. 46 - Drawing scheme of the hole configuration for all 1 <sup>st</sup> category inspection blocks (bottom view); the holes near the edges were made to screw the bars on the heating box.....	35
Fig. 47 - Drawing scheme representation of the 2 <sup>nd</sup> category inspection block (side view).....	35
Fig. 48 - Drawing scheme of 3 <sup>rd</sup> category validation block (bottom view).....	35
Fig. 49 - Left: printscreen of a typical TX/RX menu of <i>Innerspec PowerBox H</i> . Right: probe datasheet chart of signal response (mV) and frequency (kHz) for <i>Innerspec High Temperature Sensor SH Spiral [74]</i> .....	36
Fig. 50 - Left: printscreen of typical <i>DSP/Gates</i> menu of <i>Innerspec PowerBox H</i> . Right: printscreen of typical <i>Gate 2 Parameters</i> menu of <i>Innerspec PowerBox H</i> .....	38
Fig. 51 - Printscreen of A plus C Scan of the 10 mm block at 50 °C performed with <i>Innerspec PowerBox H</i> , where the green gate (First Peak) can be seen on the A-Scan.....	38
Fig. 52 - Printscreen of typical <i>DAQ</i> menu of <i>Innerspec PowerBox H</i> .....	39
Fig. 53 - Printscreen of typical <i>Display</i> menu in <i>Innerspec PowerBox H</i> .....	39
Fig. 54 - Simplified scheme of the first calibration position for 1 <sup>st</sup> category 10 mm block (bottom view).....	41
Fig. 55 - Temperature check using the thermocouple.....	43
Fig. 56 - Inspection on a given block.....	43
Fig. 57 - Left: A+C Scan of 20 mm block of the 1 <sup>st</sup> category at 125 °C using <i>Innerspec PowerBox H</i> . Right: A+C Scan of 25 mm block of the 1 <sup>st</sup> category at 200 °C using <i>Innerspec PowerBox H</i> .....	44
Fig. 58 - Amplitude vs. Temperature for the 1 <sup>st</sup> category blocks Ø12 mm defect echo.....	45
Fig. 59 - Amplitude vs. Temperature for the 1 <sup>st</sup> category blocks Ø14 mm defect echo.....	45
Fig. 60 - Amplitude vs. Temperature for the 1 <sup>st</sup> category blocks Ø16 mm defect echo.....	46
Fig. 61 - Amplitude vs. Temperature for the 1 <sup>st</sup> category blocks Ø18 mm defect echo.....	46
Fig. 62 - Amplitude vs. Temperature for the 1 <sup>st</sup> category blocks back wall echo.....	47
Fig. 63 - Phase diagram of iron-iron carbide, also known as cementite [106].....	48

Fig. 64 - SNR vs. Temperature for the 1<sup>st</sup> category blocks Ø12 mm defect echo, along with the respective rejection value. .... 51

Fig. 65 - SNR vs. Temperature for the 1<sup>st</sup> category blocks Ø14 mm defect echo, along with the respective rejection value. .... 51

Fig. 66 - SNR vs. Temperature for the 1<sup>st</sup> category blocks Ø16 mm defect echo, along with the respective rejection value. .... 52

Fig. 67 - SNR vs. Temperature for the 1<sup>st</sup> category blocks Ø18 mm defect echo, along with the respective rejection value. .... 52

Fig. 68 - SNR vs. Temperature for the 1<sup>st</sup> category blocks back wall echo, along with the respective rejection value. .... 53

Fig. 69 - A+C Scan of 2<sup>nd</sup> category block at 400 °C using *Innerspec PowerBox H*. .... 54

Fig. 70 - A+C Scan of 3<sup>rd</sup> category block at 100 °C using *Innerspec PowerBox H*. .... 55

Fig. 71 - Left: *EMAT Heat Inspection* prototype on a OD 400 mm pipe. Right: *Emat Heat Inspection* prototype on upside-down test (same pipe as left image). .... 56

Fig. 72 - Amplitude vs. Temperature for the 2<sup>nd</sup> category block back wall echo. .... 67

Fig. 73 - SNR vs. Temperature for the 2<sup>nd</sup> category block back wall echo. .... 67

Fig. 74 - Amplitude vs. Temperature for 3<sup>rd</sup> category block defects and back wall echo. .... 68

Fig. 75 - SNR vs. Temperature for 3<sup>rd</sup> category block defects and back wall echo. .... 68

# List of Tables

Table 1 – Arrangement of results for 1<sup>st</sup> Category Blocks..... 44

Table 2 - Linear regression equations of the aforementioned amplitude versus temperature charts for various defect and back wall echoes, at different nominal thickness blocks..... 48

Table 3 - Percentual share over the real defect diameter of the difference between obtained and real flaw diameters for 10 mm block of the first category. .... 50

Table 4 - Percentual share over the real defect diameter of the difference between obtained and real flaw diameter for 15 mm block of the first category..... 65

Table 5 - Percentual share over the real defect diameter of the difference between obtained and real flaw diameter for 20 mm block of the first category..... 65

Table 6 - Percentual share over the real defect diameter of the difference between obtained and real flaw diameter for 25 mm block of the first category..... 66

Table 7 - Percentual share over the real defect diameter of the difference between obtained and real flaw diameter for 25 mm block of the first category..... 66

## Acronyms

<b>IST</b>	-	Instituto Superior Técnico
<b>ISQ</b>	-	Instituto de Soldadura e Qualidade
<b>EMAT</b>	-	Electromagnetic Acoustic Transducer
<b>UT</b>	-	Ultrasonic Testing
<b>USA</b>	-	United States of America
<b>NDT</b>	-	Non Destructive Testing
<b>KO</b>	-	Knockout
<b>SH</b>	-	Shear Horizontal
<b>LW</b>	-	Longitudinal Wave
<b>L</b>	-	Longitudinal
<b>AC</b>	-	Alternating Current
<b>OD</b>	-	Outer Diameter
<b>NPT</b>	-	National Pipe Thread
<b>SNR</b>	-	Signal-to-Noise Ratio

# Nomenclature

$v_a$	-	Acoustic Velocity	-	m/s
$f$	-	Frequency	-	Hz
$\lambda$	-	Wavelength	-	m
$V_L$	-	Longitudinal Wave Velocity	-	m/s
$V_T$	-	Shear Wave Velocity	-	m/s
$E$	-	Young Modulus	-	$\text{N/m}^2$
$\rho$	-	Density	-	$\text{Kg/m}^3$
$\nu$	-	Poisson Ratio	-	
$\vec{B}$	-	Magnetic Field Density	-	T
$\delta$	-	Electromagnetic Skin Depth	-	m
$\omega$	-	Angular Frequency	-	rad/s
$\mu$	-	Magnetic Permeability	-	H/m
$\sigma$	-	Electrical Conductivity	-	$(\Omega \cdot \text{m})^{-1}$
$\vec{J}$	-	Current Density	-	$\text{A/m}^2$
$\vec{F}_L$	-	Lorentz Force	-	N
$H$	-	Magnetic Field Strength	-	A/m
$G_R$	-	Received Gain	-	dB
$P_I$	-	Incident Acoustic Pressure	-	Pa
$P_R$	-	Reflected Acoustic Pressure	-	Pa
$SNR$	-	Signal-to-Noise Ratio	-	
$A_S$	-	Signal Peak Amplitude	-	%
$A_N$	-	Noise Peak Amplitude	-	%
$A_b$	-	Gain Basis Amplitude	-	%
$G_b$	-	Gain Basis	-	dB
$A_o$	-	Original Amplitude	-	%
$G_b$	-	Original Gain	-	dB
$A_e$	-	Edge Echoes Amplitude	-	%
$A_m$	-	Maximum Echo Amplitude	-	%
$G$	-	Gain (6 dB Method)	-	dB
$P_s$	-	Percentual Share	-	%
$D_O$	-	Obtained Defect Diameter	-	mm
$D_R$	-	Real Defect Diameter	-	mm
$SNR_{dB}$	-	Signal to Noise Ratio (in dB)	-	dB
$A_{AV}$	-	Average of Noise Peaks Amplitude	-	%
$A_i$	-	Signal Amplitude at Block of Nominal Thickness i	-	%
$T$	-	Temperature	-	$^{\circ}\text{C}$
$T_c$	-	Curie Temperature	-	$^{\circ}\text{C}$

# 1. Introduction

## 1.1. Economic impact of corrosion incidents

In a time when technology and industry are experiencing an exponential evolution, as the actual USA daily production of oil barrels nearly doubled since the last decade [1], it is important to address all the evitable losses which can slow down this expansion.

It is estimated that the annual global cost of corrosion is 2,16 trillion euros, and the adoption of corrosion control practices can translate in annual savings between 324 billion euros and 756 billion euros (between 15% and 35% of global annual cost). Nevertheless, these values do not include economical costs due to individual safety and environmental consequences [2].

And analysing just the oil and gas industry alone, the annual corrosion costs are estimated to be 1185 billion euros, of which 509 million euros are just for surface pipeline and facility costs, 400 million euros in downhole tubing expenses and 276 million euros in capital expenditures [3]. Surveys account that from 1988 to August 2008, in US, 18% of significant incidents in onshore and offshore pipelines were due to corrosion; in Canadian pipelines, from 2000 to 2006, corrosion ramps up to 50% of the incident causes; and in Europe, from 1970 to 2004, 15% to 17% of the pipeline incidents were also due to corrosion [4].

Now more than ever, with fierce markets and competition, every avoidable expense needs to be obliterated. Therefore, it is of major importance to bet in corrosion prevention. That would bring significant economical savings, and also obviate tragic accidents with possible structural, environmental and human losses.

## 1.2. Industrial disasters due to corrosion in high temperature structures

Despite companies being obliged to form and inform employees about the hazards and safety procedures on their working site, as well as accepting regular inspections by certified organisms, always ensuring safe working conditions [5], from time to time accidents caused by severe corrosion of high temperature structures can happen, being pertinent to remember some of the most tragic.

*Shell Oil Co.* refinery at Norco, Louisiana (USA) is located on the heavily industrialized corridor along the Mississippi River, between New Orleans and Baton Rouge. Running since 1929, nowadays it processes a total of 250 000 crude barrels and produces 170 000 gasoline barrels on a daily basis [6].

On 5<sup>th</sup> May, 1988, around 3:30h in the morning, a big calamity took place, as an enormous explosion and fire happened in the refinery. The blast was so strong it shattered windows in a 32 Km range up to New Orleans. Over 2500 citizens were evacuated, and out of 42 people injured, 19 of them were refinery workers, being one at critical condition with burns at around 75% of his body.

And worst of all, seven people who were in the refinery died. At first, only one of them was



declared dead, as the fire was so violent that the rescue team had to wait for 5:30h for it to calm down and go search for the other bodies [7][8][9].

Following further investigation, Occupational Safety and Health Administration of the USA Department of Labour concluded that the explosion and fire was due to corrosion of a Ø20,32 cm vapour line, causing a gas escape. The failure of this vapour line, (which was under 18,6 bar) released over 7711 Kg of hydrocarbon vapour for approximately 30 seconds, which probably ignited when in contact with a furnace [10]. The following Fig. 1 shows a newspaper from that time exposing what happened [11].



Fig. 1 - Image from the *Santa Cruz Sentinel* newspaper (8th May 1988) reporting what happened in Norco [11].

Another tragic accident occurred in Woods Cross, Utah, on the 4th November 2009. At *Silver Eagle* refinery, a leaking in a Ø25,4 cm hot pipe, which typically operated between 260 °C and 427 °C, led to a massive release of hydrogen that immediately caught fire and exploded, projecting four nearby workers to the ground, with burns in the face, neck, arms and hands (one has even suffered lung damage due to inhalation of hot air). The blast wave generated by the explosion damaged over one hundred houses, ripping one of them off its foundations [12][13]. Fig. 2 shows the fire that consequently spread in the refinery due to the explosion (as reported by [12]).

Posterior analysis revealed that the hydrogen leakage was due to severe corrosion along the pipe which was not inspected since the day it was installed in the facility, and ended up thinning over the years [14].



Fig. 2 - Fire in *Silver Eagle* refinery after hydrogen explosion [12].

But these types of accidents in refineries are not uncommon. On 6th August 2012, a ruptured pipe in *Chevron USA Inc.* refinery (Richmond, California) released high temperature gas oil which partially vaporized and ignited two minutes later, creating a fierce fire and a dense plume of black smoke which travelled to the vicinities (that can be seen on Fig. 3, as in [15] and [16] respectively).

Despite being no casualties, on the following weeks over 15 000 people sought medical treatment reporting breathing problems, chest pain, shortness of breath and sore throat.

Official investigation made by US Chemical Safety and Hazard Investigation Board (CSB)

concluded that the main cause for the pipe rupture was gradual thinning due to corrosion, and stated that it could be prevented if proper testing and procedures were conducted [17].



Fig. 3 - Left: The fire being extinguished at *Chevron* refinery [15]. Right: The big cloud of smoke that emerged after the refinery explosion [16].

As seen by these examples, corrosion plays an important role in structures specifically operating at high temperatures, and lack of proper inspection could cause serious accidents and calamities resulting in material, environmental and human losses. Those have been causes of major concern among companies, which now, more than ever, adopt a preventive approach in order to avoid major disasters.

### 1.3. Challenge Assessment and Work Methodology

As already mentioned, corrosion is one of the Petrochemical Industry's leading causes of equipment failure [18]. And also, the increased emphasis on minimizing production costs pulls companies to reduce their plant's maintenance period, and avoiding shutdowns, along with all their inherent high costs [19][20]. In order to effectively mitigate such occurrences, companies could bet in preventive actions, such as the regular conduction of Non Destructive Testing [21].

For that reason, the present work, developed by *IST (Instituto Superior Técnico)*, in collaboration with the *Non Destructive Testing Laboratory of ISQ (Instituto de Soldadura e Qualidade)*, aimed to create an appropriate solution for the increased customer demand to perform corrosion inspections in high temperature structures.

An appropriate prototype equipment, called *EMAT Heat Inspection*, using the Non Destructive Testing technology of Electromagnetic Acoustic Transducers, was developed, as well as all the necessary apparatus to perform various validation tests on *EMAT Heat Inspection*. Therefore, the prototype was tested to prove its capability to perform inspections in real Engineering context.

Customers wanted *ISQ* to perform corrosion inspections on Carbon Steel materials, fulfilling the following criteria:

- Detect defects with minimum diameter of 16 mm and depth of 50% of the nominal specimen thickness – this is the critical depth which determines the replacement of the inspected structure<sup>1</sup> – from 10 mm to 30 mm, up to 400 °C.

---

<sup>1</sup> The critical depth of corrosion flaws in inspected structures is usually a criterion derived from various factors such as the fluid or gas which it carries and the chosen material or structure geometry. Usually, the responsibility to stipulate its value is up to the manufacturer or the owner [116][117][118]. Nevertheless, there are certain codes which suggest good practices for the choosing of corrosion critical depths [119].

- Detect thickness discontinuities of at least 4 mm depth in structures of 10 mm nominal thickness up to 400 °C.
- Perform circumferential and axial inspections on pipes with a minimum outer diameter of 350 mm.
- Perform bottom, vertical and upside-down inspections.
- The production site won't need to be shut down in order to perform the testing.
- No more than 10 minutes of setup time.
- Minimum scanning speed of 15 mm/s.
- Generate Corrosion Mapping Reports (A-Scan and C-Scan).
- The inspection equipment must be portable enough to be taken to spaces of difficult access.

Therefore, the following Chapters describe the adopted process to address these challenges. First, a study over the main types of high temperature corrosion defects was performed (Chapter 2.1), as well as a study on the most adequate Non Destructive Testing Technologies used in that context (Chapter 2.2).

These studies created a basis to perform a market survey in order to find the most adequate equipment which satisfied *ISQ* customers' requisites (Chapter 2.3), but it was noted that none of the presented offers was fit to the task, so that the adopted solution was to create the *EMAT Heat Inspection* prototype which could perform the inspections on the given customers' conditions.

That being said, Chapter 3.1 was focused on the design and creation of the prototype, describing each component as well as its respective connections.

For validating *EMAT Heat Inspection*, proper equipment was also created, in order to perform various studies on prototype detectability and ultrasonic signal behaviour along increasing temperatures (Chapter 3.2).

In Chapter 4, the test results were then analysed, corroborating the prototype capability to perform corrosion inspections in high temperature structures, fulfilling all costumers conditions and creating a reliable competitive solution when compared with similar products already on the NDT market.

Some suggestions for future work were approached in Chapter 5. And finally, Chapter 7 presented some important annexes such as a User's Guide for *EMAT Heat Inspection* equipment, and a Marketing Brochure.

That being said, as a first step, it was important to acknowledge the most common corrosion-related defects which are behind the majority of failures on these kinds of industrial structures, so that a solution could be found.

## 2. State of the Art

### 2.1. Main corrosion defects at high temperature structures

A general and simple approach to the meaning of corrosion is that it's an environmental reaction which culminates in destructive attack of a metal [22]. Being the cause of many industrial accidents, it is important to briefly analyse some corrosion defects which can happen at high temperatures. As suggested on the previous chapter, this analysis will be focused on corrosion at high temperature in Carbon Steel, being one of the industry's most widely used materials, at a multitude of structures such as flow lines, injection lines, production separators and KO drums, for example [23], due to its cost, properties, ease of fabrication, availability and weldability [24].

#### 2.1.1. Uniform Corrosion

In this case the metal is evenly attacked over its entire surface, or at least most of it, as no portions of the metal surface are preferentially more corroded than others, and this process gradually thins the metal surface until eventual failure [22]. It is the most common form of corrosion [25], but fortunately, it's rate could be easily measured and predicted, making disastrous failures relatively rare [26].

#### 2.1.2. Pitting Corrosion

It is a localized form of corrosion with formation of cavities in the material, being more dangerous than uniform corrosion because it is more unpredictable and difficult to detect [26], due to the usual small sized defects, the varying depths and numbers of pits that may occur under identical conditions, and because they are often covered with corrosion products. Sometimes one single pit can lead to the failure of an entire system [25]. This kind is more prone to happen in liquid retaining or exclusion systems such as pipelines and tanks, for example [24]. Fig. 4, left shows typical variations in the cross sectional shape of pits (according to [26]), and Fig. 4, right shows an example of pitting corrosion on a Carbon steel Boiler Tube (as in [21]).

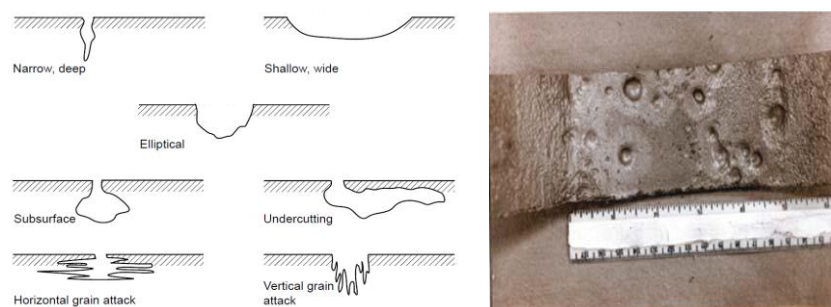


Fig. 4 - Left: different shapes of pitting corrosion defects in cross sectional view [26]. Right: pitting corrosion due to dissolved oxygen in Carbon Steel boiler tube [21].

### 2.1.3. Erosion Corrosion

This type is created by the movement of a corrosive liquid against the metal surface [22], being the cumulative damage created by corrosion reactions and mechanical effects [26]. The relative motion between the corrosive liquid and the metal surface, usually one of high velocity, induces mechanical wear and abrasion, which disembogues in accelerated material degradation [26], being this effects increased in the presence of turbulent flow, and two-phase fluid stream (i.e. with two of the three: solid, liquid or gas) [21].

As a consequence, the defects usually appear as grooves, waves, and valleys that have a pattern along the flow direction of the corroding fluid, and are found on equipments such as pipelines, reaction vessels and distillation columns, where high velocity streams and turbulence tend to happen [21]. As an example, Fig. 5 shows the presence of erosion corrosion in the middle of a reducer (according to [27]).



Fig. 5 - Erosion corrosion in the middle of a reducer [27].

### 2.1.4. Cavitation Corrosion

It occurs when the flow of a corrosive liquid creates localized lower pressure spots, leading to the formation of bubbles which produce shock waves and high-velocity microjets when the same bubbles collapse. These impacts cause mechanical damage due to continuous and local bombardment of the surface by the vapour bubbles, that is intensified by the corrosive effect of the liquid [21][22]. Fig. 6 shows the effect of cavitation in a steel pipe (according to [28]).

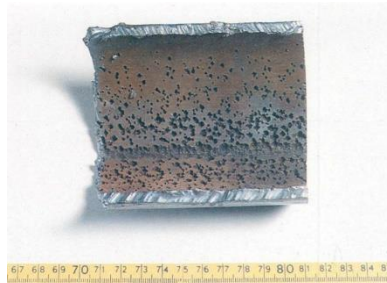


Fig. 6 - Cavitation corrosion in a Carbon Steel pipe of a steam condensate system (detail of the upper part) [28].

### 2.1.5. Microbiologically Influenced Corrosion

This kind of corrosion, as its name states, happens due to the influence of microorganisms and/or their metabolites. They usually form aggregated colonies on the material surface, creating corrosion cells which are the basis for accelerated attack [26]. These microorganisms have been reported to cohabit in structures above 100 °C and pH values of -1 [29]. Fig. 7 shows a case of massive microbial corrosion on a pump housing (as in [30]).

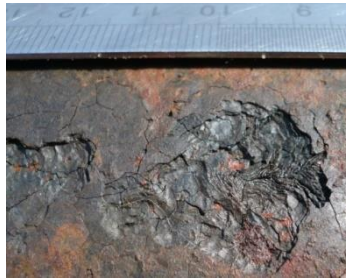


Fig. 7 - Massive microbial corrosion on a pump housing [30].

As could be seen, there are numerous corrosion processes that can happen in high temperature environments, leading to a multitude of defects which can cause numerous accidents. It was also known that the causes of most corrosion defects customers wanted to see monitored by ISQ were uniform corrosion, erosion corrosion and pitting corrosion.

Therefore, it is important to acknowledge the most prominent non destructive techniques which can address the challenge and conduct a proper inspection on these structures.

## 2.2. Technologies used in high temperature Carbon Steel inspections

Of all the Non Destructive Testing techniques, Conventional Ultrasonic Testing, Eddy Currents and advanced techniques such as Electromagnetic Acoustic Transducers were proven to be the most safe, versatile and portable to inspect corrosion defects [31].

Radiography is also a much used alternative, as it can evaluate the inside of complex, small parts, and by using real-time radiography, a portable form of radiographic technology which presents an instant image much like a video camera, one overcomes the problem of longer setup times that arose by the older models. But it still poses various disadvantages, as the process control and variance is more dependable on human factors than the aforementioned techniques; also, the possible use of radioisotope elements has great inherent hazards, therefore only fully trained and licensed personnel should work with it [32].

Therefore, the techniques which will be furtherly explained are Conventional Ultrasonic Testing, Eddy Currents and Electromagnetic Acoustic Transducers.

### 2.2.1. Conventional Ultrasonic Testing

Conventional Ultrasonic Testing takes advantage on the behaviour of ultrasonic waves, which have higher frequency than the common sounds a human hear can detect (usually 1 to 10 MHz, although used frequencies can be lower or higher depending on desired applications [33]) [32].

Traditionally, by using a transmitter of electric impulses on a certain transducer, the electric signals are converted into ultrasonic waves, which travel along a given homogeneous material at constant speed, given by the following formula [34]:

$$v_a = f \times \lambda \quad (1)$$

Being  $v_a$  the acoustic velocity,  $f$  the frequency and  $\lambda$  the wavelength of the ultrasonic wave [34]. They travel at straight motion until a discontinuity between mediums of different acoustic impedances is found. Then, ideally, a portion of the ultrasonic waves is transmitted through the respective interface and another is reflected [33][34][35]. The discontinuity's reflections, when received by the transducer, are converted to electric signals which, after being amplified and rectified by an amplifier, are transmitted to a proper device that allows the detection and localization of the source of reflection along the piece, based on information such as travel time (or time of flight) and propagation velocity [34]. For that reason, UT can provide quantitative data such as thickness of the inspected material, depth of a certain discontinuity and its respective size [33].

The condition of the material surface in contact with the probe determines how much sound is transferred. For that reason, certain standards of surface finish are required for the Ultrasonic Inspection to be efficiently performed (as an example, the surface should be clean and free of extensive corrosion products) [37].

Usually, the piece which is responsible for the conversion of electric signals into ultrasonic waves in conventional ultrasonic transducers is a piezoelectric crystal [34]. Crystals can be shaped in order to produce different wave modes, and depending on the travelling material and its geometry, ultrasonic waves can also be propagated in different specific modes. The most commonly used are the Bulk modes, which can be of two types:

- Longitudinal or Compression waves: the motion of particles is parallel to the direction of propagation, that is, the wave describes a successive compression-relaxation motion along their path, as seen in Fig. 8, left (adapted from [34]).
- Transversal or Shear waves: the motion of particles is orthogonal to the direction of propagation, as seen in Fig. 8, right (adapted from [34]).

Both modes are characterized by their specific propagation velocity, which depends on the physical properties of the inspected material [33][35].



Fig. 8 - Left: Longitudinal wave. Right: Transversal wave (adapted from [34];  $\lambda$  corresponds to the respective wavelengths).

The formulas for the Longitudinal wave and Shear wave velocities, respectively, are given below:

$$V_L = \sqrt{\frac{E}{\rho} \frac{1 - \nu}{(1 + \nu)(1 - 2\nu)}} \quad (2)$$

$$V_T = \sqrt{\frac{E}{\rho} \frac{1}{2(1 + \nu)}} \quad (3)$$

Being  $V_L$  the longitudinal wave velocity,  $V_T$  the Shear wave velocity,  $E$  the Young Modulus,  $\rho$  the density and  $\nu$  the Poisson Ratio of the inspected material [34][38].

As Transversal waves are poorly transferred in gaseous environments, a coupling medium between the probe and the inspected material is required (which usually is a liquid or gel [4]). Couplants help transferring more sound energy into the inspected material, therefore allowing a feasible ultrasonic signal to be obtained (which wouldn't occur if couplants weren't used, due to the high acoustic impedance mismatch between air and the inspected material) [36].

One of the most commonly used ultrasonic techniques is Pulse Echo, where a single transducer is alternatively working as transmitter and as receiver, so that the amplitude and the time of flight of the reflected signal allow to detect the presence of a defect [35].

A general representation of the basic functioning principle in Pulse Echo can be seen in Fig. 9 (according to [32]). Like the figure suggests, the probe emits and receives ultrasonic waves which travel along the inspected material. When the waves strike a discontinuity, ideally part of them are reflected and the other is transmitted through the interface, as already mentioned [33][39]. The respective reflection is then shown on a proper device screen in an A-Scan, which usually gives information about the amplitudes of the echoes and the distance (or travelling time) between each discontinuity in the test specimen [34]. As seen on the figure's A-Scan, the initial pulse represents the reflected waves at the top of the inspected material, the backside (or back wall) echo represents the reflected waves at the bottom of the material, and the echo from pit represents the reflection that occurs when the ultrasonic waves find that certain defect.



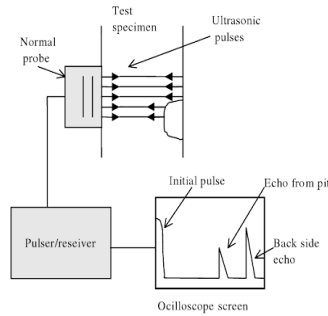


Fig. 9 - General representation of the basic functioning principle of UT Pulse Echo inspection [32].

Also, according to Fig. 10 a) (adapted from [39]), when there is no defects, the A-Scan only shows the initial and back wall echoes, but in Fig. 10 b) when the defect is wider than the ultrasonic beam on a given position, the Back Wall echo doesn't appear on the A-Scan.

Nowadays, most Conventional UT solutions use digital equipment that enable other visualization modes such as C-Scans, which offers details about the planar extension of defects through their 2D projected image, that is, as a function of X-Y coordinates of the probe movement along the inspected length (as seen in Fig. 11, adapted from [34]). It represents the echoes' amplitudes of the A-Scan of each inspected point as a function of a certain colour code, and when using Pulse Echo, a time of flight C-scan can also be obtained, providing the position through the thickness measurement of the defects [34][35]. As a matter of fact, two of the most widely used applications for Pulse Echo is thickness measurement in porosity detection and corrosion mapping [35][39]. Nevertheless, an encoder for position tracking is mandatory in order to generate a proper C-Scan [40].

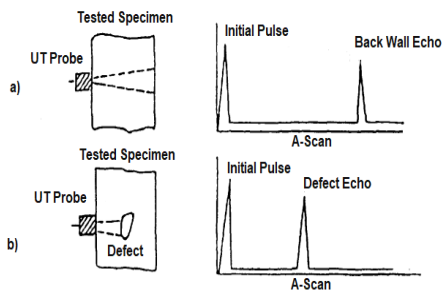


Fig. 10 - a) UT Pulse Echo inspection with no defects; b) UT Pulse Echo inspection with a defect wider than the ultrasonic beam (adapted from [39]).

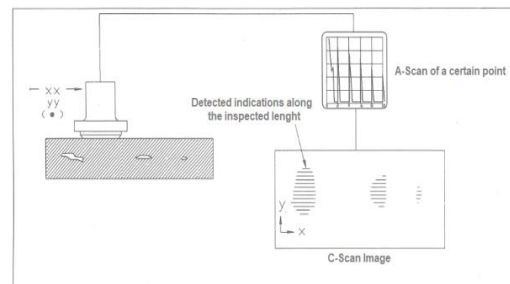


Fig. 11 - Scheme of a C-Scan representation (adapted from [34]).

## Main advantages and handicaps of Conventional UT

This technique has various pros which permit that great benefit on a certain inspection could be taken, having:

- High penetrative power that makes it possible to test a multitude of materials and thicknesses [34].

- Accuracy and precision when detecting the presence of small defects, along with its respective depth, dimensions and shape, being also suitable for thickness measurement of specimens with parallel surfaces [34][35].
- Portability, which makes it suitable for inspections in places of difficult access [34].
- A safety profile, so that it is non-harmful to other nearby equipments, materials or personnel [35][39].

But naturally it poses some limitations, such as:

- The necessity to use a coupling medium (if water is used, the test specimen must be water resistant) [34][35].
- It must be performed by experienced operators [39].
- The inspection is difficult when on materials with high acoustic attenuation, roughness, inhomogeneity, complex geometries, or very low thickness [34][35].
- Surface cleaning is usually necessary [35].

## 2.2.2. Eddy Current

In Eddy Current technique, the phenomena of electromagnetic induction is used to detect defects in electrically conductive materials. When an Alternating Current running through the coil of a certain probe is close to a given test specimen, a variable magnetic field (excitation field) is generated, inducing a circulating Eddy Current on the material (as seen in Fig. 12, adapted from [35]) [34][35]. The Eddy Current, on the other hand, produces its own magnetic field which opposes the excitation field and reduces the coil current. This results in an overall change of the coil impedance, which is the limitation to the propagation of its current. The Eddy Currents could be detected with a sensor which is sensitive to the magnetic field or by measuring the changes to the current flowing in the excitation coil, and then be amplified for visual display or a sound signal [32][35].

Given the same conditions, reduction in the current running along the coil should be equal for all identical specimens placed in the same position regarding the probes, thereby, the presence of a defect or a discrepancy in dimensions, for example, will cause a change in the Eddy Current and a corresponding variation in the phase and amplitude of this measured current [35][39]. Thus, this technique is also suitable to perform thickness measurement and corrosion detection [32][34].

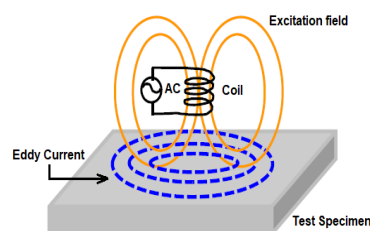


Fig. 12 - General representation of Eddy Current generation on a given test specimen by a coil in AC (adapted from [35]).

But in order to successfully perform an inspection using this technique, some factors need to be taken to consideration.

For example, the electrical conductivity of the test specimen has a very direct effect on the Eddy Current flow, that is, higher conductivities enable greater flows of Eddy Currents nearby the surface. Electrical conductivity can be influenced by various factors, such as the material composition, heat treatments and mechanical hardening. The magnetic permeability is another important factor, as it is a direct signal that a certain material can easily become magnetized. It can vary within the same material due to aspects like localized stresses and heating treatments, thus influencing the Eddy Current response. Geometrical factors like edges and grooves also alter the Eddy Current response, and last but not least, the distance between the coil and the test specimen (lift-off) also has great influence over the results, because the longer the distance, the lesser the effect Eddy Currents exert on the coil, therefore, sensitivity to any variation will decrease [35][39].

## **Main advantages and handicaps of Eddy Currents**

The major advantages of this technology are:

- The ability to detect small defects even in test specimens of complex geometry, with minimal surface preparation [35].
- It can perform inspections on any material which is electrically conductive [39].
- Contact between the probe and the inspected material is not mandatory [35][39].
- This technique can be easily automated, allowing for rapid inspections (which can be up to 100 m/s) of the test specimens [39].

Apart from that, it also presents some handicaps:

- Eddy Currents are restricted to a small layer beneath the surface of the material, called skin depth. If, for example, a certain defect or thickness is deeper than the skin depth, it won't be detected. Thus, the penetrative power into the test specimen is limited, making this technique only suitable for inspections in thinner materials [32][39].
- It requires trained, qualified and experienced operators [39].
- The technology is susceptible to various factors which can compromise the results.

Parameters like electrical conductivity, magnetic permeability, material geometry and lift-off need to be correctly addressed, otherwise it can give undesired outcomes [35].

### **2.2.3. EMATs - Electromagnetic Acoustic Transducers**

The functioning principle of EMAT technology is based on the simultaneous action of two components – the magnetic field generated by a permanent magnet (in some cases, an electromagnet

or a pulsed magnet) and the dynamic current which travels through a coil [41][36]. In transmitting mode, it imposes an electromagnetic field on the examined material, creating (by means of two main phenomena, Lorentz Forces and Magnetostriction [42]) an elastic field on its surface and generating ultrasonic waves. The reciprocal is also true in receiving mode - the ultrasonic waves are converted in electrical signals by the transducer [41][43]. Also, the presence of these principles varies if the material to be inspected is magnetic or nonmagnetic (being the Magnetostriction only present in magnetic conductive materials). Nevertheless, the material needs to be electrically conductive [36].

For nonmagnetic conducting materials, assuming (during transmitting mode) a system constituted by a vertical bias magnet on top of a flat coil, a certain inspected material on the base of the system will be subjected to two phenomena – the presence of the static magnetic field density  $\vec{B}$  in the material, created by the magnet (as seen in Fig. 13, left, adapted from [41], without the presence of a coil and its respective electromagnetic field, in order to better visualize the phenomena) and the Eddy Current density  $\vec{j}$ , generated by the magnetic field that the electrical current passing the coil induces [43] (as it is illustrated in Fig. 13, right, which was adapted from [44] according to the notions in [45], and without the presence of a magnet and its respective magnetic field, for the same reasons as Fig. 13, left). Note that field density  $\vec{B}$  can interact with the material surface in a parallel or perpendicular direction (or some angle in between) [46].

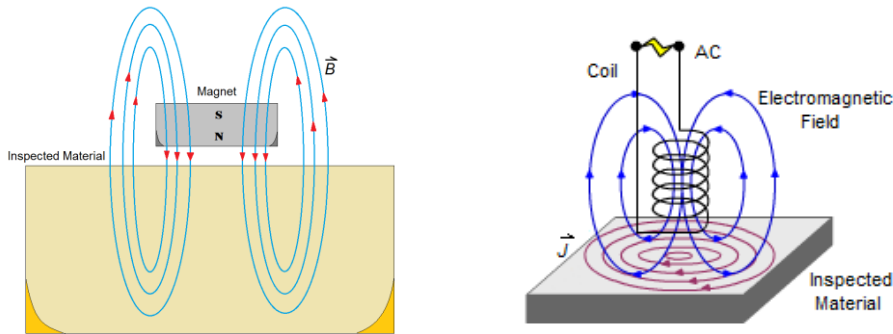


Fig. 13 - Left: scheme of influence of the magnetic field generated by a vertical bias magnet on an inspected material (adapted from [41]). Right: scheme of generation of Eddy Currents on a material by a meander coil (adapted from [44]).

The penetration range of  $\vec{j}$  is given by the electromagnetic skin depth  $\delta$  [41], according to the following equation:

$$\delta = \sqrt{\frac{2}{\omega\mu\sigma}} \quad (4)$$

Being  $\omega$  an assumed time harmonic (angular frequency),  $\mu$  the magnetic permeability, and  $\sigma$  the electrical conductivity [47]. Note that, for steels,  $\delta$  is approximately 0,01 mm, so one can consider Eddy Currents act on the material surface [41].

The combined effect of the magnetic field density  $\vec{B}$  and the Eddy Current density  $\vec{j}$  (parallel to the material surface) will generate the Lorentz Force  $\vec{F}_L$  at the surface region of the inspected material, given by the external product [47]:

$$\vec{F}_L = \vec{B} \times \vec{J} \quad (5)$$

This body force will create an elastic Shear Horizontal (SH) wave on the material, perpendicular to  $\vec{F}_L$  (which could be seen in Fig. 14, adapted from [46]) as the Lorentz Force has a dynamic character along its length, which is conferred by the alternating current passing through the coil [47].

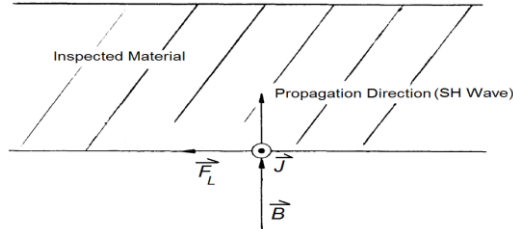


Fig. 14 - Generation of a SH Wave (adapted from [46]). Note that the Eddy Current density vector is normal to the image plane.

As mentioned above, the magnetic field density  $\vec{B}$  can also interact with the material surface in a parallel direction. In this case, the propagation direction will be parallel to  $\vec{F}_L$  – a Longitudinal wave (LW) will be generated (as seen in Fig. 15, adapted from [46]).

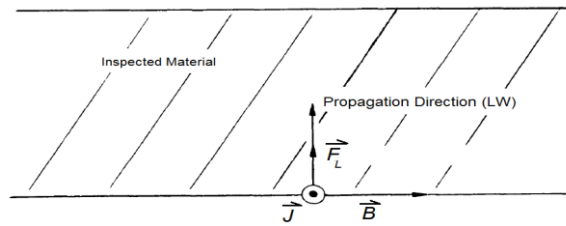


Fig. 15 - Generation of a Longitudinal Wave (adapted from [46]). Note that the Eddy Current density vector is normal to the image plane.

Then, if the static magnetic field makes some angle in between  $0^\circ$  and  $90^\circ$  with the material surface, both Shear Horizontal and Longitudinal waves can be generated [46], as exemplified in Fig. 16 (adapted from [41]). Like the figure suggests, SH waves are generated by horizontal  $\vec{F}_L$  and L waves are generated by vertical  $\vec{F}_L$ . Lorentz Forces are directly proportional to the current passing through the coils, and to the applied magnetic field [41]. One can see that, due to the limited range of the Eddy Currents, the electromechanical conversion takes place within the electromagnetic skin depth  $\delta$  [46].

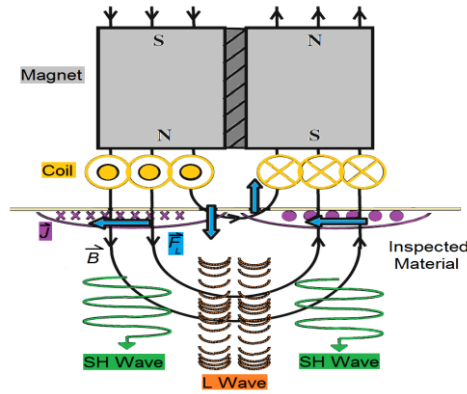


Fig. 16 - Simultaneous generation of SH and L waves with a periodical bias magnet and a racetrack coil (adapted from [41]). Note that the coil and Eddy Current density propagate in a direction normal to the reading plane.

For magnetic conducting materials, along with the Lorentz Force, there also has to be considered the Magnetostrictive Force, caused by the effect of magnetostriction, which occurs due to the orbital changes in the electrons on the surface region of the inspected material, in order to minimize their energy in the presence of an external magnetic field [41]. This could be intuitively explained by the scheme in Fig. 17 (present in [41]), in which occurs a dimensional change in a chain of small magnets connected by elastic springs when they are exposed to an external magnetic field strength  $H$ . In this figure, the magnets represent the atomic spins [41]. It's important to note that, even when the chain is not subjected to an external magnetic field ( $H = 0$ ), there is an elastic strain which maintains the equilibrium between the springs and the magnets – which in the real model is called spontaneous magnetostriction, and translates to an eigenstrain on the individual magnetic domains of the inspected material's surface area [41].

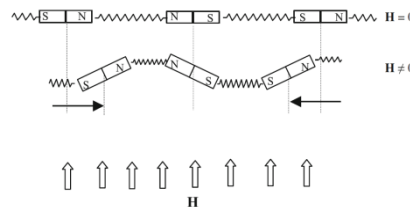


Fig. 17 - Scheme of the magnetostrictive effect on materials when exposed to an external magnetic field  $H$ , explained with a chain of magnets connected by elastic springs [41].

This explains why in polycrystalline materials (such as polycrystalline iron), the dimensional change occurs in two phases, as seen in Fig. 18 (present in [41]). The polycrystalline material is constituted by various random domains, inside each one the magnetization has a specific orientation, different from the adjacent ones' [48] (Fig. 18 a)). When subjected to an external magnetic field, the domains expand in volume, causing an elongation nearly parallel to the external field due to the positive spontaneous magnetostriction (Fig. 18 b)). And finally, the magnetization rotates according to the external field's direction (Fig.18 c)) [41].

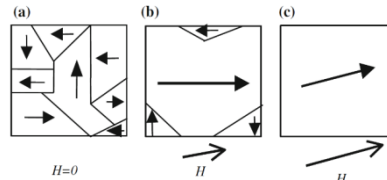


Fig. 18 - Magnetostrictive effect in polycrystalline materials subjected to an external magnetic field [41].

The magnetostriction effect along a certain material's surface is a function of the external field [41]. In EMATs, the combined effect of the static magnetic field caused by the magnet and the dynamic magnetic field caused by the passing of AC current through the coil modulates the magnetostrictive response along the material – in other words, the material extends and shortens about the length established by the bias field, producing periodic magnetostrictive stresses (that exist in addition to the stresses produced by Lorentz Forces [46]) which disembody in the propagation of ultrasonic waves [36][43]. An example of SH Waves generation by the magnetostrictive force in a certain EMAT configuration can be seen in Fig. 19 (adapted from [41]).

The magnetostriction phenomena depends significantly on the inspected material's physical properties [41].

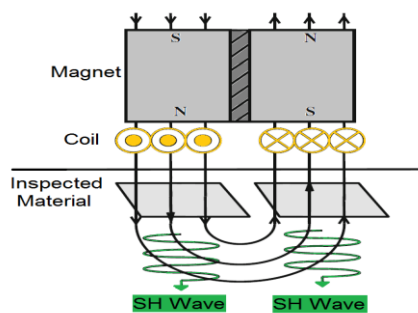


Fig. 19 - Example of SH wave generation in an inspected material due to magnetostrictive force, with a periodical bias magnet and racetrack coil (adapted from [41]).

The proper combination of different magnet and coil designs can generate a wide variety of types and patterns of ultrasonic waves [41][36][49]. Longitudinal wave and Shear wave velocities obey the same formulas as the ones in equations (2) and (3) respectively.

In respect to the receiving mechanism, the same transducer that excites ultrasonic waves can also detect them, and it behaves in general by the inverse phenomena of Lorentz and Magnetostrictive Forces [43].

For a nonmagnetic conductive material, the dynamic deformation of an acoustic wave, coupled with the steady magnetic field  $\vec{B}$  to which the material is subjected, induces Eddy Currents on the material surface region, inherently creating dynamic electromagnetic fields, which can pass the material surface and be detected by the coil [41][43]. The dynamic electric field induced by the deformation is the reverse Lorentz Force mechanism [41].

For magnetic conductive materials, the elastic deformation disturbs the magnetization state, resulting in an additional magnetic density flux. This is the piezomagnetic effect, or in other terms, the reversed magnetostriction mechanism [41].

With the magnetostrictive contribution, the signal strength is significantly increased when compared to the signal generated only by Lorentz Forces, although the last is predominant [36][50].

But above the Curie Temperature (which is 770 °C for Low Carbon Steels), ferromagnetic materials become paramagnetic, due to a rearrangement of the electrons' magnetic moments to a disordered state, which significantly diminishes the efficiency of electromagnetic ultrasound generation. This happens because the magnetic flux density at the surface of a paramagnetic material is lower than that on ferromagnetic materials, (so the Lorentz Force will also be weaker), and because the effect of magnetostriction is dependent on the mechanical strain arising from ordered domains when they are aligned with the applied magnetic field, but in paramagnetic materials the domains are in a disordered state, therefore no strain is made and the magnetostrictive effect is null [50].

The results can also be displayed in digital equipments, taking advantage of visualization modes like A-Scan and C-Scan [51]. Also, due to its affinity with ferromagnetic materials and tolerance at high temperature environments, this technique it is widely used to perform corrosion inspections in pipelines [41][36][43].

## **Main advantages and handicaps of EMATs**

It is evident that EMAT technology holds various advantages when compared to other conventional techniques:

- There is no need to use any kind of couplants in the inspected material, which reduces the equipment setup time as no preparation and further cleaning is required, allowing more efficient and cheaper inspections (because high temperature couplants are very costly [52]) [50].
- It has the ability to generate various wave modes which could be used to meet a wide range of measurement needs [41][36][43].
- The EMAT probe can be in contact with the inspected material, or with a certain lift-off, therefore this technology could be used in coated and rough surfaces (up to a certain limit), and is practically not affected by oxidation or surface pollutants [43].
- The versatility of this technique allows it to be used in a multitude of challenging inspections, like on moving specimens or at potentially dangerous environments [36][43] [53].
- EMATs don't make use of any hazardous equipment, making it a safer option [36].

But on the other side, this technology also presents some handicaps:

- EMATs traditionally have lower transduction efficiency when compared to Conventional Ultrasonic Testing [41][36]. This makes the design of EMAT probes more challenging in order to overcome this obstacle, for example, by using high transmitting currents, low noise receivers and careful matching of each component [36][49]. Noise is a phenomenon which could have various causes such as the inspection environment, the conditions of the testing equipment and conditions of the inspected material, disemboing in the possible presence of unwanted echoes in the A-Scan acquisitions [34][54].
- The performance of this technology significantly depends on the properties of the inspected material - it needs to be electrically conductive [41] and it shouldn't be paramagnetic, which restricts the scope of materials that could be inspected [50][55].



- Experienced technicians are required to perform the inspections [56].
- In some cases, EMATs could need to be complemented with Conventional UT for exact sizing [56].

As previously seen, every three of the presented inspection techniques could be used to perform high temperature corrosion inspections on Carbon Steel structures. Nevertheless, one could be more suitable to address the specific needs that *ISQ* customers have. Therefore, the next step would naturally be to scan the market for the most appropriate equipment.

### 2.3. Market survey

In a vast engineering market with increasingly numerous offers, NDT equipments for high temperature corrosion inspection are limited by various detrimental factors such as service temperature, ease of use, inspection time and cost [26]. It is then of major importance to know what products are present on the NDT market, in order to select the most appropriate equipments to match *ISQ* customers' needs.

The various market offers would need to be analysed and selected using the specific customers criteria present in Chapter 1.3.

#### ***Silverwing RMS2***

This solution permits corrosion mapping of ferrous structures up to 200 °C such as storage tanks, pipelines and pressure vessels, using ultrasonic testing.

Created by *Silverwing*, *RMS2* gives total inspection coverage over a maximum range of 50 m length and 1 m width in one single session, at 730 mm/s, in pieces up to 280 mm thickness. The scanner positioning is easier due to a mounted camera, and due to its automation, there is no need to use scaffolds (hence the maintenance costs are reduced). Also, there is no need to remove surface paints.

This equipment also has the possibility to switch from different scanning heads to suit different inspection requirements: to maximize scanning rates (*RMS2 600*), to operate longitudinally (*RMS2-450*, seen in Fig. 20, left according to [57]), to run in limited access areas (*RMS2 300*) and to inspect circular profiles (*RMS2 ARC 24 -36*, seen in Fig. 20, left according to [57]) for example. The system is also supported by an electronically controlled water pump, which can deliver 5.7 litres of water per minute at a height of 30 meters (Fig. 20, right shows a practical application of *RMS2 450*, as seen in [58]).

Its analysis software permits real-time display of A-Scans and C-Scans, thickness measurement and positional data (as high as 0.5 mm x 0.5 mm resolution). Settings can be readjusted after the acquisition, in order to produce a more accurate C-scan image, or highlight particular indications, as an example. Also, the system records A-Scans which can be processed and rectified afterwards. This minimizes the set up on site and avoids rescanning due to incorrect settings. It also

provides sizing tools, being easy to identify any defects [57][59].

With a transducer range from 2.5 to 10 MHz [57], this equipment can detect defects of uniform corrosion, pitting corrosion and erosion corrosion [60].



Fig. 20 - Left, up: *RMS2 450* equipment. Left, down: *RMS2 ARC 24-36* equipment [57]. Right: industrial application of *RMS2 450* [58].

## ***Phoenix SSHTC***

Meant to inspect hot surfaces, this is a range of twin crystal, compression wave transducers developed by the company *Phoenix ISL*.

Ranging from 1 MHz to 5 MHz frequency, and nominal focuses from 8 to 28 mm (which means that, depending on the chosen probe, it can inspect materials of maximum thicknesses from 8 mm to 28 mm), these equipments can work continuously up to 120 °C and intermittently up to 200 °C, leaving the probe to cool for 1 minute when reaching 10 seconds of continuous contact (Fig. 21 shows two of the *SSHTC* probes, as seen in [62]). Twin crystal means the probe has two crystals, one with the transmitting function and other with the receiving function, which gives good near surface resolution [63]. They have an outer skin of Stainless Steel which grants increased robustness [62].

Using the higher frequency probes (5 MHz), the equipment can detect uniform corrosion, pitting corrosion and erosion corrosion [60], but as it is, it can only perform spot inspections (A-Scans).



Fig. 21 - From left to right: Phoenix SSHTC 4/10 and SSHTC 4/6 - High Temperature Twin Crystal Compression Wave Transducers [62].

## ***Innerspec High Temperature Sensor SH Spiral***

This is probe purposely engineered by the American company *Innerspec Technologies* for inspections at high temperature surfaces.

It has a SH Lorentz permanent magnet. SH stands for Shear Horizontal, which means it was built to perform inspections using Shear Horizontal waves [64], while Lorentz relates to the effect that contributes the most for the generation of ultrasonic waves in this probe, which is the Lorentz Force [65], and permanent magnet indicates that this probe's magnet exerts a permanent magnetic field [66].

The probe also has a spiral coil, following the same configuration as in scheme of Fig. 22, left (adapted from [50]), which in conjunction with the magnet, produces radially polarized Shear Horizontal Waves (that is, SH waves generated by Lorentz Forces acting along the radial direction, due to the product of the radial component of the static field with the Eddy Current flux; Normal Lorentz Forces are generated by the product of the vertical component of the static field with the Eddy Current flux, creating Longitudinal waves, although this contribution is minimal [41]), as the side view of Fig. 22, right (adapted from [41]) suggests.

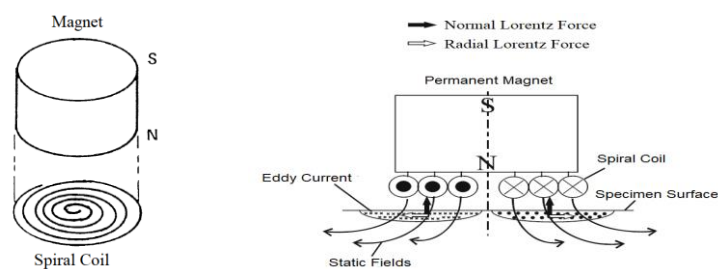


Fig. 22 - Left: scheme of permanent magnet and spiral coil (adapted from [50]); N and S stands for North and South poles of the magnet. Right: side view of Lorentz Force generation with permanent magnet and spiral (or pancake) coil (adapted from [41]).

This system can perform continuous inspections at structures with surface temperatures up to 200 °C without cooling. From 200 °C to 450 °C, it also performs continuous inspections but with the aid of an air cooling system, which can be plugged to a compressed air stream source that is present in most industrial facilities, providing a rapid, easy and safe cooling solution (as it doesn't require any previous preparation, no further cleaning and no harmful products). This equipment can even perform inspections from 450 °C to 650 °C with air cooling and 30s contact duration [64].

According to the ultrasonic beam profiles in Fig. 23 (as in [64]), this probe can detect defects of minimum diameter near 16 mm, at 10 mm thickness specimens, and it can analyse materials up to 120 mm thickness, making it fit for thickness measurements and flaw detections, that is, inspections on uniform corrosion, erosion corrosion and pitting [64]. As Fig. 23 suggests, this ultrasonic beam has a dead zone in the middle of its profile, where the signal has no strength, which is confirmed by the transducer configuration in Fig. 22.

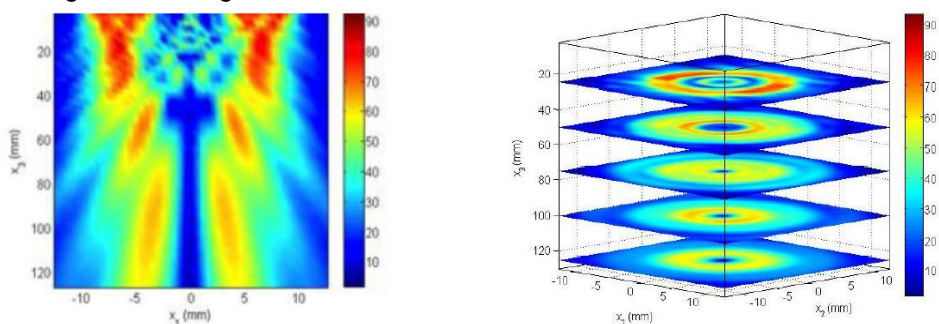


Fig. 23 - Ultrasonic beam profiles of *Innerspec High Temperature Sensor SH Spiral* [64]. X1 stands for length, X2 for width and X3 for thickness. The colour grade chart (which goes from 0% to 100%) is related to the ultrasonic signal strength.

Furthermore, it is meant to be used with a dedicated digital equipment, the *PowerBox H*, which has the ability to edit various probe settings for optimal inspection performance regarding each specific specimen. It also generates reports in various formats such as A-Scans or C-Scans (with an encoder), delivering real-time display of results. The reports can be furtherly accessed in the *PowerBox H*, or saved to an external device (it has a port for SD card, USB and mini USB each) to be consulted in any computer with *Windows* software, using the program *PowerBox H PC Viewer* that emulates the display of the actual digital device [51]. It has a removable battery of 8h maximum life, which takes only 2h to be fully charged. A frontal view of the equipment can be seen in Fig. 24, left, (as in [51]). *PowerBox H* can even be used with an harness, to inspect environments of difficult access (as in Fig. 24, right, according to [67]).



Fig. 24 - Left: *PowerBox H* frontal view [51]. Right: *Powerbox H* used with an arness [67].

The probe can only perform spot inspections (no C-Scans), as it doesn't come with any attached encoder. Therefore, as it is, this equipment cannot perform corrosion mapping at high temperature surfaces, unless a proper encoder is coupled to the probe. Fig. 25 shows the probe in different views (as in [64]).



Fig. 25 - *Innerspec High Temperature Sensor SH Spiral* in different views [64].

## ***Eddyfi Lyft***

This equipment was developed by *Eddyfi* using Eddy Current technology, it presents a portable instrument which is able to create real time C-Scan imaging and complete wall thickness measurements of inner and outer diameter tubes, being capable of performing total inspection management and reporting. This equipment, unlike those previously presented, gives qualitative results, which vary over a certain range of values [68][69].

It has a digital interface that is portable, water and dust resistant, and cools without any external air exchange, making it appropriate for on-site inspections as seen in Fig. 26 (as seen in [70]). Running in *Windows* software, it can be easily connected to any computer. It also comes with two batteries (which can last up to 8h each) for extended autonomy. With two USB and one HDMI port, this even comes with an extra USB entry to perform quick copies, transferring all inspection files at the touch of a button [69].



Fig. 26 - Eddyfi Lyft with Single Element PEC Probe being used at on-site inspections [70].

The system has algorithms that remove operator-specific dependence, and automatically optimizes pulser and receiver parameters as well as wall thickness measurements. And it also comes with a desktop software, *Lyft Pro*, that provides advanced data analysis through the same graphical display as the *Lyft* digital interface, making it easy to process larger data layouts and plan future inspections [69].

This scanner has various types of different sized plug-and-play probes for the right balance between wall thickness and lift-off, from tube probes (which are meant to inspect tubes from inside) to underwater probes, but the most adequate for inspections of erosive corrosion, pitting and uniform corrosion is the *Single Element PEC* probe, which can test materials up to 102 mm thickness [68]. *Single Element* means it has the most simple form of Eddy Current generation, an AC coil (as explained in Chapter 2.2) and *PEC* stands for Pulsed Eddy Current, which means that it uses a step function voltage to excite the probe instead of sinusoidal alternating electrical currents of a particular frequency, as in conventional Eddy Current inspections. The step function voltage contains a continuum of frequencies, and as the depth of penetration is dependent on the frequency of excitation, information from a range of depths can be obtained all at once [71][72].

It also needs to be coupled to an encoder in order to perform corrosion mapping, which wouldn't be an issue because an attachable encoder is sold by the same company.

As could be noted by the customer's criteria, it is needed that the equipment chosen to perform the desired inspections delivers quantitative results, in order to accurately detect critical defect depths and thickness discontinuities. That being said, it could be seen that the great differentiating factor among the presented market offers which give quantitative results, is the maximum inspection temperature tolerated by the probes.

Many of the structures, (which *ISQ* clients want the company to inspect), like tanks, boilers and pipes, operate at temperatures above 200 °C, easily reaching 300 °C and 400 °C [21][26][61]. That impairs the application of every existing equipment except for the *Innerspec High Temperature Sensor SH Spiral*, which can inspect structures up to 120 mm thickness, for the detection of uniform corrosion, erosion corrosion and pitting corrosion defects up to 400 °C. However, as it is only able to do spot inspections (A-Scan), which is a very basic and impractical solution, it requires the attachment of a proper encoder in order to perform corrosion mapping (A+C Scans).

There isn't in the NDT market any integrated equipment which generates A+C Scans, for the detection of corrosion defects in structures up to 400 °C, according to the aforementioned criteria.

Consequently, it was concluded that the most feasible solution was to create a prototype, which name is *EMAT Heat Inspection*, that would satisfy the customer's needs. It consisted in the use of the *Innerspec* probe and a proper encoder to create an assembled scanner which would function together with the *PowerBox H* acquisition equipment.

The present work, developed by *IST* in collaboration with the *Non Destructive Testing Laboratory* of *ISQ*, aimed to create *EMAT Heat Inspection* prototype, as well as proper validation apparatus which enabled the execution of validation tests on the prototype in order to legitimize it for inspections on the aforementioned conditions.

If all customer's requirements were fulfilled, the prototype would fill a gap in the Inspection Services market, offering the possibility to perform axial and circumferential inspections for A+C Scan report generation on the detection of corrosion defects of critical depths and Ø16 mm minimum, and minimal discontinuities of 4 mm, at structures of nominal thicknesses from 10 mm to 30 mm, and temperatures up to 400 °C, in Carbon Steel Structures. *EMAT Heat Inspection* prototype would also create a portable solution to perform bottom, vertical and upside-down inspections, being used in places of difficult access, with reduced setup times and decent scanning velocities, thus dispelling the necessity of shutting down the production site for the inspections to be conducted and giving a competent solution for the monitorization and control of corrosion defects.

## 3. Design and construction of *EMAT Heat Inspection* prototype

### 3.1. Scanner prototype build-up

To create the scanner prototype, technical knowledge about its main components - the probe and the encoder - needed to be acquired. Then, all the necessary connections (including the ones to the acquisition equipment) had to be schematized before proceeding to the design of the scanner structure, so that further fabrication of the respective structure components and actual assembling could finally be done.

#### 3.1.1. Presentation of the main components

Understanding of the working principle and technical data regarding the probe and the encoder was mandatory in order to proceed with the scanner creation.

As already mentioned, the chosen probe was the *Innerspec High Temperature Sensor SH Spiral*, an Electromagnetic Acoustic Transducer which functioning principle and main technicalities can be found in Chapter 2.2 and 2.3, respectively. It weighted 1 Kg and, due to its magnet, was highly attracted to ferromagnetic materials, which could be useful to help keeping the scanner on top of the test surfaces in certain inspection positions. Also, the probe had a built-in two-pin *OB LEMO* connector, for transmission and receiving of signals to the acquisition equipment, one ¼" NPT (American size) thread which enabled cooling with compressed air (if a proper housing was connected) and four 8-32 (American size [73]) threaded holes for fixing, as seen in *Innerspec Probe Exploded View* at Chapter 7 [74]. The nominal dimensions were Ø63 mm x 70 mm [74].

In respect to the encoder, a very good solution was the *RI32-O/360AR.14KB* by *Hengstler* (seen in Fig. 27 as in [75]). This was an incremental optical rotary encoder, weighting 50 grams, which could operate at temperatures between -10 °C and 60 °C, having 3 threaded holes (of M2 thread dimension) for fixing, and maximum rotation speeds of 6000 rpm, being an economical solution to be used in small equipments [75]. This kind of encoders used optical sensing technology that had an embedded rotation code and a pattern, being able to provide signals (in the form of pulses) that could be easily interpreted to provide motion related information such as velocity or change in position [76]. Its nominal dimensions were Ø30 mm x 27.20 mm (rotary shaft was Ø5 mm x 11.50 mm). The encoder had a built-in cable which could be plugged to the acquisition equipment (*PowerBox H*) if proper connections were made.



Fig. 27 - Hengstler RI32-O/360AR.14KB encoder [75].

After all the geometrical and technical considerations of either the probe and encoder were known, the next step was to schematize all the required connections.

### 3.1.2. Connections schematics

The scheme of connections between the *PowerBox H*, the encoder and the probe, as well as the air housing, along with knowledge on fittings and cables, was of major importance during the conceiving phase.

The general schematic was represented in the following Fig. 28:

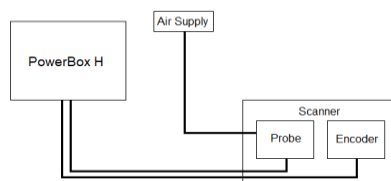


Fig. 28 - General schematic of *EMAT Heat Inspection* equipment.

As can be noted, the probe and the encoder were not directly connected – they both plugged to the *PowerBox H*. In order to avoid opening the scanner each time one wanted to connect/disconnect the probe or the encoder, the most practical solution was to fix three panel connectors to the scanner casing: one for the electrical connection between the encoder and the *PowerBox H*, other for the electrical connection between the probe and the *PowerBox H* and finally another for the air supply to the probe. As it suggested, the probe and encoder were permanently connected to the panel connectors inside the scanner. When the equipment was being used, the *PowerBox H* and the air supply were connected to the panel connectors in the scanner casing, and after usage they were simply disconnected from the panel connectors.

For the sake of simplicity, each electrical and air connection was explained in Fig. 29, along with the respective reference of each component.

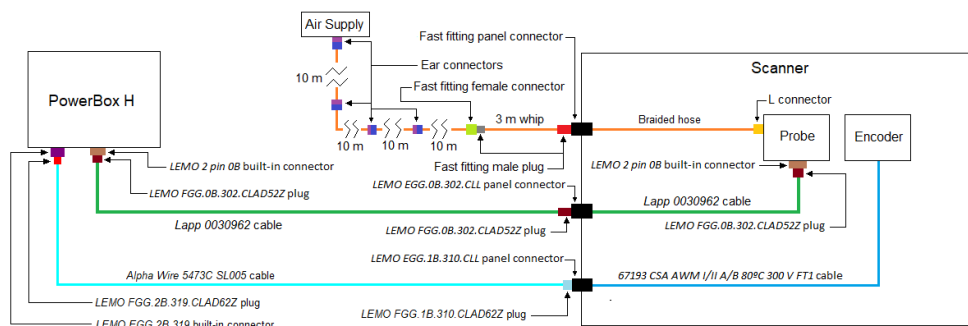


Fig. 29 - Connection schematic with information on connectors and cables (not on scale).

In respect to the probe, *Lapp 0030962* cable had 2 m outside the scanner, 1 pair of wires with shielding and was pyro-retardant, which granted extra protection against higher temperatures (up to 80 °C) [77].



The encoder cable, *Alpha Wire 5473C SL005*, had 2 m, 3 pairs of wires with shielding and was also pyro-retardant (up to 80 °C) [78].

About the air supply, all the 10 m hoses and the 3 m whip were braided. The whip had an outer diameter (OD) of 12 mm, and all the 10 m hoses had OD 18 mm. The fast fitting metal male plugs had Ø8 mm and DN9 connection, the fast fitting metal female connector had Ø8 mm and DN9 connection, the fast fitting female panel connector had Ø8 mm, and the L air metal connector had Ø8 mm and NPT thread (American size). The hose inside the scanner could be slightly punctured on 2 or 3 points, leading to a small air loss which was sufficient to cool down the scanner interior (and consequently, the encoder, which couldn't operate at temperatures higher than 60 °C).

Detailed information on the pinout schemes could be found in *EMAT Heat Inspection User's Guide*, present in Chapter 7.

The *Alpha Wire* and *Lapp* outside cables, and also part of the 3 m whip, were protected by a 2 m heat resistant sleeve, *Techflex Insultherm Ultraflex Pro* (Ø38,1 mm), that could hold temperatures up to 93 °C (which was acceptable since the sleeve wouldn't be in direct contact with the high temperature structures and ambient temperature would never reach that value).

Also, inside the sleeve was a 1 m Steel string which connected the scanner to the *PowerBox H* through its respective cable holders. The objective of this Steel string was to prevent the electrical connectors to stress out.

After all the connections have been schematized, and all the fittings have been enumerated, the scanner could start to be designed.

### 3.1.3. Scanner prototype design

In the designing phase, the scanner prototype started to take form. All the geometric aspects were taken into consideration, in order to create a portable, resistant and efficient equipment .

Since that was a manual scanner, it was important to perform a brief ergonomical study, which would contribute to create an equipment which was more comfortable to use.

In order to effectively handle the scanner prototype, two factors needed to be addressed by the user – a certain degree of force, in order to move the equipment forward, and stability, to move the scanner along a straight trajectory. Thereby, various sources described that the grip which conferred the best balance between force and stability was the *cylindrical grip*, where all the fingers were flexed over a cylindrical object, except for the thumb, which could be pointing in the axial direction [79][80]. This specific thumb position reduced some of the grip power (when compared with the thumb arched on the same radial direction as the other fingers), but conferred more stability and precision, being able to control the direction which the force was applied [81]. Fig. 30 shows an example of the cylindrical grip (adapted from [82]).



Fig. 30 - Cylindrical grip with thumb pointing in axial direction (adapted from [82]).

That led to the idea that one of the best possible designs was to have a handle similar to those commonly found in a clothes iron. Not only would it confer a more smooth and stable movement, but it would also make it easier to take the scanner away from the test specimens. Also, the handle could be hollow and with various holes, so that the small share of compressed air that would be cooling the scanner interior (as already suggested) would also be redirected to cool the user's hand when temperatures got higher.

Regarding the handle construction, it would depend greatly on the chosen material and the available production processes, being the four big deciding factors the weight, thermal resistance, mechanical strength and cost. And besides existing various plastics that were lightweight and could handle higher temperatures (like PEEK and PTFE [83][84]) the price of raw material plus its machining costs was too high, because it would imply to create the whole handle out of a single solid block [85][86]. So, the most feasible alternative was to opt for Aluminium rods which could be turned and milled in separate parts that could later be welded together in *ISQ* facilities, making that a much cheaper option. Fig. 31 shows preliminary drawings of the handles separate parts and its respective subassembly.

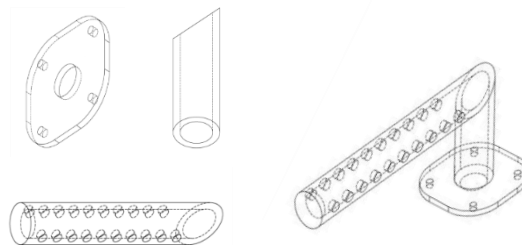


Fig. 31 - Left: preliminary drawing of the different handle parts. Right: preliminary drawing of handle subassembly (invisible lines are present in order to better perceive that the handle was hollow).

Following that thought line, the handle could be on top of a casing inside which would be the probe and encoder. The deciding criteria for it was the same as for the handle. Various design attempts were made, such as the one in Fig. 32, which was a rather stylish approach but impractical to do, because trying to create it by sheet bending and further welding, if not impossible, would create a poor quality product at the end, and machining it out of a solid block would be very costly even for an Aluminium or Stainless Steel raw material, not to mention plastics like PEEK or PTFE.

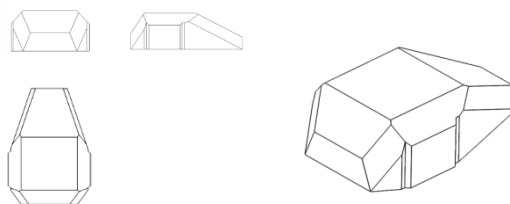


Fig. 32 - Left: first angle view of casing prototype drawing. Right: isometric view of casing prototype drawing.

Then, at the end, the chosen approach which seemed to be the cheapest and most efficient was to create a three part casing, consisting of a rectangular milled top made in Aluminium which was in direct contact with the handle, a rectangular centre with two Stainless Steel (AISI 304) bent sheet metal parts which would later be welded together in *ISQ*, and a rectangular milled bottom made in Aluminium where the probe and encoder were held. The Aluminium top and bottom made the scanner more lightweight (when compared with Stainless Steel) while it still conferred good mechanical resistance. The Stainless Steel sheet metal frame at the centre gave increased structural integrity, and since it was made from bent sheet metal, it was not a much heavier alternative [87]. Fig. 33 shows a preliminary drawing of the different casing parts. The three larger holes in one of the sheet metal parts (Fig. 33, middle, up) were made for the probe, encoder and air panel connectors, while the two smaller ones were for a shackle that held the 1 m Steel string (as already stated) to the scanner.

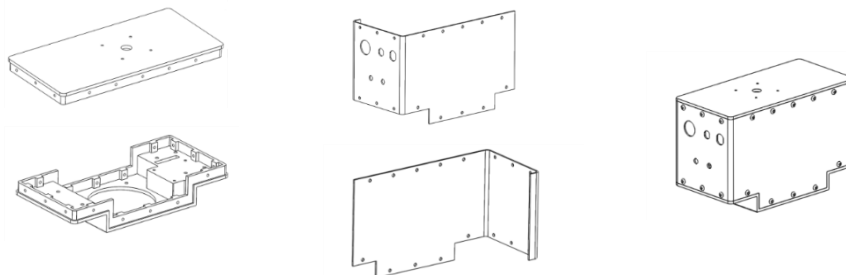


Fig. 33 - Preliminary drawings of the different casing parts. Left, up: Aluminium top. Left, down: Aluminium base. Middle: two Stainless Steel sheet metal parts. Right: casing subassembly, held together with screws.

Then, the probe and the encoder needed to be properly fixed at the casing base. In order to inspect curved surfaces of different diameters, the probe must not be static – it needed to have one degree of freedom in the axial direction which enabled the probe to move upwards and downwards according to the inspected diameter.

The most practical and simple solution would be to use a Stainless Steel cup, and a set of springs, which needed to be strong enough so the probe didn't fall down the scanner or it didn't get difficult to uncouple the scanner from the specimen due to the magnetic attraction of the probe to the ferromagnetic material. The springs also needed to be installed in such a way that it would be easy to assemble and disassemble them when required.

A preliminary scheme of the cup functioning principle is presented in Fig. 34. The images are opposing section views of the same middle plane, that is, the cup subassembly had one pair of springs (on top it was hooked to a screw which was fixed at the cup with a nut and on bottom it was hooked to a set screw which was threaded to the probe) and one pair of long screws (on top its heads were confined to a small compartment where they could only move up (as high as the nut would let) and down and at the bottom they were threaded to the probe). The presence of long screws and small compartments assured that only axial movements were possible and the alternated configuration of spring and long screw in each view granted a more even distribution of forces. And, as can be seen by the scheme, the cup top had a large hole for the interior to be accessible. The cup was to be held in the casing base with screws and nuts. Fig. 35 shows an exploded view of the cup subassembly, (horizontally disposed for the sake of convenience) in order to better illustrate its configuration (note that both screws of group 7 and 10 had transverse holes for the springs to pass inside).

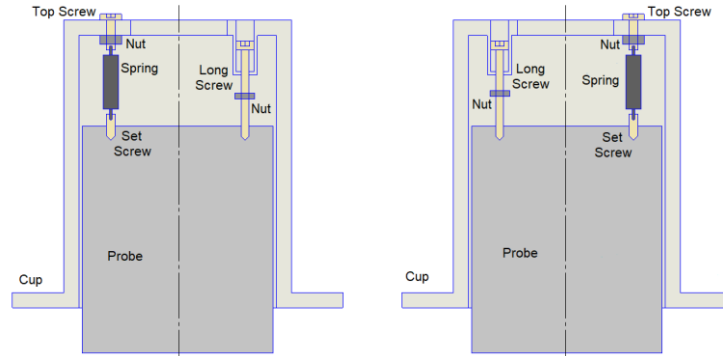


Fig. 34 - Scheme of probe cup functioning principle.

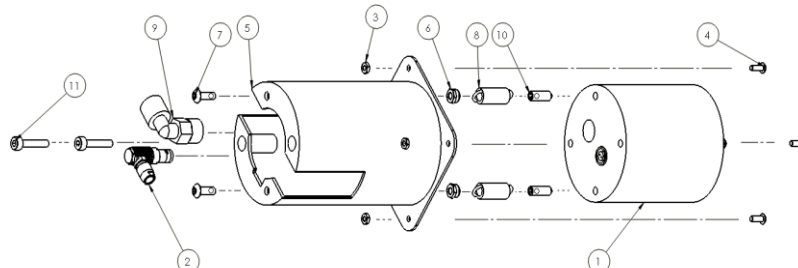


Fig. 35 - Cup subassembly exploded view. 1: probe; 2: *Lemo FGG.0B.302.CLAD52Z* plug; 3: nuts to fix the cup; 4: screws to fix the cup; 5: cup; 6: nuts to fix the top screws; 7: top screws to fix the springs; 9: L air connector; 10: set screws to fix the springs.

The cup was made of three different parts which would be produced separately and then be welded together, namely the base, the middle and the top, as Fig. 36 suggests.



Fig. 36 - Drawing of the different cup parts.

About the encoder, the main functioning requisite was that its temperature didn't exceed 60 °C, and for that to happen, a small PTFE container was conceived to hold and protect the encoder (as this material had good thermal insulation [88]). Now, the encoder needed to be coupled to one of the scanner wheels in order to function, and since it was inside the casing, the chosen option was to put one of the wheels below the encoder and make a loophole in the casing base beneath the encoder spindle, so that they could be coupled with a heat resistant O-ring of Ø40 mm x 2 mm, as seen in Fig. 37. The O-ring material was a FKM fluoroelastomer also known as Viton, which was resistant to temperatures up to 230 °C and sufficiently adhering to transmit motion between the scanner wheel and the encoder without sliding [89]. A slight notch was made in the encoder spindle for a grooved plug (where the O-ring stood) to fit in. Fig. 38 shows a simplified scheme of a scanner section which included the encoder inside its PTFE holder, the O-ring, the loophole where the O-ring passed and the coupled wheel below the encoder.

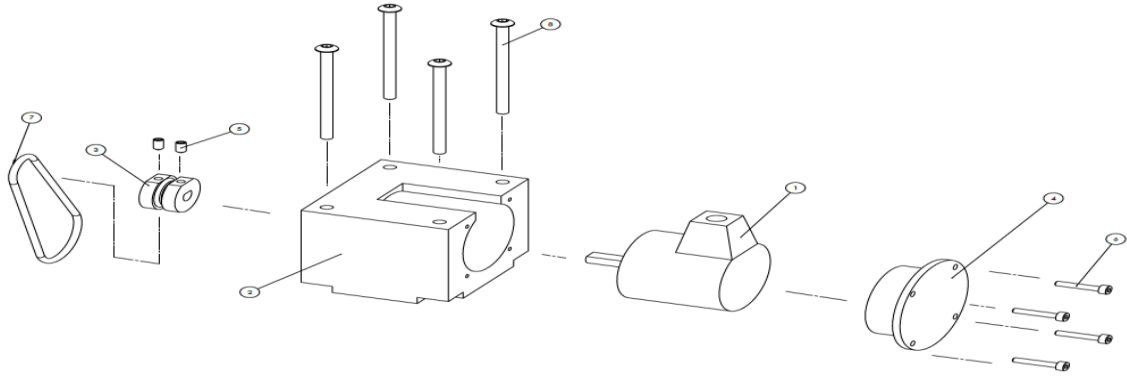


Fig. 37 - Exploded view of the encoder subassembly. 1: encoder; 2: encoder holder; 3: plug which fits in the encoder spindle; 4: encoder holder lid; 5: screws to fix the plug; 6: screws to fix the encoder lid; 7: o-ring; 8: screws to fix the encoder holder.

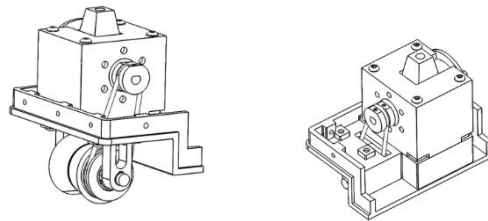


Fig. 38 - Simplified scheme of scanner section including the encoder, o-ring and coupled wheel.

To make the longitudinal inspections of curved surfaces possible, the wheels were meant to have a v-groove. And to resist temperatures up to 400 °C without degradation, Stainless Steel (AISI 304) seemed to be a good option [87], but after consulting many market offers, there was none which contemplated solid Stainless Steel wheels of the desired size (OD 30 mm). Also, there was also the challenge of one of the wheels needed to be coupled to the O-ring. Therefore, two Stainless Steel v-grooved wheels were specially designed for the purpose, as Fig. 39 shows (one of the wheels had a grooved protrusion where the O-ring stood coupled). The distance between wheels was such that they allowed the scanner to inspect the perimeter of tubular surfaces of minimum OD of 331 mm, and the v-grooves granted longitudinal inspections on tubes of minimum OD of 104 mm, which met the geometrical requirements presented in Chapter 1.3.

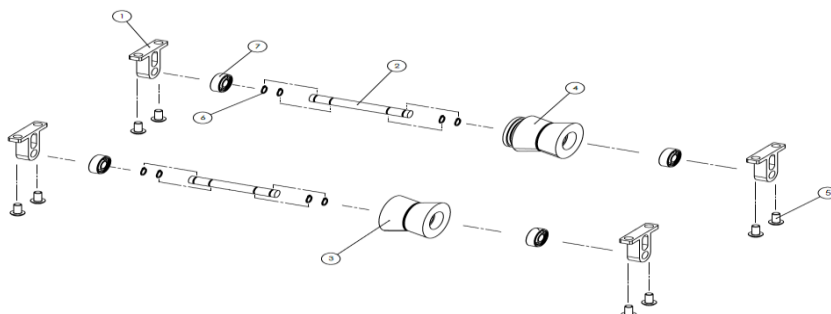


Fig. 39 - Scheme of wheels subassembly in exploded view. 1: wheel supports; 2: spindles; 3: normal wheel; 4: wheel to couple with encoder; 5: screws to fix the wheel supports; 6: retention rings; 7: roller bearings.

Then, Fig. 40 shows two external views and an internal view of the final 3D model of the scanner (without cables), made with *Solidworks 2017* software. There can be seen that the wheels were fixed to the casing base by the supports. A small pusher rod was added next to the handle in

order to help push the probe to the test specimen when they first come in contact, since the springs maintained the probe inside the scanner prototype (after that, the pusher was no longer needed because the magnetic attraction between the probe and the Carbon Steel specimen was strong enough for the scanner to stay coupled). The pusher didn't come out in upside-down inspections because it had a nut inside the scanner. As can be noted, the handle was slightly uncentered, in order to facilitate the rotation and removal of the scanner from test structures at the end of inspections.

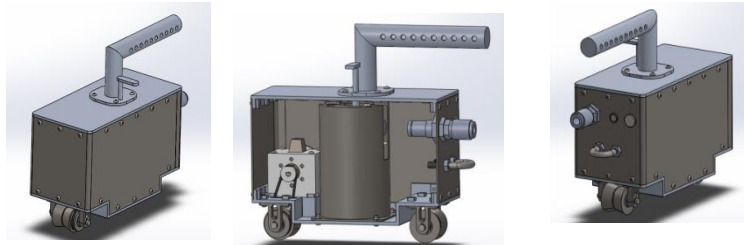


Fig. 40 - Right and left: two external views of the final scanner prototype model. Middle: internal view of the final scanner prototype model (made with *Solidworks 2017* software).

Now that the designing phase was concluded, the scanner prototype was ready to go into the production phase.

#### 3.1.4. Scanner prototype production

Each previously designed part of the scanner was then sent to be produced, and each accessory was bought, so that they could later be all assembled for the final prototype equipment.

All the parts which were meant to be produced by turning and milling, such as the casing top and bottom, the hollow rods of the handle, the encoder holder, the plug, the wheels and respective spindles and supports were produced by *MJ Branco*, a company specialized in precision mechanics for the Engineering Industry [90].

All the parts that required sheet metal bending or laser cutting, like the casing middle parts and the handle base, were produced by *Lasindustria*, a company which provided services such as water jet or laser cutting, edge bending and roller bending [91].

The air panel connector, the L connector and the hoses with respective male and ear connections were bought at *ETOPi*, which had a vast catalogue of pneumatic equipment and accessories [92].

The O-ring was bought at *SOVE*, whose scope of business was focused towards the selling of seals [93].

*Lemo* connectors were bought via an official company seller [94].

All the electric cables were bought at *RS Components*, which was specialized in the selling of electronics, via the company website [95].

And finally, the heat resistant sleeve was bought in the *Techflex* official website (a company which was focused in engineering accessories) [96].

All the screws, nuts, roller bearings, retention rings, springs, the Steel string and the shackle

were already available to use at the *Non Destructive Testing Laboratory of ISQ Group*.

The cup, due to its intricate design, was constituted of different Stainless Steel parts which were produced separately and then welded at *ISQ*. The base was made in *Lasindustria*, while the rest was done in *MJ Branco*. The middle section of the cup was produced through a larger tube, which was cut so that the diameter could match the desired value – that left a longitudinal stitch along the part which had to be welded. Fig. 41 shows various photos of the welding procedure at *ISQ*.



Fig. 41 - From left to right: welding of the handle base; welding of the handle rods; welding of the casing middle; welding of the cup top; welding of the cup base.

After welding, the material around the casing frame weld had consequently darkened. Therefore, a nitric acid passivation of the Stainless Steel casing frame was done in *ISQ*, according to the procedure in *ASTM A-967-96* [97]. Fig. 42 illustrates the change in the part aspect.

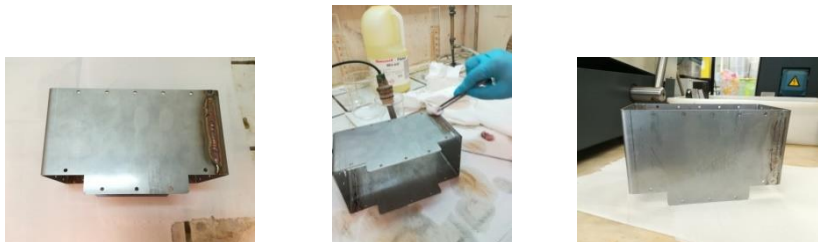


Fig. 42 - Left: the casing middle frame after being welded. Center: the casing middle frame during the passivation process. Right: the casing middle frame after the passivation process.

In order to better transport the equipment during inspections, a *Peli 1610* case (in Fig. 43) was ordered at *RF Caixas* website, which was the official Portuguese reseller of *Peli Cases* [98]. It was a very resistant case of 63 cm x 50 cm x 31 cm, specially created to work in the Industry, and was purposely chosen with wheels, for the transportation to be easier.



Fig. 43 - Peli 1610 Case.

After the cables were working correctly, the whip, encoder and probe external cables and the Steel string were coupled together using the heat resistant sleeve, in what could be called a umbilical cord. Then, the scanner was properly assembled and the equipment was ready to be tested. Fig. 44 shows the fully assembled scanner (inside and outside view) and the equipment inside the *Peli* case (the umbilical cord was around the scanner and the *PowerBox H*). An SD card (which was already

available at the *Non Destructive Testing Laboratory*) to save each inspection recording, was also added to the case. Due to its magnetic affinity to Carbon Steel structures, and as it had 3,1 Kg, the scanner prototype could easily be coupled to the test specimens to perform vertical and upside-down inspections, as required by *ISQ* customers.



Fig. 44 - Left: scanner prototype inside view. Center: the equipment in its respective travelling case. Right: scanner prototype outside view.

The equipment was then ready to be properly tested and its respective functionalities validated.

## 3.2. Scanner prototype validation

Then, the *EMAT Heat Inspection* equipment had to be validated in order to check if it could successfully perform the inspections it was designed to do, fulfilling all the desired requirements that were initially proposed by the *ISQ* clients.

### 3.2.1. Construction of validation equipment

The first step was to create proper apparatus to successfully perform the validation tests. To do that, it was important to revise the customer requirements to which the tests were dependant:

- Detect defects with minimum diameter of 16 mm and depth of 50% of the nominal specimen thickness (from 10 mm to 30 mm) up to 400 °C.
- Detect thickness discontinuities of at least 4 mm depth in structures of 10 mm nominal thickness up to 400 °C.
- Minimum scanning speed of 15 mm/s.
- Generate Corrosion Mapping Reports (A-Scan and C-Scan).

In order to perform tests with increased temperatures, a heating box was specially created for the purpose.

The case was made by 4 s-shaped bent plates, of Stainless Steel (produced by *Lasindustria*),



having a Stainless Steel thick plate as base, and an interior with 10 mm Superwool insulating board on each wall and on the base (Superwool was a material with very low thermal conductivity and resistant to temperatures up to 900 °C, which was ideal to retain the heat generated inside the box [99]) and four resistors of 5 nuclei each, which had Ø32 mm, length of 275 mm, 230 V and 1000 W each. They were supported by a Stainless Steel structure, threaded to the base.

The box was designed so that various test blocks with different thicknesses and defects could be easily inserted and removed from the top of the box (Fig. 45, left), being able to lodge up to six blocks of 40 mm width at the same time. The blocks would be heated by the resistors, having a temperature range from 25 °C (room temperature) to 400 °C due to a power regulator which was already installed at the *Non Destructive Testing Laboratory*. Then, the scanner would be put on top of the blocks, and performed various inspections at increasing temperatures for its results to be validated. A structure made of Aluminium profiles was put on top of the heating box (as in Fig. 45, right) to limitate the starting and ending point, so that these measures would be the same for every inspection performed.

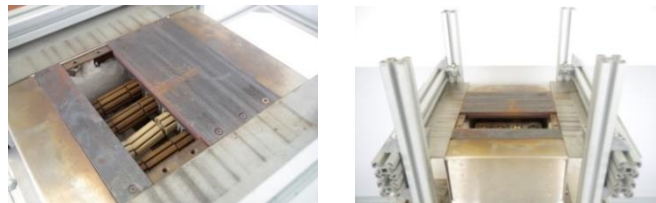


Fig. 45 - Left: various testing blocks on top of the heating box. Right: structure of aluminium profiles on the heating box.

On the various Low Carbon Steel blocks, they were designed according to the ultrasonic beam profile of the EMAT probe (Chapter 2.3), which exposed that the minimum detectable defect diameter would be around 16 mm. Basically, they could be divided in three categories:

1<sup>st</sup> Category - Five blocks for defect detection of different thicknesses: 10 mm, 15 mm, 20 mm, 25 mm and 30 mm. They all had the same length (248 mm) and width (40 mm), and five blind flat bottom holes of Ø12 mm, Ø14 mm, Ø16 mm and Ø18 mm, all having the same disposition as in Fig. 46. The depths of the holes were the following:

- a. 5 mm for the 10 mm thickness block.
- b. 7,5 mm for the 15 mm thickness block.
- c. 10 mm for the 20 mm thickness block.
- d. 12,5 mm for the 25 mm thickness block.
- e. 15 mm for the 30 mm thickness block.

That is, all the hole depths corresponded to the critical depth for each respective thickness.

2<sup>nd</sup> Category - One stair block, of 248 mm length and 40 mm width, which had various steps with thicknesses ranging from 12 mm to 30 mm, in 2 mm intervals, as depicted in the scheme of Fig. 47. This block would allow to verify to what extent the scanner was sensible to thickness variations.

3<sup>rd</sup> Category - One large block of 10 mm thickness with 248 mm length and 80 mm width, which had three blind flat bottom holes of 2 mm, 3 mm and 4 mm depths and Ø40 mm each

as seen in Fig. 48. This would permit to study how the scanner was sensible to depth variations at the minimum nominal thickness required.

The distance between defects was enough to guarantee no overlap of detected signals, according to the ultrasonic beam profile of the probe in Chapter 2.3 (also, the blocks were manufactured by *MJ Branco*).

In order to check the surface temperature of each block on top of the heating box, a thermometer *Kane May KM 3000* with thermocouple was used. The thermocouple was put in direct contact with the inspected surface and its temperature was displayed in the thermometer in a matter of seconds.

The four 1000 W resistors inside the heating box granted an even distribution of temperature along the length of each block, with maximum variance of 5 °C.

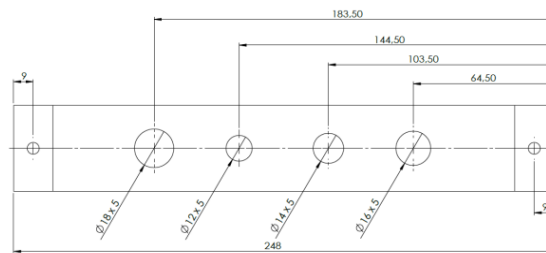


Fig. 46 - Drawing scheme of the hole configuration for all 1<sup>st</sup> category inspection blocks (bottom view); the holes near de edges were made to screw the bars on the heating box.

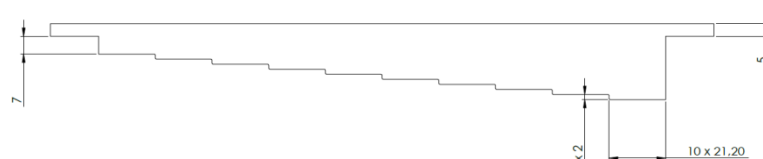


Fig. 47 - Drawing scheme representation of the 2<sup>nd</sup> category inspection block (side view).

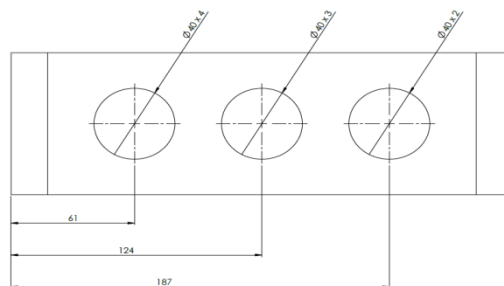


Fig. 48 - Drawing scheme of 3<sup>rd</sup> category validation block (bottom view).

After the validation equipment was ready, *PowerBox H* settings needed to be properly adjusted, so that the scanner could work at best conditions.

### 3.2.2. PowerBox H set up

In order to proceed with the tests, correct adjustment of the *PowerBox H* settings was mandatory to achieve best results.

Of course, the *PowerBox H* settings would depend on various factors such as the specimen used, but for the sake of comprehension, a standard procedure was described for a 10 mm thickness block with four defects of 5 mm depth each, belonging to the first category of blocks which was described in the previous chapter.

First, the right configuration file needed to be chosen. These configurations were provided by *Innerspec* and updated each year, having settings preferences which optimize the equipment for a certain inspection. This would depend on the test specimen, environmental conditions and also on the used probe (which in this case was made to produce horizontally polarized shear waves, as seen in Chapter 2.3). For the 10 mm Carbon Steel block which was tested for defect detection and thickness measurement, the preferred configuration was *TM\_MC\_SH\_1\_50mm.cfg*. *TM* meant thickness measurement (the inspection operation), *MC* meant Medium Carbon (the material of the test specimen), *SH* meant Shear Horizontal (the kind of waves produced by the probe during the inspection), and 1 to 50 mm meant the inspected material thickness range to which that configuration was suitable to be used. Nevertheless, the settings preferences provided by the configuration files were merely a reference, therefore user experience was required to adapt each settings to the specific inspection conditions.

The intended inspection format was A-Scan plus C-Scan, which allowed to study the presence of discontinuities such as the ones presented in the aforementioned blocks.

The A-Scan in this equipment displayed its signals in a plot where the abscissa measured the depth of a certain discontinuity in mm (as the equipment measured the travelling time, also known as time of flight (TOF) of the received signals, and by having the specific material velocity, it furtherly converted the time into a depth scale), and the ordinate gave the amplitude of the received echo signals in percentage (%). On the C-Scan, the abscissa and ordinate were related to the inspection length and the test specimen width, respectively. Then, it was necessary to comprehend each *PowerBox H* functionality. Fig. 49, left shows a print screen of a typical TX/RX menu of *PowerBox H*, which dealt with all the factors concerning transmission and receiving of the signal. Fig. 49, right shows the probe datasheet chart of signal response along frequency (as in [74]).

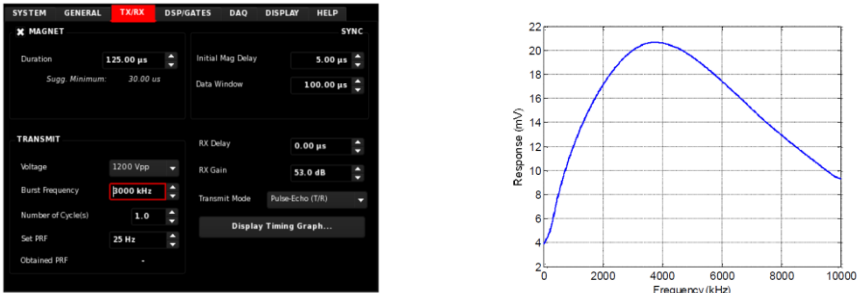


Fig. 49 - Left: printscreen of a typical TX/RX menu of *Innerspec PowerBox H*. Right: probe datasheet chart of signal response (mV) and frequency (kHz) for *Innerspec High Temperature Sensor SH Spiral* [74].

*Duration* corresponded to the length of time when the magnet was on, and the used value was 120  $\mu\text{s}$ , as it was above the suggested minimum value and always gave consistent results.

*Voltage* was the transmission voltage, so 1200 Vpp was used for the equipment to work in full-power.

*Burst Frequency* was the frequency of the transmitted signal, and as the chart in Fig. 49, right suggests, 3800 kHz was the value which granted best response for this probe.

*Number of Cycles* gave the number of electromagnetically cycles per signal burst, and a value of 1.0 gave the best results.

*Set PRF* was the theoretical Pulse Repetition Frequency, and experience with this probe has shown that above 100 Hz (approximately) there were no changes on the signal response, as the Pulse Repetition Frequency depended on the probe's characteristics, which were limited by a physical maximum, so the used value was 100 Hz.

*RX Delay* set the time space which would be omitted in the A-Scan - for example, if 8  $\mu\text{s}$  was set, the A-Scan would omit the first 8  $\mu\text{s}$  of the chart, being good to eliminate parasitic ramp-up echoes; the used value was around 7  $\mu\text{s}$  (as it depended on the temperature).

*RX Gain* was the received signal Gain, a measure of the sound intensity traditionally given by the ratio between the incident ultrasonic wave and the reflected ultrasonic wave at a certain discontinuity, as seen in the following equation:

$$G_R = 20 \log_{10} \left( \frac{P_I}{P_R} \right) \quad (5)$$

Where  $G_R$  was the received Gain (expressed in dB),  $P_I$  and  $P_R$  were respectively the acoustic pressures of the incident and reflected wave on a given discontinuity (which could be expressed on a percentage of amplitude). *RX Gain* would be adjusted according to the temperature for best results (in that particular case, its values could range from 90 dB to 100 dB).

*Initial Mag Delay* set the available time to let the magnet ramp up the magnetic field (5  $\mu\text{s}$  allowed consistent results).

*Data Window* was the range of the A-Scan x-axis (for that particular specimen, 20  $\mu\text{s}$  was sufficient to see the initial pulse and the first back wall echo, and it was shown in a time base because the A-Scan x-axis could also be expressed in a time scale).

*DSP/Gates* was the menu where the influence of certain algorithms could be controlled (Fig. 50, left).

*Coincidence* represented an algorithm to prevent the impact of external noise on the received signal. A value of 5 was enough to counteract that effect.

*Average* represented an algorithm that computed the average of various signals along a certain time frame, and presented the averaged signal in the A-Scan, so that more consistent results could be presented. A value of 16 granted decent signals (higher *Average* values increased the processing work, which tended to slow down the equipment).

*Gates* allowed to measure the distance of certain signals within the A-Scan, whether it could be between two signals or from a specific signal to the A-Scan origin, for example. This made it possible to determine the depth of a certain discontinuity, which was mandatory to detect critical

depths. On the following studies, only one gate was used, which was *Gate 2 (Flaw)*, as seen in Fig. 50, left because it could simultaneously measure the test specimens thicknesses and the flaws depths.

There were various gate algorithms, which could be chosen in *Model/Algo* of the *Gate Parameters* menu (Fig. 50, right shows it for *Gate 2*). The algorithm that was used with this particular block was *First Peak*, which detected the first peak that crossed the threshold within the gate range, and calculated its relative distance to the scan origin which was shown above the A-Scan. Fig. 51, illustrates an A plus C Scan of that particular test specimen at 50 °C, where the green gate was measuring the second back wall echo using *First Peak*). Another gate algorithm worth mentioning was *Peak to Peak*, which calculated the distance between the two highest peaks within the gate range (therefore, the gate threshold had no influence when using this algorithm).

*Minimum Thickness* set the minimum detectable thickness and was left as 1,5 mm. Thus, the *Start*, *Range*, and *Threshold* of a gate were important settings in order to correctly perform the desired measurements when using *First Peak*, so the typical used values for that particular case were 8,50  $\mu\text{s}$ , 5,50  $\mu\text{s}$  and 29 % respectively (*Start* and *Range* values were expressed in  $\mu\text{s}$  because the A-Scan could also be shown on a time scale, as already mentioned).

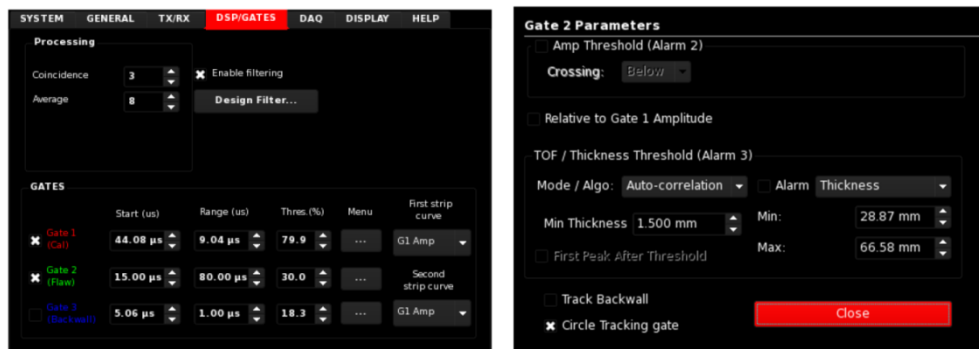


Fig. 50 - Left: printscreen of typical *DSP/Gates* menu of *Innerspec PowerBox H*. Right: printscreen of typical *Gate 2 Parameters* menu of *Innerspec PowerBox H*.

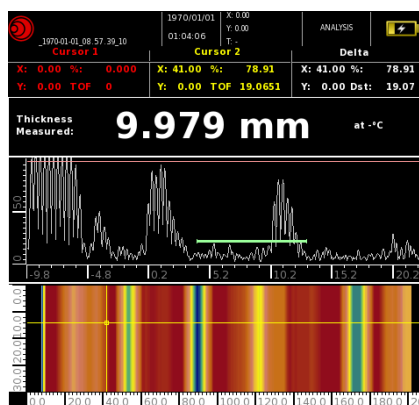


Fig. 51 - Printscreen of A plus C Scan of the 10 mm block at 50 °C performed with *Innerspec PowerBox H*, where the green gate (*First Peak*) can be seen on the A-Scan.

Then, *DAQ* was the last menu regarding important settings for the scanner functioning (Fig. 52).

*DAQ Range* was the same as *Data Window* (used value was 20  $\mu\text{s}$ ).

*Sampling Frequency* was the sampling frequency of the received signal, being 50 MHz the most adequate value considering the dimensions of the probe's coil (as higher values gave worse signal response).

The *Probe Zero* adjusted probe time offset due to electronic delays, and was left at 0  $\mu\text{s}$  which didn't interfere with the results.

*Axis 1 (X/Scan)* was mandatory to be enabled for the encoder to work. The *Start* and *Stop* were the length starting and stopping points of the inspection at which the encoder automatically turned on and off, respectively (*Start* was 0 mm and *Stop* was 210 mm, based on the position of the probe centre at the beginning and end of the block test). *Pitch* specified the dimension interval between which each A-Scan was recorded on a specific point (in that case, 0,5 was used, which meant an A-Scan was recorded at every consecutive 0,5 mm of length, from 0 mm to 210 mm).

*Axis 2 (Y/Scan)* was related to the inspected width, so that *Start* should be 0 mm and *Stop*, as well as *Pitch*, should have the same dimensions as the block width, which was 40 mm. The correct introduction of *Axis 1* and *Axis 2* values would allow the creation of a correct C-Scan.

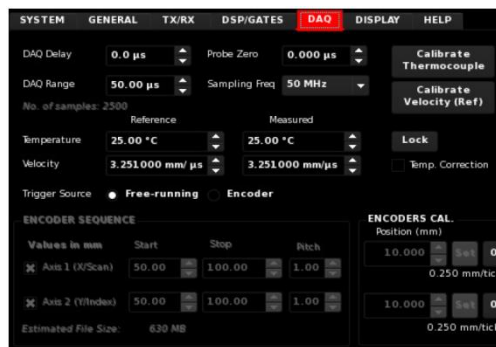


Fig. 52 - Printscreen of typical DAQ menu of *Innerspec PowerBox H*.

At last, on the *Display* menu (Fig. 53), *Distance in  $\mu\text{s}$*  option was unticked, for the x-axis on the A-Scan to be on a depth scale, *Thickness Measurement* was ticked (as that was the main inspection function), and *C-Scan Content* was at *TOF*, so that when creating the C-Scan, the A-Scan value which would be converted was the time of flight on each respective point, giving more consistent C-Scan results as they were directly correlated to thickness measurements. Whereas, if *Peak* was chosen in *C-Scan Content*, the A-Scan value which would be converted to a colour code in the C-Scan was the peak amplitude on each respective point, which could be changed manually by increasing or decreasing the gain, to which it was dependant.



Fig. 53 - Printscreen of typical *Display* menu in *Innerspec PowerBox H*.

The following step was to properly calibrate the encoder and the probe.

### 3.2.3. Probe and Encoder calibration

The scanner calibration for inspection on high temperature surfaces would obviously depend on the temperature of the surface to be inspected.

In order to do that, the desired test block (for the sake of convenience, the 10 mm block of the 1<sup>st</sup> category was used as an example, though the general calibration procedures were similar for every block) was put on top of the heating box, which was turned on.

The power regulator was set for the resistors to reach the desired temperature, which was checked on the block surface using the thermocouple (three points were always measured, one in the middle and two near both endings, to ensure if there was an even distribution of temperature along the block length).

As the compressed air which leaves the scanner from the probe tended to cool down the blocks, decreasing its temperature by 25 °C at equilibrium state (the value was equal for every tested block), the block temperature needed to be set up 25 °C higher than the desired temperature (for example, if testing was meant to be done on a certain block at 125 °C, its temperature needed to reach 150 °C, as the scanner would later cool the block down at the desired temperature of 125 °C).

The scanner was properly placed on top of the heating box in order for the calibration to be performed, so that the probe edge was tangent to the block ending, as depicted in the scheme of Fig. 54 (which was simplified showing just the probe and the block in a bottom view for better understanding). The system was turned on and the gate was correctly placed on the second back wall echo of the A-Scan.

Then, on the *DAQ* menu of *PowerBox H*, *Calibrate Velocity (Ref)* was accessed. *Temperature Ref* was unticked and the block nominal depth was added (in this case, 10 mm), allowing the system to associate the peak of the second back wall echo with the nominal block depth, successfully performing the calibration on that point. As *First Peak* gate was used, two points were necessary to perform the calibration, so the probe was then placed on the opposite block ending along its length, under the same circumstances of the first point, and the nominal depth was added again (if *Peak to Peak* was used, just the first point was necessary to perform the calibration).

On the following tests, the depth of every defect echo would be measured in proportion to the depth of the second back wall echo, so the calibration for that specific temperature was completed. Every time the temperature (or testing block) changed, the same calibration procedure was performed.

The first back wall echoes were not used during the validation tests because the echoes of the defects tended to get covered by parasitic ramp-up echoes, due to their proximity to the A-Scan origin.

All the calibration procedures, as well as all the validation tests, were made with a lift-off (distance from the probe bottom to the specimen surface) of zero, in order to have the best possible transducer efficiency, as recommended by Hirao and Ogi [41].

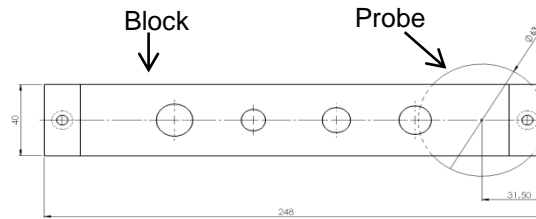


Fig. 54 - Simplified scheme of the first calibration position for 1<sup>st</sup> category 10 mm block (bottom view).

For calibrating the encoder, a plain, smooth e clear surface was chosen, where the desired calibration length was marked (in that case, the starting point and the end point at 500 mm were marked). The *Encoder* mode was chosen in *PowerBox H*, the probe centre of the scanner was put on the starting point and the calibration position was set to zero. Then, the calibration length value of 500 mm was added and the scanner was turned on to travel the calibration distance. When the probe centre reached the end point, the scanner was stopped and its position set on the display, giving an output value for that specific calibration in mm/tick, that is, displacement per tick (being tick one half of a pulse [76]).

After several calibrations, an average of the output calibration values could be found, which in that case was 0,146 mm/tick (with a minimal deviation of 0.001 mm/tick). That preset value was set on the calibration display, in order to avoid performing calibrations before each validation test.

Finally, the testing plan needed to be specified for the validation conditions to be fully known.

### 3.2.4. Prototype Testing Plan

The creation of a testing plan was mandatory to establish how the validation tests would be conducted, and what would be furtherly studied with the obtained results.

For the matter, the following tests were proposed for each block category:

#### 1<sup>st</sup> Category

- a. Study of the behaviour of the signal amplitudes related to the nominal thicknesses and defect depths along increasing temperatures, from 25 °C to 400 °C in intervals of 25 °C. That would validate the equipment detectability of critical depths at higher temperatures.
- b. Study of the equipment capability for defect dimensioning, comparing the defect diameter results obtained during the tests, with the real flaw diameters, at increasing temperatures from 25 °C to 400 °C, in 25 °C intervals.
- c. Study of the signal to noise ratio (SNR) regarding nominal thicknesses and defect depths at increasing temperatures from 25 °C to 400 °C, in 25 °C intervals.

#### 2<sup>nd</sup> Category

- a. Study of the signal amplitudes related to the different thicknesses at increasing temperatures, from 25 °C to 400 °C, in 25 °C intervals, analysing the equipment detectability of back wall thicknesses at increasing temperatures.



- b. Study of the signal-to-noise ratio (SNR) regarding different thicknesses at increasing temperatures from 25 °C to 400 °C, in 25 °C intervals.

### 3<sup>rd</sup> Category

- a. Study of the signal amplitudes related to the nominal thickness and defect depths at increasing temperatures, from 25 °C to 400 °C, in 25 °C intervals, allowing to understand the equipment detectability of different flaw depths at increasing temperatures.
- b. Study of the signal-to-noise ratio (SNR) regarding nominal thickness and flaw depths at increasing temperatures from 25 °C to 400 °C, in 25 °C intervals.

There were various definitions for the signal-to-noise ratio, but one which was usually used in industrial context was, on a given A-Scan, the difference between the peak amplitude of a certain signal and the estimated peak amplitude of the noise, as in the following formula:

$$SNR = \frac{A_S}{A_N} \quad (6)$$

Where  $SNR$  was the signal-to-noise ratio (dimensionless),  $A_S$  was the peak amplitude of a certain signal and  $A_N$  the estimated peak amplitude of the noise [54][100]. Thus, SNR behaviour would allow to monitor the influence of noise on the obtained results.

All the conditions were then met in order to proceed with the validation tests.

### 3.2.5. General Test Procedure

All the validation tests were performed in the *Non Destructive Testing Laboratory of ISQ Group*, using the equipment presented in the previous chapters.

The general test procedure for each category of blocks was the following:

1. Place the blocks on top of the heating box.
2. Set the scanner prototype and the *PowerBox H*, placing the scanner on the first block of the row and adjusting all the *PowerBox H* configurations as previously specified.
3. Calibrate the scanner prototype for the first block as seen previously.
4. Perform the inspection at room temperature (25°C) for the given block.
5. Repeat the same procedure at room temperature for the next blocks.
6. Turn on the heating box and set the power regulator to match the desired temperature (first, at 75 °C<sup>2</sup>, so that with the influence of the air cooling, the blocks could be inspected at 50 °C,

---

<sup>2</sup> As previously seen, the probe could perform inspections without air cooling up to 200 °C, but as a matter of precaution, air cooling was used in all inspections except at room temperature.

as already explained) using the thermocouple to monitor the block temperature as suggested previously (Fig. 55).



Fig. 55 - Temperature check using the thermocouple.

7. Turn on the air cooling,
8. Place the scanner on top of the first block and move the scanner along the block until a temperature equilibrium of 50 °C is reached.
9. Perform the inspection on the given block at 50 °C (as exemplified in Fig. 56)



Fig. 56 - Inspection on a given block.

10. Repeat the same procedure at 50 °C for the next blocks.
11. Repeat the procedure for the following temperatures up to 400 °C, at 25 °C intervals.

The tests were conducted on all the previously referred blocks, for the respective results to be properly studied and to conclude if the scanner effectively met all the customer requirements.

### 3.2.6. Study of results

After the validation tests, the best respective A-Scan and C-Scan recordings were analysed, and various methods needed to be adopted in order to treat the obtained results.

For the first category of blocks, maximum signal amplitudes related to defects of critical depths and back wall echo amplitudes over the same point, both along increasing temperatures, were presented in various charts divided by different groups, being the scheme presented by the following Table 1:

Block Nominal Thickness \ Echo	10 mm	15 mm	20 mm	25 mm	30 mm
Ø12 mm defect	A vs. T (25°C – 400°C)	A vs. T (25°C – 400°C)	A vs. T (25°C – 400°C)	A vs. T (25°C – 400°C)	A vs. T (25°C – 400°C)
Ø14 mm defect	A vs. T (25°C – 400°C)	A vs. T (25°C – 400°C)	A vs. T (25°C – 400°C)	A vs. T (25°C – 400°C)	A vs. T (25°C – 400°C)
Ø16 mm defect	A vs. T (25°C – 400°C)	A vs. T (25°C – 400°C)	A vs. T (25°C – 400°C)	A vs. T (25°C – 400°C)	A vs. T (25°C – 400°C)
Ø18 mm defect	A vs. T (25°C – 400°C)	A vs. T (25°C – 400°C)	A vs. T (25°C – 400°C)	A vs. T (25°C – 400°C)	A vs. T (25°C – 400°C)
Back Wall	A vs. T (25°C – 400°C)	A vs. T (25°C – 400°C)	A vs. T (25°C – 400°C)	A vs. T (25°C – 400°C)	A vs. T (25°C – 400°C)

Table 1 – Arrangement of results for 1<sup>st</sup> category blocks.

Where *A* stands for Amplitude and *T* stands for Temperature, which ranged in 25 °C intervals.

As an example, Fig. 57, left shows an A+C Scan acquisition made to a 20 mm block of the 1<sup>st</sup> category at 125 °C. The A-Scan showed the gate over the second back wall echo (which correspondent value was above), and on the C-Scan, the stripes in blue represented the various defects (except the first blue stripe at left, that corresponded to an initial period when the probe was not yet on the inspected zone, but at the block edge which fits it on top of the heating box, as seen in Fig. 45) and the orange stripes represented the nominal thickness.

Fig. 57, right shows an A+C Scan on a 25 mm block of the 1<sup>st</sup> category at 200 °C, where the orange stripes on the C-Scan depicted each defect (critical depth was 12,5 mm), and the blue stripes represented the nominal thickness. The A-Scan represented the gate over the second echo of the defect of Ø16 mm.

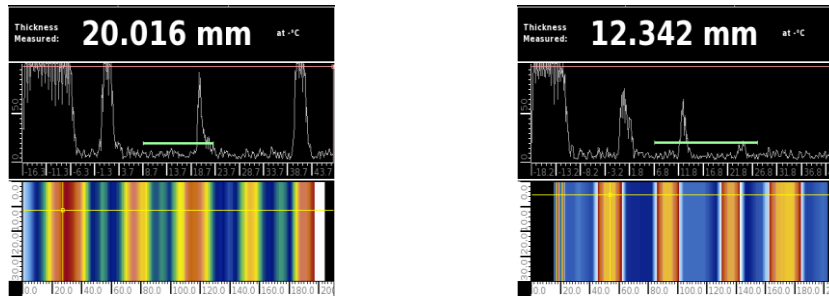


Fig. 57 - Left: A+C Scan of 20 mm block of the 1<sup>st</sup> category at 125 °C using *Innerspec PowerBox H*.  
Right: A+C Scan of 25 mm block of the 1<sup>st</sup> category at 200 °C using *Innerspec PowerBox H*.

As already mentioned, all A+C Scans were done on the second back wall echoes and second defect echoes. Also, not all the tests were performed at the same Gain (which was adjusted to every particular case for better results), therefore, the signal amplitudes needed to be reduced to an equal Gain basis, using the following equation:

$$A_b = \frac{A_o}{10^{\left| \frac{G_o - G_b}{20} \right|}} \quad (7)$$

Where  $A_b$  was the amplitude corresponding to the equal Gain basis  $G_b$ , and  $A_o$  was the original amplitude of a certain test at a given original Gain  $G_o$ . This equation was deduced from formula (5), and was mandatory in order to create the same baseline conditions of signal intensity for the generation of amplitude-temperature charts for each of the previous groups, as seen in Fig. 58,

Fig. 59, Fig. 60, Fig. 61 and Fig. 62. The Gain basis used, equal for every test performed on those blocks, was 90 dB.

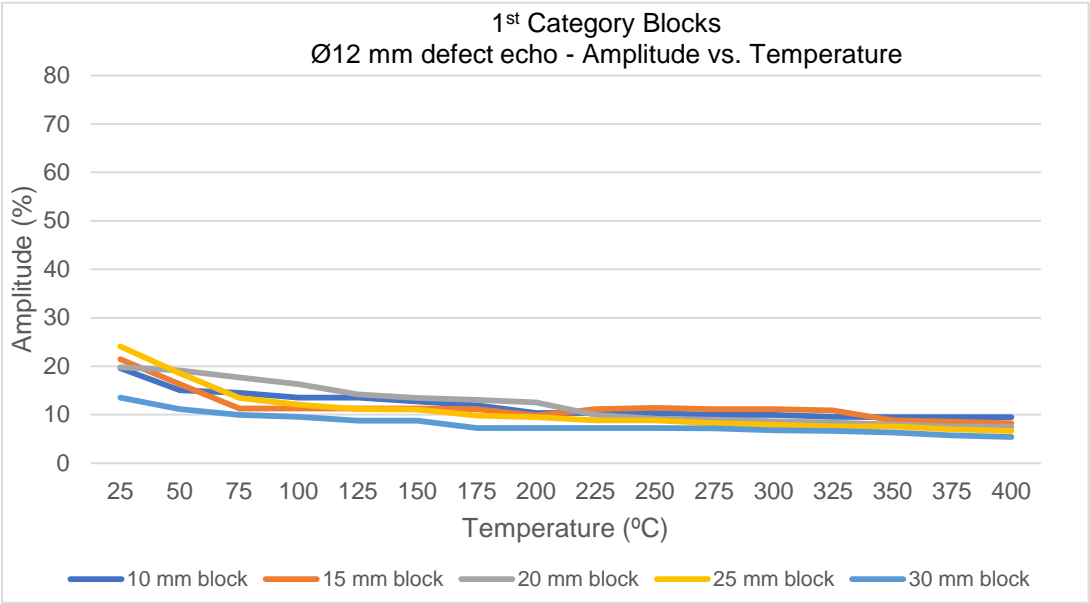


Fig. 58 - Amplitude vs. Temperature for the 1<sup>st</sup> category blocks Ø12 mm defect echo.

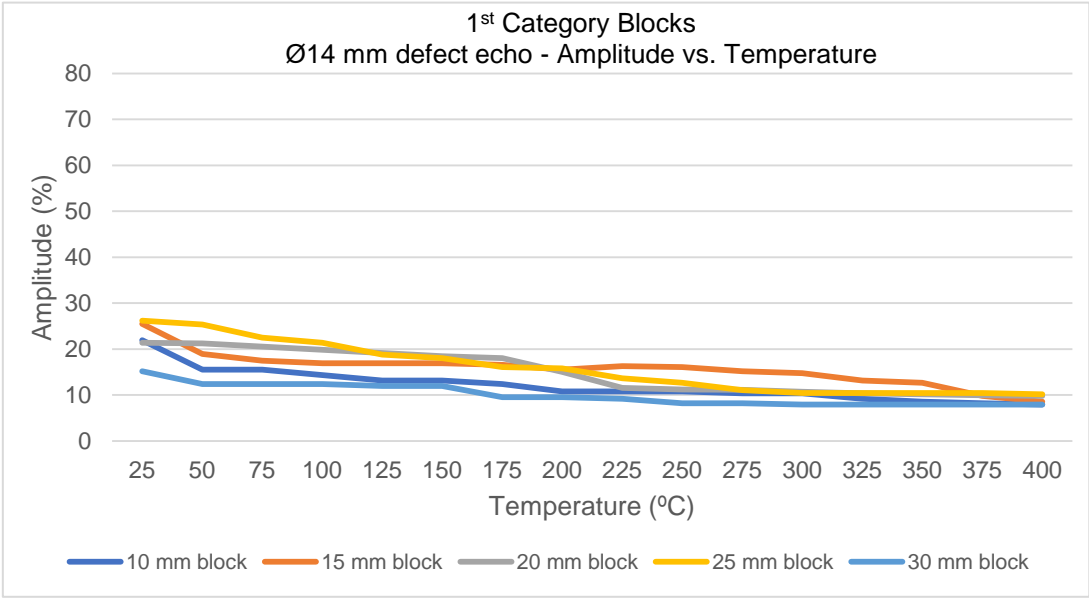


Fig. 59 - Amplitude vs. Temperature for the 1<sup>st</sup> category blocks Ø14 mm defect echo.

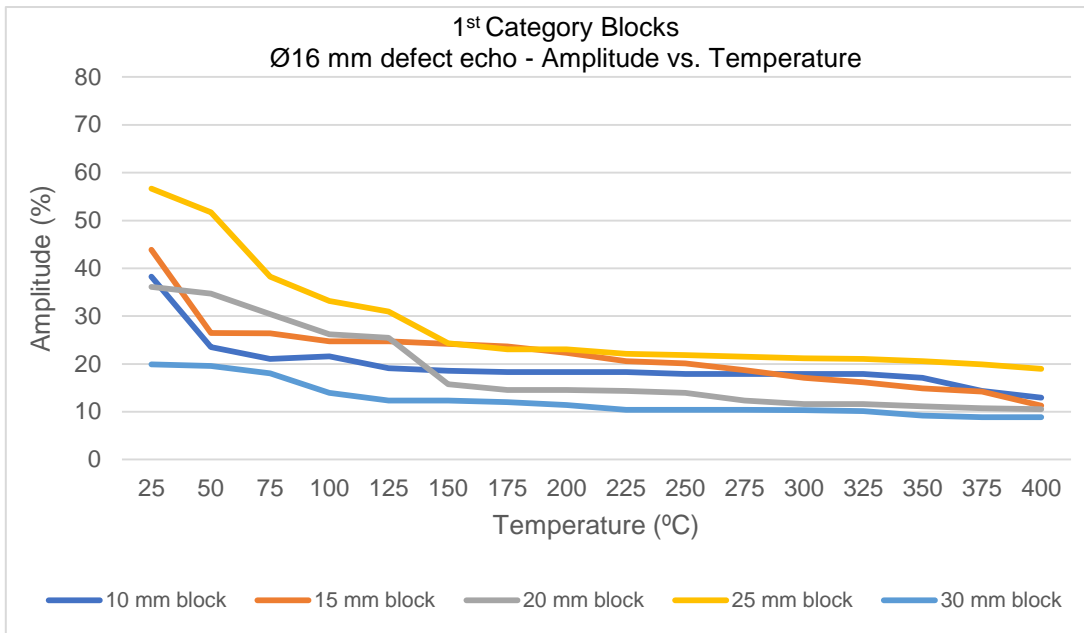


Fig. 60 - Amplitude vs. Temperature for the 1<sup>st</sup> category blocks Ø16 mm defect echo.

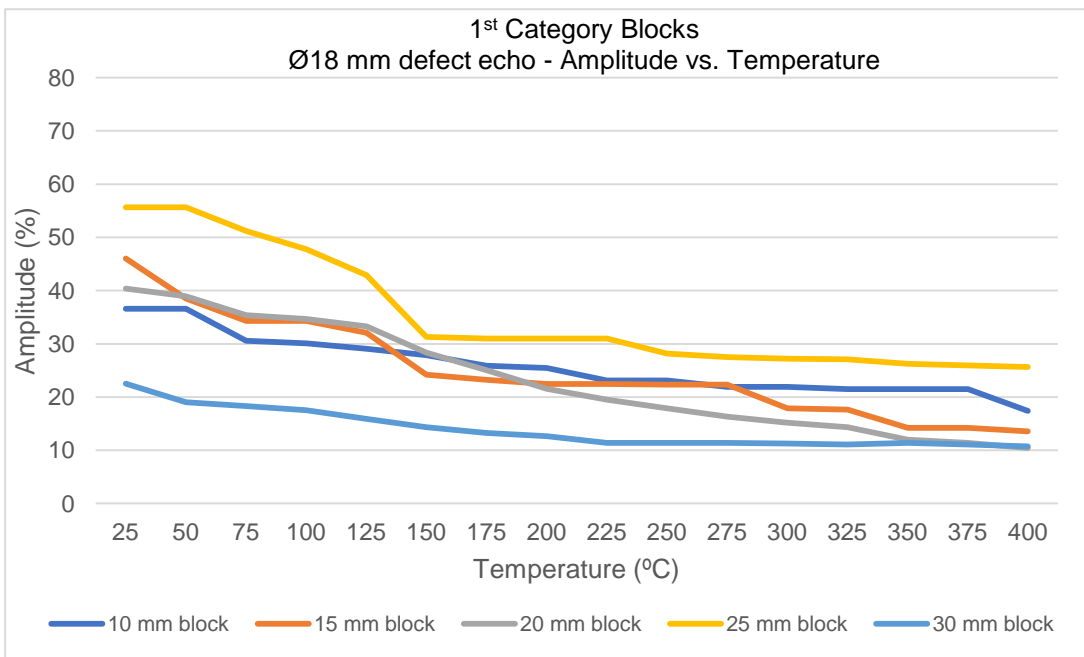


Fig. 61 - Amplitude vs. Temperature for the 1<sup>st</sup> category blocks Ø18 mm defect echo.

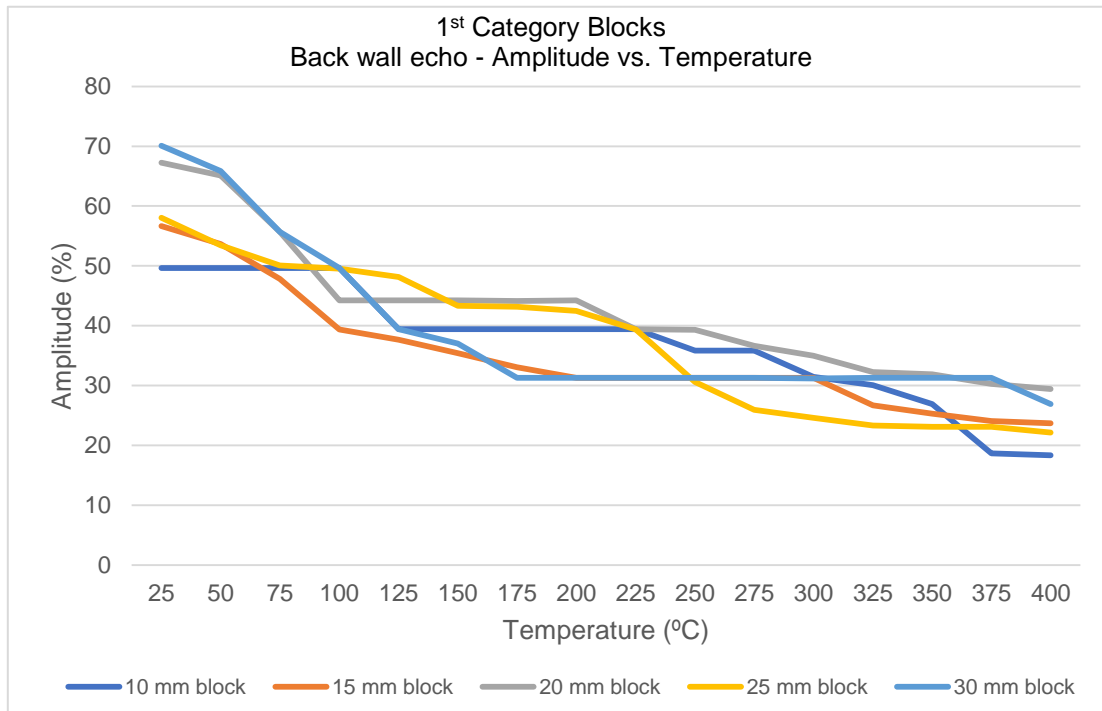


Fig. 62 - Amplitude vs. Temperature for the 1<sup>st</sup> category blocks back wall echo.

As can be noted, all the charts show a descendant tendency of their amplitudes along increasing temperatures, which agreed with the findings of Darbari et al. [101], and Papadakis et al. [102]. That phenomenon was known as attenuation, a decrease in the travelling ultrasonic wave intensity when on a certain tested material, due to the main contributions of scattering and absorption [103].

Absorption happens when part of the travelling ultrasonic waves are converted to heat in the material, but usually, its effect is not significant and can be ignored [104].

Scattering could result from the non-homogeneous nature of many polycrystalline materials, which on its grain limits present discontinuities of different acoustic impedances between mediums, due to variations in density, elastic properties or acoustic velocities [34][103]. Thus, when an ultrasonic wave is passing from one grain to another, part of it is scattered on the grain limit [101]. The energy loss due to scattering effect could depend on the frequency and polarization of the ultrasonic waves, the grain size of the material, and also the anisotropy of the material [101].

The frequency used in all the validation tests was 3800 kHz, the value around which gave the best response from the probe when using Shear Horizontal waves, as previously seen, thus minimizing the scattering effect by that source. As it was exposed by Tripathi and Verma, scattering due to the increase of grain size in Carbon Steels is a phenomenon that starts to occur at 900 °C [105], well above the temperature range of the performed tests, therefore it shouldn't be taken in consideration. And finally, Low Carbon Steel is an isotropic material (having identical properties in all directions [106]), so scattering due to anisotropy didn't apply on that case.

Scattering could also be caused by vibrational interactions between the travelling ultrasonic waves and the microstructures of the materials, which (in a general manner) increase with temperature, thus being the major cause of attenuation on the given temperature range, as stated by

Lunn et al. [107].

The presence of defects could also promote scattering of the travelling ultrasonic waves due to geometrical discontinuities along the tested specimen [103], and that was clearly the case with first category blocks, which imposed the use of higher Gain values to counteract its effect on amplitude reduction.

Also, most charts showed that amplitude had an accentuated drop from 25 °C to about 200 °C – 225 °C, from which it demonstrated a narrower decrease up to 400 °C. The slight decrease in attenuation tendency when it reached between 200 °C to 225 °C was precisely due to a reduction in microstructural oscillations of cementite ( $Fe_3C$ , a typical constituent of Carbon Steels, at temperatures below 727 °C, as seen in Fig. 63, knowing that Low Carbon Steels usually contain less than 0,25% weight of Carbon [106]), when its respective Curie Temperature ( $T_c$ ) was reached (around 215 °C) [101][105]. These oscillations enhanced attenuation in a ferromagnetic state but as temperature rose above  $T_c$ , cementite became paramagnetic and the oscillations became weaker, therefore attenuation became subtler [101][108].

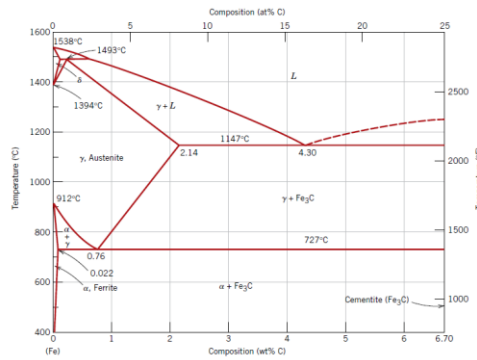


Fig. 63 - Phase diagram of iron-iron carbide, also known as cementite [106].

The respective linear regression equations of each chart were then organized on the following Table 2:

Block \ Echo	Defect				
	Ø12 mm	Ø14 mm	Ø16 mm	Ø18 mm	Back wall
10 mm	$A_{10} = -0,528T + 16,357$	$A_{10} = -0,6873T + 17,889$	$A_{10} = -0,8648T + 26,915$	$A_{10} = -1,1053T + 35,269$	$A_{10} = -2,0328T + 54,314$
15 mm	$A_{15} = -0,4817T + 15,661$	$A_{15} = -0,7104T + 21,718$	$A_{15} = -1,3923T + 33,676$	$A_{15} = -1,8888T + 41,034$	$A_{15} = -1,9282T + 51,379$
20 mm	$A_{20} = -0,8655T + 19,493$	$A_{20} = -0,9406T + 22,891$	$A_{20} = -1,6979T + 32,806$	$A_{20} = -2,1435T + 41,634$	$A_{20} = -2,2249T + 61,606$
25 mm	$A_{25} = -0,8198T + 17,736$	$A_{25} = -1,1337T + 25,46$	$A_{25} = -2,0127T + 45,128$	$A_{25} = -2,1112T + 53,269$	$A_{25} = -2,5866T + 59,499$
30 mm	$A_{30} = -0,4137T + 11,564$	$A_{30} = -0,4508T + 13,845$	$A_{30} = -0,6851T + 18,208$	$A_{30} = -0,6887T + 19,807$	$A_{30} = -2,3764T + 59,336$

Table 2 - Linear regression equations of Amplitude versus Temperature charts for various defect and back wall echoes, at different nominal thickness blocks.

$A_{10}$  to  $A_{30}$  represent the amplitudes and the nominal thickness of each respective block, and  $T$  represents temperature.

As it was noted by the behaviour of the charts and by the linear regression equations along the table columns from left to right, amplitudes regarding echoes of defects tended to increase with flaw diameters, which corroborated what was generally presented in the ultrasonic beam profile provided by the manufacturer. Smaller defects of  $\varnothing 12$  mm and  $\varnothing 14$  were more difficult to detect.

Furthermore, it was also seen that, as defect diameters increased, the linear regression equations of the defects tended to approach the equations of the nominal thicknesses (and when defect diameters decreased, the linear regression slopes tended to get flatter, hence the increased difficulty to detect smaller defects). Charts also tended to exhibit similar behaviour over the same point (whether it was a defect or back wall).

About the study for critical defect dimensioning on the first category blocks, one of the most commonly used methods for flaw sizing was the 6 dB method [39], which consisted in positioning the probe above the flaw until the maximum defect amplitude was found, after which the amplitude of echoes which represented the beginning and ending of the defect were calculated using the following equation:

$$A_e = \frac{A_m}{10^{\frac{|G|}{20}}} \quad (8)$$

Where  $A_e$  is the amplitude of the echoes marking the beginning and end of the defect,  $A_m$  is the given maximum defect echo and  $G$  is the gain drop which is equal to 6 dB (that was another application of equation (5)). Therefore, it was admitted that a drop of 6 dB over the intensity of the maximum amplitude of the defect echo would give the amplitudes of the echoes between which the defect was present. By using the C-Scan, the block positions, where these echoes were present, could be found, thus giving the flaw dimension [34][109].

Nevertheless, that method was developed to be used in Conventional Ultrasonic Testing. Therefore, experiments with 5 dB, 6 dB and 7 dB drops on the obtained test results have shown that for that particular EMAT probe, using a value of 7 dB in equation (8) instead of 6 dB led to more accurate results.

The following Table 3 shows, for each defect diameter, the percentage share, over the real defect diameter, of the difference between the obtained flaw diameter (according to the aforementioned method), and the real flaw diameter, at the 10 mm block, given by the following formula [109]:

$$P_s = \frac{D_o - D_R}{D_R} \times 100 \quad (9)$$

Being  $P_s$  the percentual share,  $D_o$  the obtained defect diameter and  $D_R$  the real defect diameter. Tables 4 to 7, present in Chapter 7, show the obtained results for 15 mm to 30 mm thickness blocks.



Defect Temperature	Ø12 mm	Ø14 mm	Ø16 mm	Ø18 mm
25 °C	66,67 %	-21,43 %	-37,50 %	-33,33 %
50 °C	-41,67 %	-35,71 %	-25 %	-33,33 %
75 °C	25 %	0 %	-6,25 %	-33,33 %
100 °C	-25 %	-7,14 %	-43,75 %	-27,78 %
125 °C	50 %	-28,57 %	-18,75 %	11,11 %
150 °C	8,33 %	35,71 %	-62,50 %	-11,11 %
175 °C	-8,33 %	-28,57 %	-25 %	-38,89 %
200 °C	33,33 %	-28,57 %	-37,50 %	-22,22 %
225 °C	0 %	-28,57 %	-25 %	-33,33 %
250 °C	83,33 %	50 %	0 %	-27,78 %
275 °C	16,67 %	-28,57 %	18,75 %	-27,78 %
300 °C	0 %	-42,86 %	6,25 %	-33,38 %
325 °C	-8,33 %	-35,71 %	-12,5 %	-33,33 %
350 °C	8,33 %	57,14 %	-18,75 %	-22,22 %
375 °C	-25 %	28,57 %	-31,25 %	27,78 %
400 °C	-8,33 %	35,71 %	-6,25 %	-33,33 %

Table 3 - Percentual share over the real defect diameter of the difference between obtained and real flaw diameters for 10 mm block of the first category.

The negative values meant the obtained diameter was smaller than the real one. And as it was demonstrated, except for a few exceptions where there was no difference (0%), there was great disparity between the obtained results and real dimensions, as most of the percentual differences of defect diameters were well above 20%, reaching in some cases as high as 92,86% of the real defect diameter. Therefore, the prototype was not suitable for defect dimensioning, but that was not a matter of great concern, as what was really important during the kind of inspections for which it was designed to perform, was that it could effectively detect defects of critical depth above the required diameter of 16 mm.

Then, in order to have a final acceptance criteria over the above validation tests, the study of signal to noise ratio (SNR) regarding nominal thicknesses and defect depths at the given temperatures was performed.

It would be common practice for the SNR study to use equation (6) and reject values which were below  $SNR = 3$  [109]. But, as a matter of fact, the classical SNR equation (6) was better suited for Conventional Ultrasonic testing. For EMATs, the following equation should be adopted [107]:

$$SNR_{dB} = 20 \log_{10} \left( \frac{A_S}{A_{AV}} \right) \quad (9)$$

Where  $SNR_{dB}$  was the Signal to Noise Ratio in decibels (dB),  $A_S$  was the peak amplitude of a given signal and  $A_{AV}$  was the is the average value of a number of noise peaks for a region of noise around the signal of  $A_S$ .

The results were presented in the following charts of Fig. 64, Fig. 65, Fig. 66, Fig. 67 and Fig. 68, and the adopted rejection value was  $SNR_{dB} = 20 \log_{10}(3) = 9,54 \text{ dB}$ .

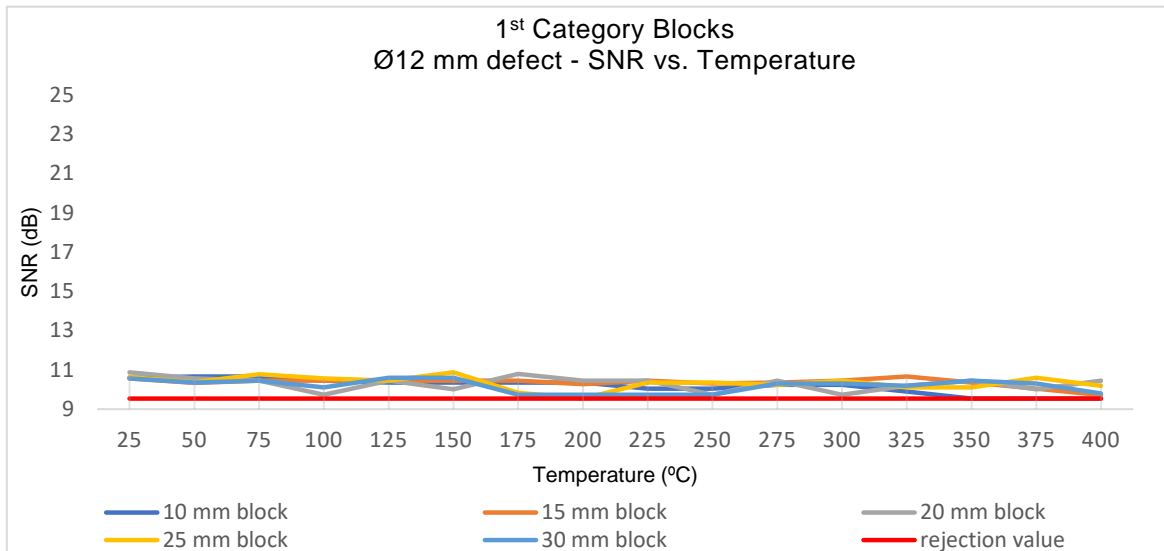


Fig. 64 - SNR vs. Temperature for the 1<sup>st</sup> category blocks Ø12 mm defect echo, along with the respective rejection value.

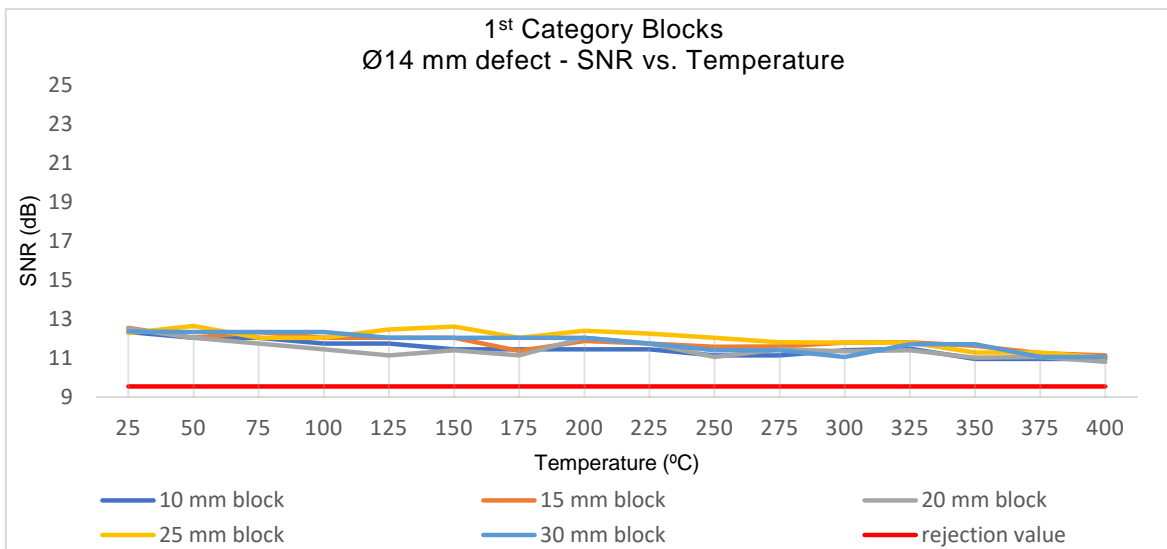


Fig. 65 - SNR vs. Temperature for the 1<sup>st</sup> category blocks Ø14 mm defect echo, along with the respective rejection value.

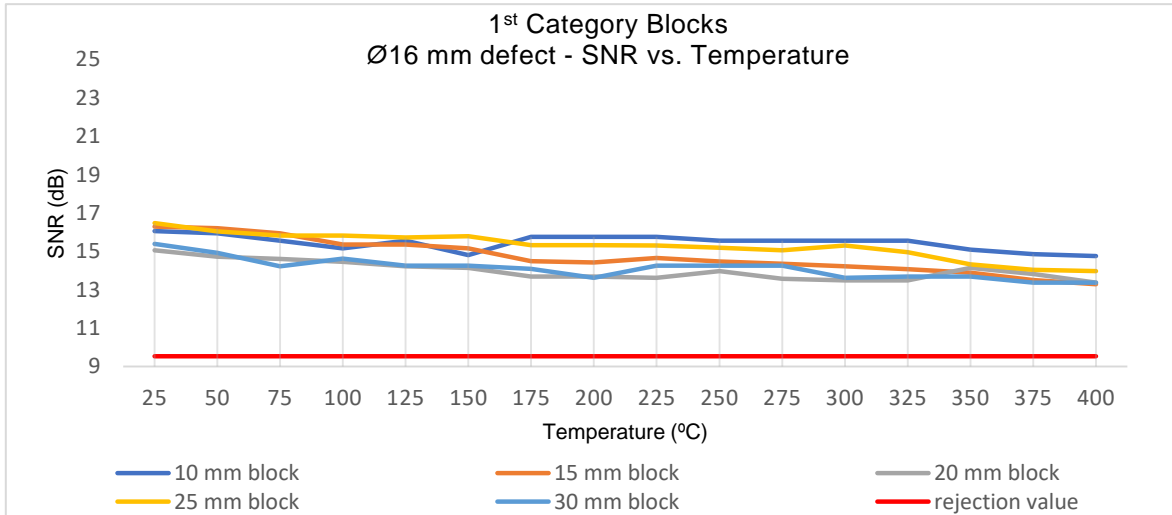


Fig. 66 - SNR vs. Temperature for the 1<sup>st</sup> category blocks Ø16 mm defect echo, along with the respective rejection value.

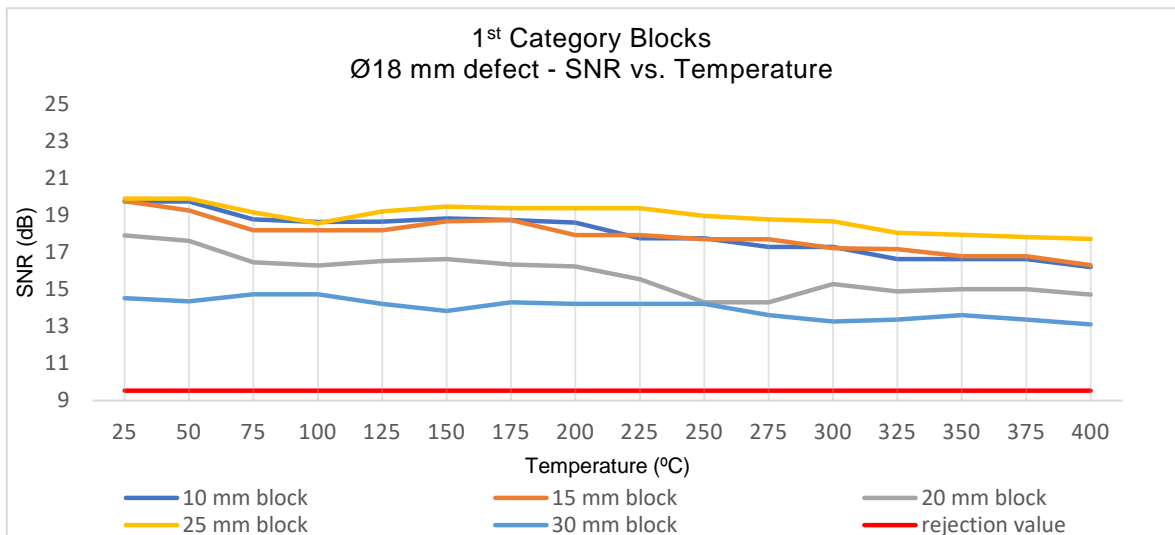


Fig. 67 - SNR vs. Temperature for the 1<sup>st</sup> category blocks Ø18 mm defect echo, along with the respective rejection value.

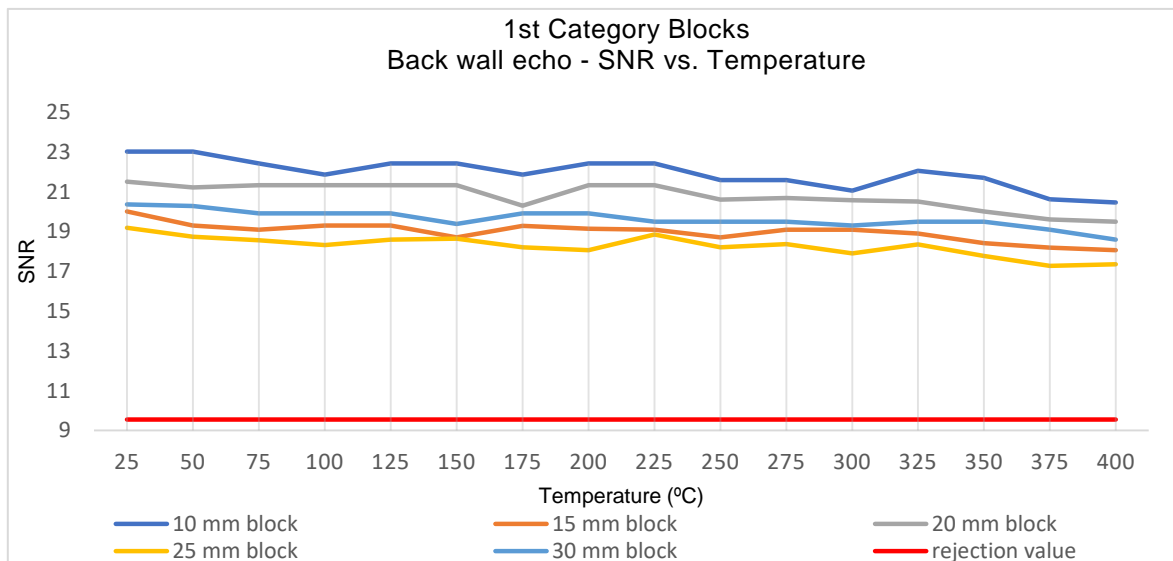


Fig. 68 - SNR vs. Temperature for the 1<sup>st</sup> category blocks back wall echo, along with the respective rejection value.

Noise amplitudes ranged from 5% to 15% during the tests, being the most common values between 7,5% and 10 %. Most charts had a slight descending behaviour, which demonstrated the effect of decreasing amplitudes along higher temperatures. And, as could be seen, SNR decreased with shorter defect diameters, (which was mainly due to the decrease in signal amplitude in smaller defects), tending to approach the Rejection Value of 9,54 dB.

Charts from Fig. 64 show that SNR values from Ø12 mm defects were generally very close (or even equal, as seen in the 10 mm block above 350 °C) to the Rejection Value, which means this equipment wasn't fit to detect defects as short as Ø12 mm.

Fig. 65 shows SNR values from Ø14 mm defects were not as close to 9,54 dB as the previous ones, but a mean value of 11 dB was still low, considering the charts for Ø16 mm defects, with values between 13 dB to 16 dB, and for Ø18 mm defects, ranging from 14 dB to 20 dB.

Because, as SNR values successively decreased from Ø18 mm to Ø14 mm and Ø12 mm defects, charts became less sparse and defect amplitudes tended to approximate noise amplitudes, being increasingly difficult to clearly detect lower diameter defects. Withal, simultaneous analysis of the charts for SNR vs. Temperature and Amplitude vs. Temperature has proven that defects of critical depth from Ø16 mm up could easily and clearly be detected at temperatures from 25 °C to 400 °C, for all given blocks.

For that reason, it was decided to apply a safety margin, declaring that the minimum defect diameter (of critical depth), from 10 mm to 30 mm nominal thickness blocks, which the prototype equipment could clearly detect was Ø16 mm, as required by *ISQ* customers.

Regarding the second category step block, A+C Scan results were properly treated (using a Gain Basis of 90 dB and the same proceedings as with the first category blocks), so that charts regarding back wall echo signal amplitude evolution along increasing temperatures, as well as SNR vs. Temperature, could be presented, and the prototype precision regarding depth discontinuities at higher thicknesses could be studied.

Fig. 69 shows an example of the A+C Scan report on the second category block at 400 °C, noting that all tests were performed using *Peak to Peak* gate algorithm, as thickness was successively changing from step to step, along with the position of each echo, (so that the first back wall echo tended to merge with the parasitic echo at 14 mm thickness). The red and orange stripes on the C-Scan represented the back wall thickness of each respective step, and the bluish/yellow stripes represented the thickness discontinuities between each step (except the first blue stripe, for the same reason as the report in Fig. 57).

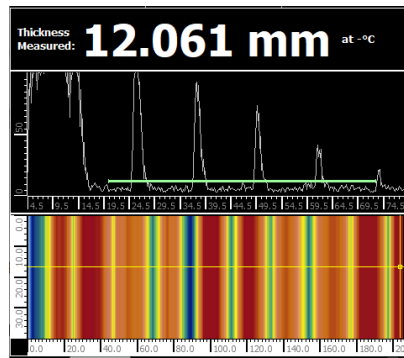


Fig. 69 - A+C Scan of 2<sup>nd</sup> category block at 400 °C using *Innerspec PowerBox H*.

The charts from Fig. 72 (in Chapter 7) show the evolution of the back wall echo amplitude along increasing temperatures for the second category step block. As could be noted, amplitudes regarding each step followed the same descending tendency as the back wall echo amplitudes of the first category blocks, generally presenting a slight slope change at 200 °C – 225 °C (near the Curie Temperature of cementite) for the same reasons previously explained with other blocks. For the sake of convenience, all steps were presented in the same plot.

In that case, only back wall echoes were analysed. Then, as there were no defects of critical depth, scattering effects were reduced, allowing the use of lower Gain values to obtain decent amplitude results which, after being reduced to the same Gain basis, led to greater back wall echo amplitudes when compared with the ones of first category blocks. Noise was also reduced by these effects, having a mean value of 5%. The amplitudes tended to increase as nominal thicknesses decreased, although it was not very significant.

For the SNR vs. Temperature study (as seen in Fig. 73, Chapter 7), the same proceedings as the previous blocks were used (Rejection Value of 9,58 dB), and the obtained results showed higher SNR values than the ones of the back wall echoes on first category blocks, ranging from 21,5 dB to almost 27,5 dB, (which was expected due to the decrease of scattering effect as already explained), while maintaining the slight descending tendency of SNR values over temperature, as seen in the previous tests (for the same reasons). Therefore, the results were more than sufficient to state that the equipment could clearly detect thickness discontinuities of 2 mm, from 12 mm to 30 mm steps, and temperatures between 25 °C and 400 °C.

Lastly, in order to better study the prototype behaviour and precision on different depth discontinuities at a lower thickness of 10 mm, A+C Scans of the third category block were analysed.

In Fig. 70, the A-Scan was showing the gate over the defect of 4 mm depth, which gave a reminiscent thickness of 6 mm. Third back wall and defect echoes were analysed in these tests

because the first two seemed to merge with parasitic echoes. In the C-Scan, the red and blue stripes represented the defect echoes (except for the first one, by the same reasons already mentioned for other blocks), and the yellow stripes represented the nominal thickness of 10 mm.

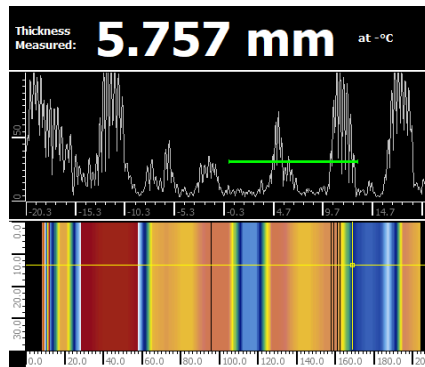


Fig. 70 - A+C Scan of 3<sup>rd</sup> category block at 100 °C using *Innerspec PowerBox H*.

The results were treated using the same procedure as with previous blocks (Gain basis of 90 dB), therefore Fig. 74 and Fig. 75 (Chapter 7) show the charts regarding Amplitude vs. Temperature and SNR evolution over increasing temperatures, respectively.

The amplitude evolution along increasing temperatures described the same behaviour as with previous blocks (a descending tendency, with a slight slope decrease after around 200 °C), for the same aforementioned reasons. But in this case, as geometric discontinuities created by the defects were not so accentuated when compared with first category blocks (the present blocks had  $\varnothing 40$  mm defects with depths of 2 mm, 3 mm and 4 mm), scattering due to this effect was reduced, therefore amplitude response was generally higher.

That also contributed to slightly higher SNR values from back wall echo in the SNR vs. Temperature chart. And generally, SNR values also followed the same tendency along increasing temperatures as the previous blocks, with noise values around 10% and exhibiting SNR values well above the required minimum of 9,58 dB. Therefore, it was evident that the equipment could also detect thickness variations of 1 mm, from 2 mm depth to 4 mm depth, in 10 mm nominal thickness block, as it detected thickness variations on the previous second category block. As the required minimum of thickness discontinuities was 4 mm at a 10 mm block, it could be stated that the equipment satisfied the desired criterion.

On the ability to inspect tubular structures, it was tested and verified at the *Non Destructive Testing Laboratory of ISQ Group* that the scanner prototype could easily be coupled and removed to Carbon Steel pipes for circumferential and axial inspections (Fig. 71, left).

Since the scanner prototype only weighted 3,1 Kg, and could easily be moved back and forth without much effort, it was comfortable enough to perform not only vertical inspections but also upside-down inspections (Fig. 71, right).



Fig. 71 - Left: *EMAT Heat Inspection* prototype on a OD 400 mm pipe. Right: *Emat Heat Inspection* prototype on upside-down test (same pipe as left image).

During validation tests, scanning times were recorded using a chronometer, giving a mean value of 10 s which, with the scanning length (that was 210 mm, due to the Aluminium profiles on top of the heating box that assured the same starting and ending point at every test) were then used to compute the scanning speed, having a mean value of 21 mm/s. That also satisfied the minimum speed requirement of 15 mm/s.

As equipment calibration would always be performed on *Non Destructive Testing Laboratory* before each industrial inspection, on-site setup time, (which consisted in taking the equipment from the travelling case, making the necessary connections, coupling the scanner in the desired structure and turning on the *PowerBox H*) wouldn't take more than 6 minutes, as it was tested. Therefore, the desired maximum setup time of 10 minutes wasn't surpassed.

Using a proper harness (as seen in Chapter 2.3), *PowerBox H* could be attached to the chest and the scanner could be transported by hand, revealing to be portable enough to be taken into spaces of difficult access.

Having performed all the required studies, conclusions could finally be drawn, to determine if the equipment met the desired requirements.

## 4. Conclusion

In the present work, the design and creation of *EMAT Heat Inspection* prototype was achieved. Its validation in laboratorial environment showed that the equipment allows corrosion mapping in Carbon Steel structures up to 400 °C.

The work was developed by *IST*, in collaboration with the *Non Destructive Testing Laboratory* of *ISQ Group*, with the intent to create a portable equipment which enabled the execution of specific corrosion mapping inspections over high temperature Carbon Steel structures on the Petrochemical Industry, in a rapid and efficient manner, thus reducing the setup and inspection times, avoiding plant shutdowns and preventing the occurrence of industrial disasters.

After proper validation tests were performed, the study of its respective results, mainly regarding signal amplitude behaviours on various kinds of defects and specimens at temperatures from 25 °C to 400 °C led to various conclusions. Remembering each customer requirement, the accomplishments were the following:

- Detect defects with minimum diameter of 16 mm and depth of 50% of the nominal specimen thickness (from 10 mm to 30 mm) up to 400 °C.

The tests using first category blocks have shown that the prototype successfully detected defects of at least Ø16 mm, on nominal thicknesses ranging between 10 mm and 30 mm, and between 25 °C and 400 °C. That kind of flaws was very similar to those of pitting corrosion defects [110], thus it can be concluded that the equipment can detect pitting corrosion flaws with the same characteristics.

- Detect thickness discontinuities of at least 4 mm depth in structures of 10 mm nominal thickness up to 400 °C.

Thickness measurement tests on the second and third category blocks led to the conclusion that the equipment not only detected thickness discontinuities of 1 mm (from 2 mm to 4 mm depth defects), in blocks of 10 mm nominal thickness, but also detected 2 mm thickness discontinuities in blocks with steps from 12 mm to 30 mm depth, between 25 °C and 400 °C, surpassing the desired requirement. That being said, evidently the equipment can be used to detect uniform corrosion or erosion corrosion defects, which usually led to thickness losses similar to those on the tested blocks [22].

- Perform circumferential and axial inspections on pipes with a minimum outer diameter of 350 mm.

As seen, the scanner was designed to perform circumferential and axial inspections on pipes tubular surfaces of minimum outer diameter of 331 mm and 104 mm respectively, and experiments on *Non Destructive Testing Laboratory* concluded that the scanner can be easily coupled to pipes.

- Perform bottom, vertical and upside-down inspections.

All validation tests were bottom inspections, and laboratory experiments on various structures have also shown that the scanner, of 3,1 Kg, was easy to move and comfortable enough to perform vertical and upside-down tests.



- The production site won't need to be shut down in order to perform the testing.

As it could inspect the desired Carbon Steel structures up to 400 °C, the production site wouldn't need to be shut down for the surfaces to cool and to perform the inspections.

- No more than 10 minutes of setup time.

Experiments on the *Non Destructive Testing Laboratory of ISQ* concluded that the setup time was around 6 minutes, well below the limit.

- Minimum scanning speed of 15 mm/s.

According to experiments, the scanning speed was around 21 mm/s, which satisfied the required minimum.

- Generate Corrosion Mapping Reports (A-Scan and C-Scan).

The A+C Scans were the basis of this equipment's corrosion mapping reports, and were available to be consulted both in *PowerBox H* and in a desktop.

- The equipment must be portable enough to be taken to spaces of difficult access.

*PowerBox H* can be harnessed to the chest and the scanner prototype can be transported by hand, making the equipment suitable to perform inspections in spaces of difficult access.

Despite the natural attenuation effects of the signals along increasing temperatures due to scattering caused by defect geometries, vibrational interactions between the travelling ultrasonic waves and the microstructures of Carbon Steel, and the different behaviour of cementite vibrational interactions with the ultrasonic waves after reaching its Curie Temperature, the developed prototype fulfilled all the customer requirements.

Its capacity to inspect, on the given conditions, flaws due to uniform corrosion and erosion corrosion, and defects of critical depth due to pitting corrosion, generating corrosion mapping reports at service temperatures up to 400 °C in a practical and reliable manner, was validated.

It was concluded that *EMAT Heat Inspection* prototype could be used to successfully inspect high temperature Carbon Steel structures of the aforementioned kind, for corrosion mapping. In fact, the equipment is the only one on the NDT market which is able to perform corrosion mapping on the given structures up to 400 °C, with lower setup times and rapid report generations.

Therefore, the developed engineering solution managed to resolve the imposed Industrial challenges, creating an equipment that can propel, in near future, a solid and competitive market offer on Corrosion Inspection Services at High Temperatures.

## 5. Marketing and suggestions for future work

The prototype equipment was ready to be used in real industrial context.

To promote *EMAT Heat Inspection* for the services it was able to perform, a marketing brochure was made, which specified the main characteristics and functionalities of the equipment prototype, as could be seen in Chapter 7. The services it could provide were then publicized amongst interested *ISQ* customers, and it was expected that the equipment would be first used in a certain company of the Petrochemical Industry in near future.

The prototype could even be furtherly used in conjunction with corrosion prediction softwares, such as *Honeywell Predict-Pipe 5.0* which was designed to accurately quantify internal corrosion in natural gas and liquid petroleum pipeline systems due to water or solids accumulation. *Predict-Pipe* could identify the pipeline segments more prone to water condensation and accumulation, as well as study the corrosion rates in onshore and offshore piping systems that normally carry natural gas with condensed water, or water and liquid hydrocarbons.

More so, it made use of Internal Corrosion Direct Assessments (according to NACE Standard Practice Documents [111][112][113]), creating structured processes that combine pre-assessment, indirect inspection, detailed examination, and post-assessment to evaluate pipeline integrity threats as a result of internal corrosion, taking in consideration factors such as water content, flow regime, liquid holdup, temperature and pressure variations [114].

That would add a major step in preventive maintenance against costly pipeline failures, creating an interface which could perform prediction studies in order to identify and quantify corrosion in the relevant pipeline environment, so that the spots of major interest on a desired structure could be easily and promptly inspected with *EMAT Heat Inspection* prototype equipment.

Lastly, if smaller defect diameters were required to be detected on the same structural and thermal conditions as in previous tests, *EMAT Heat Inspection* scanner could be adapted in order to accommodate a different probe, with a smaller coil diameter which would provide slender magnetic fields and therefore narrower, more concentrated ultrasonic beam profiles, as stated by Rueter [115], allowing for the detection of smaller defect diameters at critical depths.

## 6. References

- [1] 'BP Statistical Review of World Energy 2018', 2018.
- [2] G. Koch, J. Varney, N. Thompson, O. Moghissi, M. Gould, and J. Payer, 'International Measures of Prevention, Application, and Economics of Corrosion Technologies Study', *NACE Int.*, p. 216, 2016.
- [3] M. R. Simmons, 'Report of offshore technology conference (OTC) presentation', 2008.
- [4] Michael Baker Jr. Inc. to US Department of Transportation; Pipeline and Hazardous Materials Safety Administration; Office of Pipeline Safety; Integrity Management Program (under Delivery Order DTRS56-02-D-70036), 'Pipeline Corrosion - Final Report', 2008.
- [5] United States Department of Labour - Occupational Safety and Health Administration, 'Employer Responsibilities', [www.osha.gov](http://www.osha.gov). [Online]. Available: <https://www.osha.gov/as/opa/worker/employer-responsibility.html>. [Accessed: 16-Oct-2018].
- [6] Shell United States, 'About NORCO', [www.shell.us](http://www.shell.us). [Online]. Available: <https://www.shell.us/about-us/projects-and-locations/norco-manufacturing-complex/about-norco.html>. [Accessed: 15-Oct-2018].
- [7] The New York Times, 'Death Toll Up to 6 in Blast', [www.nytimes.com](http://www.nytimes.com). [Online]. Available: <https://www.nytimes.com/1988/05/07/us/death-toll-up-to-6-in-blast.html>. [Accessed: 15-Oct-2018].
- [8] The New York Times, 'Louisiana Refinery Explodes, Killing One Worker', [www.nytimes.com](http://www.nytimes.com). [Online]. Available: <https://www.nytimes.com/1988/05/06/us/louisiana-refinery-explodes-killing-one-worker.html>. [Accessed: 15-Oct-2018].
- [9] Linda Ashton - The Washington Post, '1 DEAD, 6 MISSING AS BLAST AT SHELL OIL REFINERY ROCKS LOUISIANA TOWN', [www.washingtonpost.com](http://www.washingtonpost.com). [Online]. Available: [https://www.washingtonpost.com/archive/politics/1988/05/06/1-dead-6-missing-as-blast-at-shell-oil-refinery-rocks-louisiana-town/a8ddcf3a-047d-4bd9-b23c-90d88a85639d/?utm\\_term=.e268a421eff3](https://www.washingtonpost.com/archive/politics/1988/05/06/1-dead-6-missing-as-blast-at-shell-oil-refinery-rocks-louisiana-town/a8ddcf3a-047d-4bd9-b23c-90d88a85639d/?utm_term=.e268a421eff3). [Accessed: 15-Oct-2018].
- [10] Occupational Safety and Health Administration, 'Inspection Detail (#100478866 - Shell Oil Company)', [www.osha.gov](http://www.osha.gov). [Online]. Available: [https://www.osha.gov/pls/imis/establishment.inspection\\_detail?id=100478866](https://www.osha.gov/pls/imis/establishment.inspection_detail?id=100478866). [Accessed: 15-Oct-2018].
- [11] Newspapers.com, 'Shell Norco Explosion', [www.newspapers.com](http://www.newspapers.com). [Online]. Available: [https://www.newspapers.com/clip/18862767/shell\\_norco\\_explosion/](https://www.newspapers.com/clip/18862767/shell_norco_explosion/). [Accessed: 15-Oct-2018].
- [12] Ben Winslow & Jacob Hancock - Deseret News, 'Refinery explosion injures 4', [www.deseretnews.com](http://www.deseretnews.com), 2009. [Online]. Available: <https://www.deseretnews.com/article/705277112/Refinery-explosion-injures-4-homes-evacuated.html>. [Accessed: 12-Oct-2018].
- [13] CSB, 'CSB Releases Analysis Showing Cause of Rupture and Hydrogen Blast in 2009 Silver Eagle Refinery Accident in Woods Cross, Utah', [www.csb.gov](http://www.csb.gov), 2014. [Online]. Available: <https://www.csb.gov/-/csb-releases-analysis-showing-cause-of-rupture-and-hydrogen-blast-in-2009-silver-eagle-refinery-accident-in-woods-cross-utah-pipe-walls-thinned-due-to-corrosion-that-went-uninspected-for-years-/>. [Accessed: 12-Oct-2018].
- [14] U.S. CSB, 'Silver Eagle Refinery Explosion Investigation : Metallurgical Analysis Silver Eagle Refinery Explosion Investigation : Metallurgical Analysis', *U. S. Chem. Saf. Hazard Investig. Board*, pp. 1–43, 2013.
- [15] Jeremy Miller - High Country News, 'The Bay Area Chevron explosion shows gaps in refinery safety', [www.hcn.org](http://www.hcn.org), 2012. [Online]. Available: <https://www.hcn.org/issues/44.15/the-recent-bay-area-chevron-explosion-shows-gaps-in-refinery-safety>. [Accessed: 12-Oct-2018].
- [16] Braden Reddall & Erwin Seba - Reuters, 'Chevron's California refinery fire contained, not out yet', [www.reuters.com](http://www.reuters.com), 2012. [Online]. Available: <https://www.reuters.com/article/us-refinery-fire-chevron-richmond/chevrons-california-refinery-fire-contained-not-out-yet-idUSBRE87602Y20120807>. [Accessed: 15-Oct-2018].
- [17] U.S. Chemical Safety and Hazard Investigation Board, 'Final Investigation Report Chevron Richmond Refinery Pipe Rupture and Fire Chevron Richmond Refinery #4 Crude Unit', 2015.
- [18] R. J. Carswell, 'High Temperature Ultrasonic Scanning', *3rd MENDT - Middle East Nondestruct. Test. Conf. Exhib.*, pp. 1–7, 2005.

- [19] A. McLay and J. Verkooijen, 'Ultrasonic inspections at elevated temperature', *18th World Conf. Nondestruct. Test.*, vol. 54, no. 6, pp. 307–309, 2012.
- [20] 'Standard Guide for Corrosion-Related Failure Analysis (ASTM Designation G161-00)', *Annu. B. ASTM Stand.*, vol. 00, no. Reapproved 2013, pp. 1–5, 2005.
- [21] K. Elayaperumal and V. Raja, *Corrosion Failures - Theory, Case Studies and Solutions*. Wiley, 2015.
- [22] E. McCafferty, *Introduction to Corrosion Science*. Springer, 2010.
- [23] Lekan Popoola et.al., 'Corrosion problems during oil and gas production and its mitigation', *Springer*, vol. 4, no. 1, p. 35, 2013.
- [24] R. Melchers, 'A Review of Trends for Corrosion Loss and Pit Depth in Longer-Term Exposures', *MDPI - Corros. Mater. Degrad.*, vol. 1, no. 1, pp. 42–58, 2018.
- [25] Fontana & Greene - NACE International, 'Eight Forms of Corrosion', [www.nace.org](http://www.nace.org), 1967. [Online]. Available: <https://www.nace.org/Corrosion-Central/Corrosion-101/Eight-Forms-of-Corrosion/>. [Accessed: 18-Oct-2018].
- [26] P. R. Roberge and R. Pierre, *Handbook of Corrosion Engineering*. 1999.
- [27] King Fahd University of Petroleum & Minerals (Saudi Arabia), 'Corrosion Engineering - Case Study 6 (Erosion Corrosion in a Reducer)', [www.faculty.kfupm.edu.sa](http://www.faculty.kfupm.edu.sa). [Online]. Available: [http://faculty.kfupm.edu.sa/ME/hussaini/Corrosion Engineering/cs-06.htm](http://faculty.kfupm.edu.sa/ME/hussaini/Corrosion%20Engineering/cs-06.htm). [Accessed: 19-Oct-2018].
- [28] Steel Data, 'Steam condensate system - Upper part of horizontal condensate pipe', [www.steeldata.info](http://www.steeldata.info). [Online]. Available: <http://www.steeldata.info/macro/demo/data/171.html>. [Accessed: 19-Oct-2018].
- [29] L. Martinez, R. Torres, J. M. Sanchez Yanez, and A. M. Vazquez, 'High Temperature Microbial Corrosion in the Condenser of a Geothermal Electric Power Unit', *Corros.* 96, 24-29 March, Denver, Color., 1996.
- [30] GFZ - German Research Centre for Geosciences (Helmholtz Centre Postdam), 'Quantification of microbial metabolic processes to enhance process understanding in terms of scaling and corrosion in geothermal plants', [www.gfz-potsdam.de](http://www.gfz-potsdam.de). [Online]. Available: <https://www.gfz-potsdam.de/en/section/geothermal-energy-systems/projects/completed-projects/miprotherm/>. [Accessed: 19-Oct-2018].
- [31] The British Institute of Non-Destructive Testing, 'In-service corrosion assessment for high-temperature plant components', 2018. [Online]. Available: <http://www.bindt.org/events/NDT-2018/in-service-corrosion-assessment-for-high-temperature-plant-components/>. [Accessed: 04-Apr-2019].
- [32] E. Bardal and J. M. Drugli, 'Corrosion Detection and Diagnosis', in *Materials Science and Engineering Vol. III*, EOLSS / UNESCO, 2009, pp. 144–165.
- [33] B. Raj, T. Jayakumar, and M. Thavasimuthu, *Practical Non-Destructive Testing*. Woodhead Publishing Ltd., 2002.
- [34] F. Pinto, J. Barata, and P. Barros, *Ensaio Não Destrutivos*. ISQ, 1992.
- [35] C. Meola, S. Boccardi, and G. M. Carlomagno, *Nondestructive Evaluation*. 2017.
- [36] American Society for Testing and Materials (ASTM), 'Standard Guide for Electromagnetic Acoustic Transducers ( EMATs ) (Designation: E 1774 - 96)', vol. 03, no. Reapproved, pp. 1–8, 2002.
- [37] S. D. Cramer and B. S. Covino, *ASM Handbook Volume 13C Corrosion: Environments and Industries*, vol. 13. 2006.
- [38] A. Kumar, T. Jayakumar, B. Raj, and K. K. Ray, 'Correlation between ultrasonic shear wave velocity and Poisson's ratio for isotropic porous materials', *J. Mater. Sci.*, vol. 43, no. 1, pp. 316–323, 2003.
- [39] IAEA, *Non-destructive Testing: A Guidebook for Industrial Management and Quality Control Personnel*, no. 9. Vienna, 1999.
- [40] 'Olympus IMS: C-Scan Mapping'. [Online]. Available: <https://www.olympus-ims.com/en/ndt-tutorials/instrumentation/cscan/>. [Accessed: 09-Apr-2019].
- [41] M. Hirao and H. Ogi, *Electromagnetic Acoustic Transducers - Noncontacting Ultrasonic Measurements using EMATs*, Springer. 2004.
- [42] R. Ribichini, F. Cegla, P. B. Nagy, and P. Cawley, 'Evaluation of electromagnetic acoustic transducer performance on steel materials', *NDT&E Int.* 45 32–38, vol. 1335, no. 1, pp. 785–

- 792, 2011.
- [43] R. B. Thompson, 'Electromagnetic Acoustic Transducers (EMATs)', in *The Evaluation of Materials and Structures by Quantitative Ultrasonics*, Springer, Ed. Vienna: J. D. Achenbach, 1993.
- [44] 'NDT Resource Center - Basic Principles of Eddy Current Inspection'. [Online]. Available: <https://www.nde-ed.org/EducationResources/CommunityCollege/EddyCurrents/Introduction/IntroductiontoET.htm>. [Accessed: 31-Jul-2018].
- [45] J. García-Martín, J. Gómez-Gil, and E. Vázquez-Sánchez, 'Non-Destructive Techniques Based on Eddy Current Testing', *Sensors*, vol. 11, no. 3, pp. 2525–2565, 2011.
- [46] J. C. Duke Jr, *Acousto - Ultrasonics: Theory and Application*. Springer, 1988.
- [47] G. Hayward *et al.*, *Ultrasonic Measurement Methods*, vol. XIX. Academic Press, 1990.
- [48] D. Leitão and L. Silva, 'Quality and Technology Global Network: EMAT – Electromagnetic Acoustic Transducers (Internal Doc)', pp. 1–28.
- [49] S. Huang and S. Wang, *New Technologies in Electromagnetic Non-destructive Testing*. 2016.
- [50] S. E. Burrows, Y. Fan, and S. Dixon, 'High temperature thickness measurements of stainless steel and low carbon steel using electromagnetic acoustic transducers', *NDT E Int.*, vol. 68, pp. 73–77, 2014.
- [51] 'Innerspec PowerBox H - Operations Manual'. pp. 1–51, 2008.
- [52] 'NDT Supply - High Temperature Couplants'. [Online]. Available: <https://ndtsupply.com/ultrasonic-flaw-detection/couplants/high-temperature-couplants.html>. [Accessed: 08-Apr-2019].
- [53] W. P. Mason and R. N. Thurtson, 'Physical Acoustics', vol. 14, Elsevier, 1979.
- [54] K. Manjula, K. Vijayarekha, and B. Venkatraman, 'Noise reduction in ultrasonic signals for identification of weld defects: A review', *Res. J. Appl. Sci. Eng. Technol.*, vol. 6, no. 24, pp. 4595–4601, 2013.
- [55] O. Trushkevych, Y. Fan, R. Perry, and R. S. Edwards, 'Magnetic phase transitions in Gd<sub>64</sub>Sc<sub>36</sub> studied using non-contact ultrasonics', *J. Phys. D. Appl. Phys.*, vol. 46, no. 10, p. 105005, 2013.
- [56] SuvenduLenka - NDT Training Consultancy and Inspection Services Pvt.Ltd, *Pipeline inspection using EMAT*. 2015.
- [57] Silverwing, 'RMS2 – High Speed, Remote Access C-Scan Defect Detection and Corrosion Mapping System (brochure)'. pp. 0–5.
- [58] Silverwing publication at NDT News (ndt.org), 'RMS2 - High Speed Ultrasonic Corrosion Mapping', [www.ndt.org](http://www.ndt.org), 2012. [Online]. Available: <https://www.ndt.org/news.asp?ObjectID=47719>. [Accessed: 25-Oct-2018].
- [59] Silverwing, 'RMS2 - Automated Ultrasonic Corrosion Mapping Scanner', [www.silverwingndt.com](http://www.silverwingndt.com). [Online]. Available: <https://www.silverwingndt.com/products/rms2-ultrasonic-corrosion-mapping/>. [Accessed: 24-Oct-2018].
- [60] American Society for Testing and Materials (ASTM), 'ASTM G 46 – 94: Standard Guide for Examination and Evaluation of Pitting Corrosion', vol. 94, no. Reapproved 2005. pp. 1–8, 2006.
- [61] I. Chattoraj, 'Industrial Corrosion Failure - Case Studies', pp. 24–36, 1997.
- [62] Phoenix ISL, 'High Temperature Twin Crystal Compression Wave Transducers', [www.phoenixisl.com](http://www.phoenixisl.com). [Online]. Available: <https://www.phoenixisl.com/transducers-wedges/compression-wave-transducers/high-temperature-twin-crystal-compression-wave-transducers>. [Accessed: 29-Oct-2018].
- [63] 'TWI - What are the advantages of using twin crystal ultrasonic probes?' [Online]. Available: <https://www.twi-global.com/technical-knowledge/faqs/faq-what-are-the-advantages-of-using-twin-crystal-ultrasonic-probes>. [Accessed: 10-Apr-2019].
- [64] Innerpsec, 'Standard Sensors & Accessories for EMAT Applications'. pp. 1–209, 2017.
- [65] K. Lee and T. Nelligan, 'The use of magnetostrictive EMAT transducers on oxide scaled boiler tubes', *16th WCNDT 2004 - World Conf. NDT*, pp. 1–5, 2004.
- [66] M. Hirao and H. Ogi, *EMATs For Science and Industry: noncontact ultrasonic measurement*. 2003.
- [67] 'Innerspec - Portable instrument: body harness for PowerBox H'. [Online]. Available: <https://www.innerspec.com/portable/standard-sensors-and-accessories/emat/body-harness/>.

- [Accessed: 10-Apr-2019].
- [68] E. Technologies, 'Eddyfi Catalog - Pulsed Eddy Current (PEC) Probes'.
- [69] Eddyfi, 'Eddyfi Lyft - Specification Sheet'.
- [70] 'Subsea & Offshore Service Magazine - Eddyfi Technologies will be exhibiting at Subsea Expo 2018'. [Online]. Available: <https://www.sosmagazine.biz/single-post/2017/12/11/Eddyfi-Technologies-will-be-exhibiting-at-Subsea-Expo-2018-showcasing-TSC's-latest-developments-in-subsea-ACFM-inspection-technologies-alongside-Eddyfi's-Lyft-system-for-underwater-a>. [Accessed: 10-Apr-2019].
- [71] 'Eddyfi - Eddy Current Testing'. [Online]. Available: <https://www.eddyfi.com/technologies/eddy-current-testing-ect/>. [Accessed: 10-Apr-2019].
- [72] A. Sophian, G. Tian, and M. Fan, 'Pulsed Eddy Current Non-destructive Testing and Evaluation: A Review', *Chinese J. Mech. Eng. (English Ed.)*, vol. 30, no. 3, pp. 500–514, 2017.
- [73] 'East Tennessee State University - Tap and Drill Sizes Chart'. [Online]. Available: [http://faculty.etsu.edu/hemphill/tap\\_drill.htm](http://faculty.etsu.edu/hemphill/tap_drill.htm). [Accessed: 11-Apr-2019].
- [74] Innerpsec, 'Standard Sensors & Accessories for EMAT Applications', pp. 1–209, 2017.
- [75] 'Hengstler - RI32 Incremental RI32-O/360AR.14KB'. [Online]. Available: [https://www.hengstler.de/en/s\\_c10030217i4625/Rotary\\_encoders/Incremental\\_rotary\\_encoder\\_s/ICURO\\_RI32/RI32\\_Incremental\\_RI32-O/360AR.14KB/527179.html](https://www.hengstler.de/en/s_c10030217i4625/Rotary_encoders/Incremental_rotary_encoder_s/ICURO_RI32/RI32_Incremental_RI32-O/360AR.14KB/527179.html). [Accessed: 12-Apr-2019].
- [76] M. I. Afandi, H. Adinanta, A. Setiono, Qomaruddin, and B. Widiyatmoko, 'High resolution extensometer based on optical encoder for measurement of small landslide displacements', *J. Phys. Conf. Ser.*, vol. 985, no. 1, pp. 0–6, 2018.
- [77] 'Lapp - Product Information Unitronic FD CP plus'.
- [78] 'Alpha Wire - 5473C cable'. [Online]. Available: <http://www.alphawire.com/Products/Cable/Alpha-Essentials/Communication-and-Control-Cable/5473C?popup=pdf>. [Accessed: 12-Apr-2019].
- [79] P. K. Levangie and C. C. Norkin, *Joint Structure and Function: A Comprehensive Analysis*. F.A. Davis, 2011.
- [80] M. W. Marzke, 'Precision grips, hand morphology, and tools', *Am. J. Phys. Anthropol.*, vol. 102, no. 1, pp. 91–110, 1997.
- [81] M. Nordin and V. H. Frankel, *Basic Biomechanics of the Musculoskeletal System*. Lippincott Williams & Wilkins, 2001.
- [82] T. L. Kivell, 'Evidence in hand: Recent discoveries and the early evolution of human manual manipulation', *Philos. Trans. R. Soc. B Biol. Sci.*, vol. 370, no. 1682, 2015.
- [83] 'Curbell Plastics - PEEK High Temp, Chemical Resistance'. [Online]. Available: <https://www.curbellplastics.com/Research-Solutions/Materials/PEEK>. [Accessed: 13-Apr-2019].
- [84] 'Curbell Plastics - PTFE Soft, Low Friction Fluoropolymer'. [Online]. Available: <https://www.curbellplastics.com/Research-Solutions/Materials/PTFE>. [Accessed: 13-Apr-2019].
- [85] 'Understanding PEEK Plastic Price Per Pound - Reading Plastic'. [Online]. Available: <http://readingplastic.com/peek-plastic-price-per-pound/>. [Accessed: 13-Apr-2019].
- [86] 'PTFE Production, Price and Market Demand'. [Online]. Available: <https://www.plasticsinsight.com/resin-intelligence/resin-prices/ptfe-polytetrafluoroethylene/>. [Accessed: 13-Apr-2019].
- [87] 'Goodfellow - Stainless Steel AISI 304 online catalog'. [Online]. Available: <http://www.goodfellow.com/A/Stainless-Steel-AISI-304.html>. [Accessed: 15-Apr-2019].
- [88] 'WS Hampshire Inc. - Teflon Property Chart'.
- [89] 'Polymer Properties Database - FKM'. [Online]. Available: <http://polymerdatabase.com/Elastomers/FKM.html>. [Accessed: 14-Apr-2019].
- [90] 'M.J. Branco - Indústria de Mecânica Fina, Lda.' [Online]. Available: <http://www.mjbranco.pt/>. [Accessed: 15-Apr-2019].
- [91] 'Lasindustria'. [Online]. Available: <https://www.lasindustria.pt/>. [Accessed: 15-Apr-2019].
- [92] 'ETOPi'. [Online]. Available: <https://etopi.pt/>. [Accessed: 15-Apr-2019].
- [93] 'Sove'. [Online]. Available: <http://www.sove.pt/>. [Accessed: 15-Apr-2019].
- [94] 'LEMO Connectors'. [Online]. Available: <https://www.lemo.com/en>. [Accessed: 15-Apr-2019].
- [95] 'RS Components'. [Online]. Available: <https://pt.rs-online.com/web/>. [Accessed: 16-Apr-2019].

- [96] 'Techflex'. [Online]. Available: <https://www.techflex.com/>. [Accessed: 16-Apr-2019].
- [97] ASTM, 'ASTM A 967-96: Standard Specification for Chemical Passivation Treatments for Stainless Steel Parts', vol. 2001. 2001.
- [98] 'RF Caixas'. [Online]. Available: [www.caixas.net](http://www.caixas.net). [Accessed: 16-Apr-2019].
- [99] 'Morgan Advanced Materials - Data sheet Superwool Boards', 2017.
- [100] P. J. Howard, D. C. Copley, and R. S. Gilmore, 'A Signal-To-Noise Ratio Comparison of Ultrasonic Transducers for C-Scan Imaging in Titanium', *Rev. Prog. Quant. Nondestruct. Eval.*, vol. 14, no. 1, pp. 2113–2120, 2012.
- [101] G. S. Darbari, R. P. Singh, and G. S. Verma, 'Ultrasonic attenuation in carbon steel and stainless steel at elevated temperatures', *J. Appl. Phys.*, vol. 39, no. 5, pp. 2238–2245, 1968.
- [102] E. Papadakis, 'Ultrasonic Attenuation in Hot Specimens by the Momentary Contact Method with Pressure Coupling', *J. Acoust. Soc. Am.*, vol. 50, no. 1A, pp. 115–115, 2005.
- [103] P. Edmonds, *Methods of Experimental Physics Vol. 19 - Ultrasonics*. Academic Press, 1981.
- [104] T. Wan, T. Naoe, T. Wakui, M. Futakawa, H. Obayashi, and T. Sasa, 'Effects of Grain Size on Ultrasonic Attenuation in Type 316L Stainless Steel', *MDPI Mater. J.*, vol. 10, no. 7, p. 17, 2017.
- [105] R. C. Tripathi and G. S. Verma, 'Ultrasonic attenuation as function of temperature in a 1% carbon steel', *J. Acoust. Soc. Am.*, vol. 53, no. 5, pp. 1344–1345, 2005.
- [106] W. D. Callister and J. Wiley, 'Materials Science: an Introduction', p. 990, 2014.
- [107] N. Lunn, S. Dixon, and M. D. G. Potter, 'High temperature EMAT design for scanning or fixed point operation on magnetite coated steel', *NDT E Int.*, vol. 89, no. October 2016, pp. 74–80, 2017.
- [108] L. Mauger *et al.*, 'Phonons and elasticity of cementite through the Curie temperature', *Phys. Rev. B*, vol. 95, no. 2, pp. 1–9, 2017.
- [109] ISQ, 'ISQ Group Technical Procedure (Internal Report)'. 2019.
- [110] M. Baker, 'Pipeline Corrosion Report', no. November, pp. 1–78, 2008.
- [111] NACE, 'NACE SP0206-2016: Internal Corrosion Direct Assessment Methodology for Pipelines Carrying Normally Dry Natural Gas (DG-ICDA)'. 2016.
- [112] NACE, 'NACE SP0208-2008: Internal Corrosion Direct Assessment Methodology for Liquid Petroleum Pipelines'. 2008.
- [113] NACE, 'NACE SP0110-2018: Wet Gas Internal Corrosion Direct Assessment Methodology for Pipelines'. 2018.
- [114] Honeywell, 'Honeywell Predict-Pipe 5.0: Assessment of Internal Corrosion in Pipeline Systems'. [Online]. Available: <https://www.honeywellprocess.com/library/marketing/notes/Honeywell-Predict-Pipe-5.0.pdf>. [Accessed: 27-Apr-2019].
- [115] D. Rueter, 'Induction coil as a non-contacting ultrasound transmitter and detector: Modeling of magnetic fields for improving the performance', *Ultrasonics*, vol. 65, pp. 200–210, 2016.
- [116] P. Yvon, *Structural Materials for Generation IV Nuclear Reactors*. Woodhead Publishing Ltd., 2017.
- [117] M. Stewart and O. T. Lewis, *Heat Exchanger Equipment Field Manual*. Elsevier, 2013.
- [118] M. Stewart and O. T. Lewis, *Pressure Vessels Field Manual*. Elsevier, 2013.
- [119] ASME, 'ASME B31G - Manual for Determining the Remaining Strength of Corroded Pipelines', vol. 2012. 1991.

## 7. Annexes

### 7.1. Results from validation tests

Defect Temperature	Ø12 mm	Ø14 mm	Ø16 mm	Ø18 mm
25	-16,67 %	50 %	-31,25 %	5,56 %
50	66,67 %	50 %	31,25 %	22,22 %
75	66,67 %	-28,57 %	12,5 %	11,11 %
100	58,33 %	21,43 %	-31,25 %	0 %
125	66,67 %	42,86 %	0 %	-5,56 %
150	66,67 %	42,86 %	18,75 %	44,44 %
175	41,67 %	21,43 %	0 %	5,56 %
200	75 %	-28,57 %	-12,5 %	27,78 %
225	58,33 %	-35,71 %	0 %	0 %
250	41,67 %	42,86 %	75 %	-5,56 %
275	41,67 %	-21,43 %	0 %	16,67 %
300	-8,33 %	14,29 %	-6,25 %	-5,56 %
325	50 %	-35,71 %	6,25 %	-5,56 %
350	-8,33 %	35,71 %	6,25 %	27,78 %
375	16,67 %	14,29 %	12,5 %	0 %
400	-16,67 %	57,14 %	50 %	-44,44 %

Table 4 - Percentual share over the real defect diameter of the difference between obtained and real flaw diameter for 15 mm block of the first category.

Defect Temperature	Ø12 mm	Ø14 mm	Ø16 mm	Ø18 mm
25	75 %	42,86 %	31,25 %	0 %
50	66,67 %	64,29 %	31,25 %	44,44 %
75	50 %	57,14 %	56,25 %	11,11 %
100	75 %	21,43 %	37,5 %	27,78 %
125	66,67 %	50 %	31,25 %	44,44 %
150	58,33 %	21,43 %	43,75 %	33,33 %
175	66,67 %	71,43 %	50 %	0 %
200	25 %	0 %	43,75 %	27,78 %
225	0 %	14,29 %	12,5 %	61,11 %
250	66,67 %	35,71 %	25 %	55,55 %
275	8,33 %	0 %	37,5 %	11,11 %
300	66,67 %	28,57 %	31,25 %	33,33 %
325	41,67 %	92,86 %	0 %	16,67 %
350	16,67 %	7,14 %	50 %	16,67 %
375	66,67 %	64,29 %	43,75 %	38,89 %
400	25 %	57,14 %	18,75 %	11,11 %

Table 5 - Percentual share over the real defect diameter of the difference between obtained and real flaw diameter for 20 mm block of the first category.



Defect Temperature	Ø12 mm	Ø14 mm	Ø16 mm	Ø18 mm
25	50 %	50 %	-25 %	-5,56 %
50	66,67 %	28,57 %	-37,5 %	-5,55 %
75	50 %	50 %	-25 %	-11,11 %
100	66,67 %	0 %	-12,5 %	-5,56 %
125	16,67 %	28,57 %	-12,5 %	0 %
150	50 %	7,14 %	-18,75 %	0 %
175	75 %	0 %	-6,25 %	-16,67 %
200	41,67 %	35,71 %	12,5 %	-11,11 %
225	66,67 %	7,14 %	6,25 %	-11,11 %
250	66,67 %	7,14 %	-18,75 %	-11,11 %
275	41,67 %	57,14 %	-6,25 %	0 %
300	50 %	64,29 %	-12,5 %	-11,11 %
325	25 %	0 %	-18,75 %	-22,22 %
350	66,67 %	28,57 %	12,5 %	11,11 %
375	16,67 %	-14,29 %	-6,25 %	0 %
400	58,33 %	28,57 %	-25 %	11,11 %

Table 6 - Percentual share over the real defect diameter of the difference between obtained and real flaw diameter for 25 mm block of the first category.

Defect Temperature	Ø12 mm	Ø14 mm	Ø16 mm	Ø18 mm
25	8,33 %	42,86 %	37,5 %	33,33 %
50	33,33 %	35,71 %	12,5 %	22,22 %
75	41,67 %	-50 %	43,75 %	55,56 %
100	16,67 %	0 %	31,25 %	16,67 %
125	50 %	57,14 %	31,25 %	50 %
150	25 %	28,57 %	-37,5 %	27,78 %
175	8,33 %	0 %	43,75 %	33,33 %
200	-8,33 %	78,57 %	-12,5 %	33,33 %
225	-16,67 %	35,71 %	31,25 %	33,33 %
250	-16,67 %	-21,43 %	62,5 %	22,22 %
275	-33,33 %	-28,57 %	81,25 %	22,22 %
300	-8,33 %	14,29 %	81,25 %	44,44 %
325	33,33 %	-14,29 %	62,5 %	5,56 %
350	0 %	0 %	87,5 %	-33,33 %
375	-33,33 %	-21,43 %	31,25 %	-22,22 %
400	25 %	50 %	37,5 %	-16,67 %

Table 7 - Percentual share over the real defect diameter of the difference between obtained and real flaw diameter for 25 mm block of the first category.

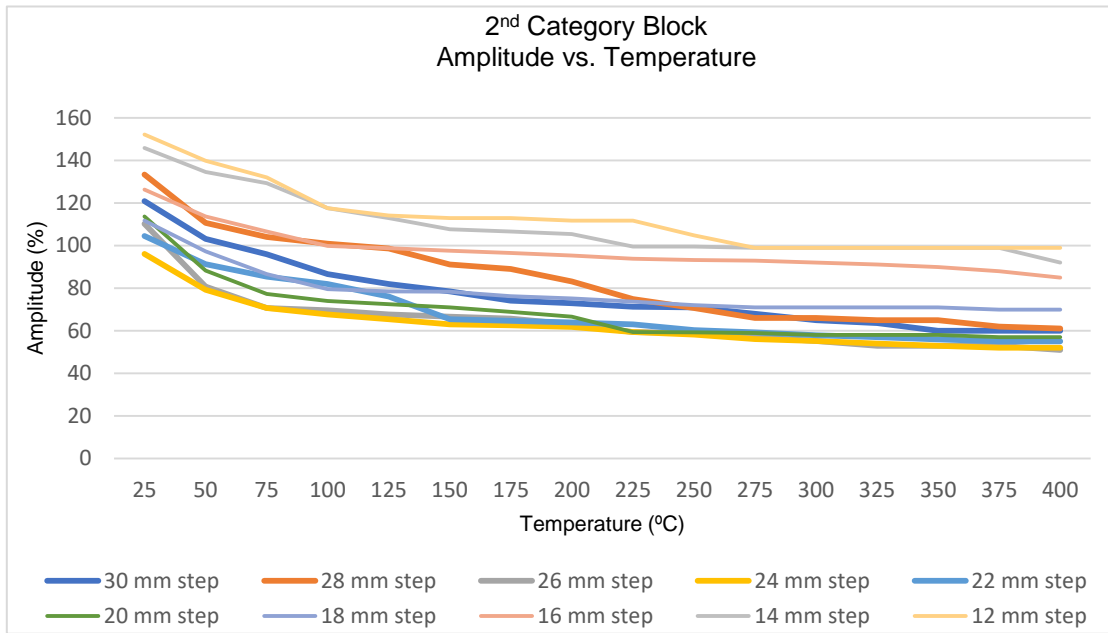


Fig. 72 - Amplitude vs. Temperature for the 2<sup>nd</sup> category block back wall echo.

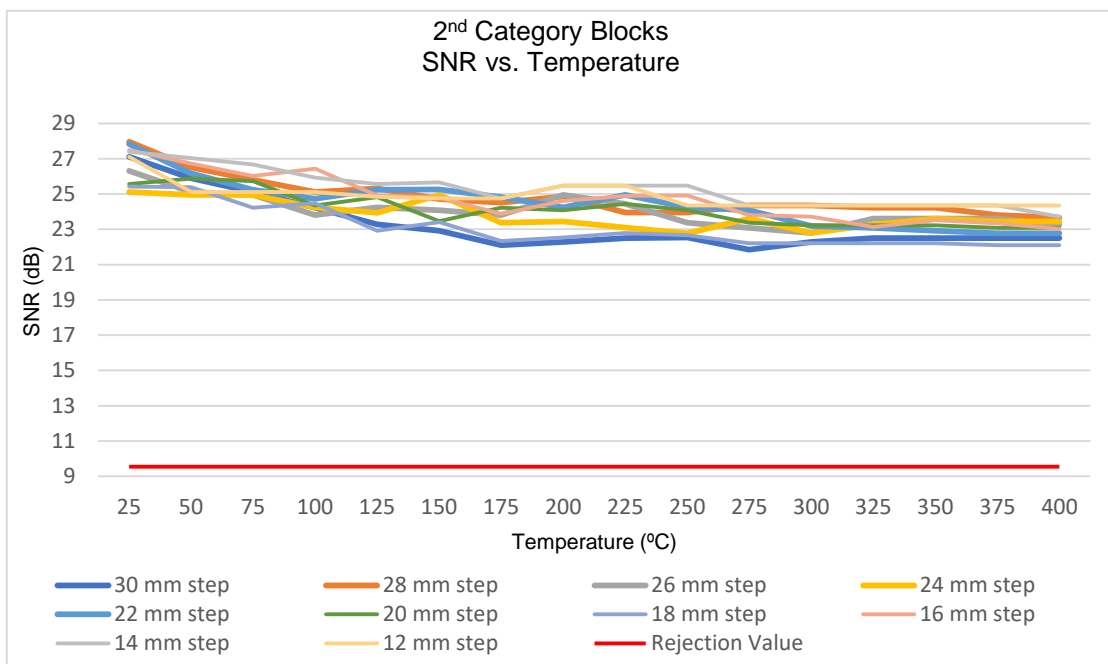


Fig. 73 - SNR vs. Temperature for the 2<sup>nd</sup> category block back wall echo.

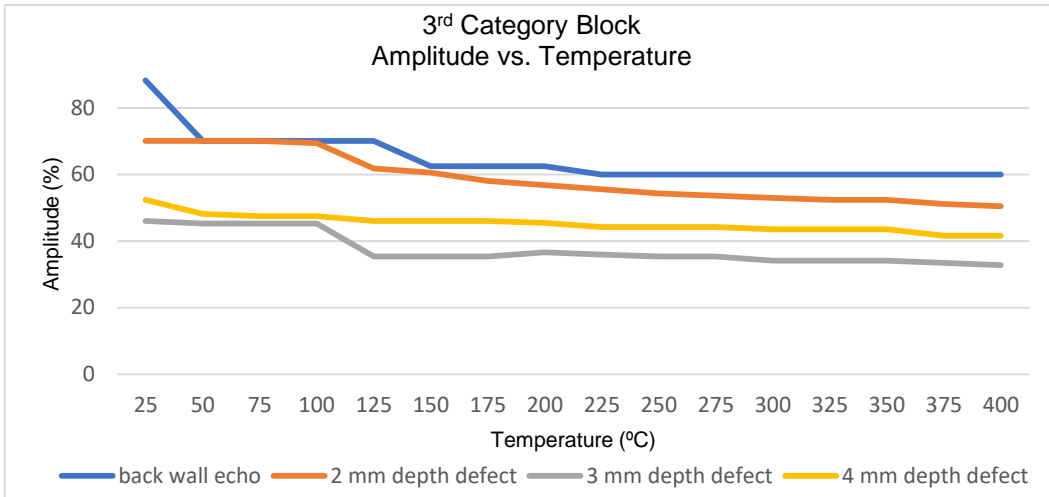


Fig. 74 - Amplitude vs. Temperature for 3<sup>rd</sup> category block defects and back wall echo.

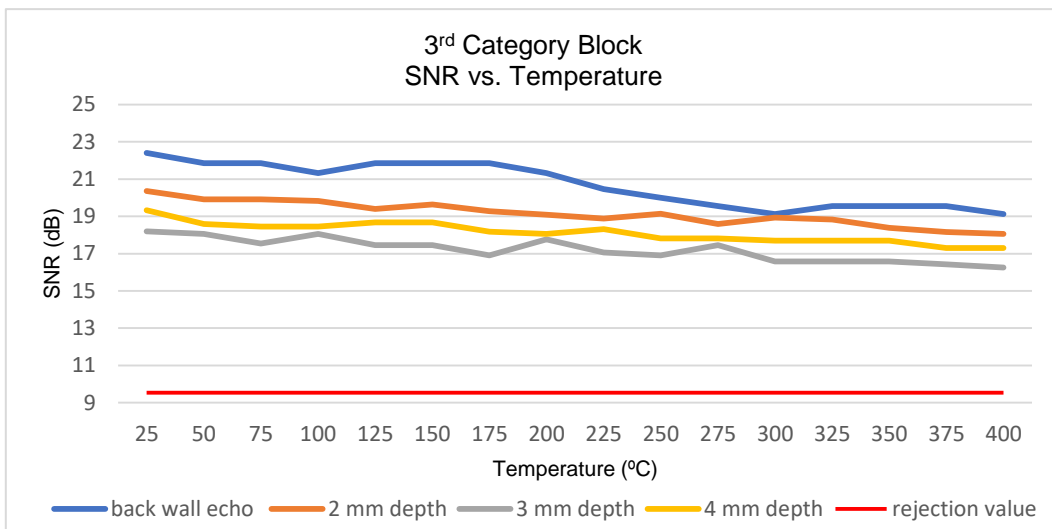
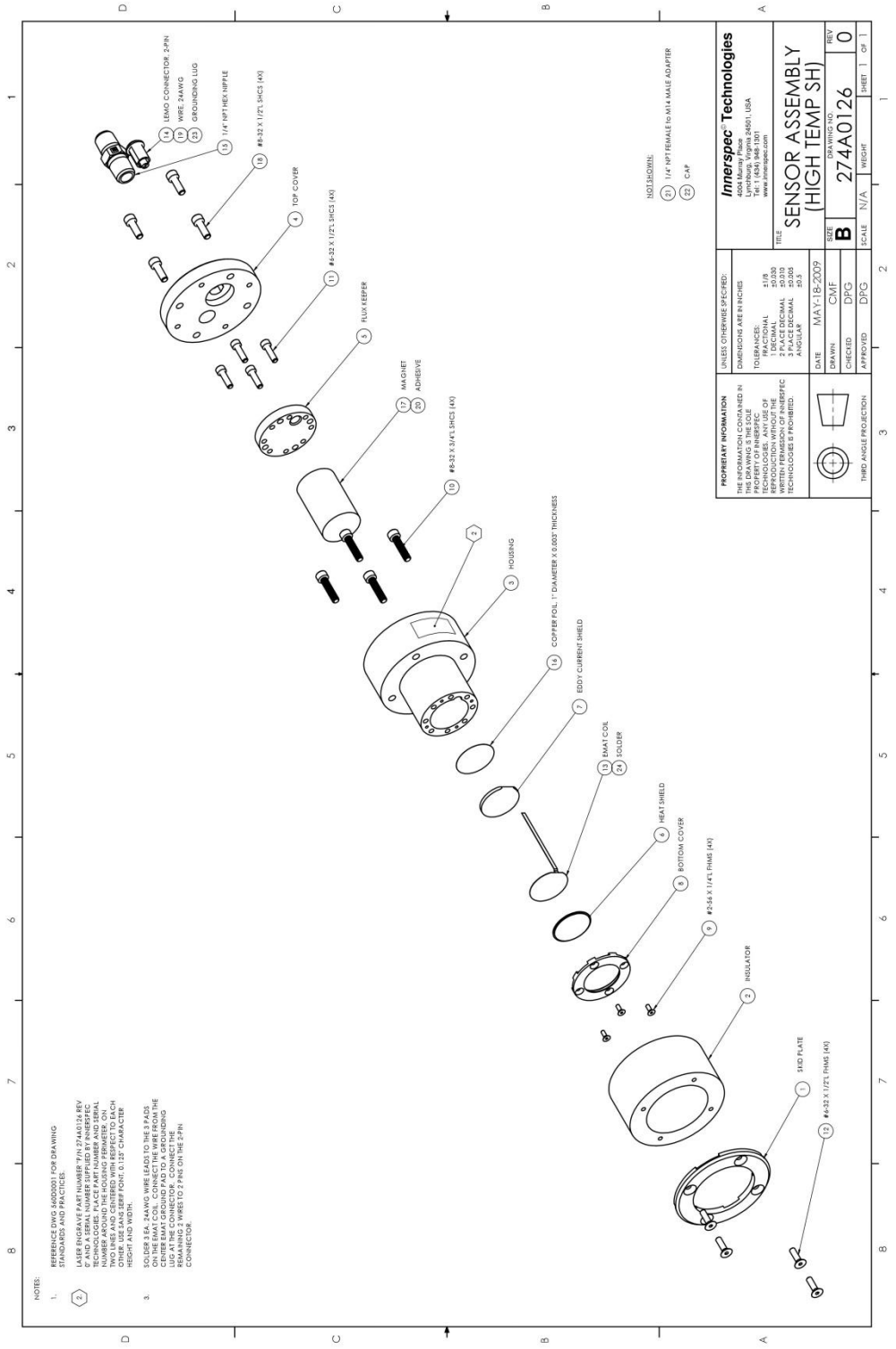


Fig. 75 - SNR vs. Temperature for 3<sup>rd</sup> category block defects and back wall echo.

## 7.2. Innerspec probe Exploded View



### 7.3. EMAT Heat Inspection Marketing Brochure



## ISQ AT A GLANCE

### YOUR TECHNOLOGY AND INNOVATION INTERFACE IN PORTUGAL

ISQ delivers **value** through integrated and innovative solutions that support you **managing risk**, **improve performance** and **boost competitiveness**.

Present in 14 countries and with more than 50 years of history, ISQ is the **one-stop shop** for engineering, inspection, testing and training services

Covering the entire project lifecycle, ISQ assists you to **align your business goals** with applicable regulations and standards while meeting your targets for quality, safety, environmental and social responsibility.

#### ISQ NUMBERS

<b>1.400</b> EMPLOYEES	<b>16</b> ACCREDITED LABORATORIES	<b>5</b> BRANCHES AND OFFICES IN PORTUGAL
<b>+500</b> INTERNATIONAL R&D PROJECTS	<b>14</b> COUNTRIES	<b>16</b> AFFILIATES IN PORTUGAL
<b>+17.000</b> TRAINING COURSES (1994 TO 2017)	<b>+200.000</b> TRAINEES (1994 TO 2017)	

#### ISQ WORLDWIDE



#### OUR EXPERTISES



#### SECTORS

#### TRANSVERSAL AREAS



[www.isqgroup.com](http://www.isqgroup.com)

# PORTABLE IN-SERVICE INSPECTION SOLUTION FOR HIGH-TEMPERATURE CORROSION DETECTION





## CHALLENGE

Carbon Steel industrial equipments operating at high temperatures such as pipelines, boilers and KO drums are prone to be degraded by corrosion effects. Typically, these equipments are inspected during the factories shut down and their maintenance is confined to the shut down period. The non-planned shut downs, due to equipments fails, represents a very high cost to the factories and must be avoided with a better knowledge of the equipments and a consequent better shut down planning. This only can be achieved with an in-service non-destructive inspection.

## SOLUTIONS

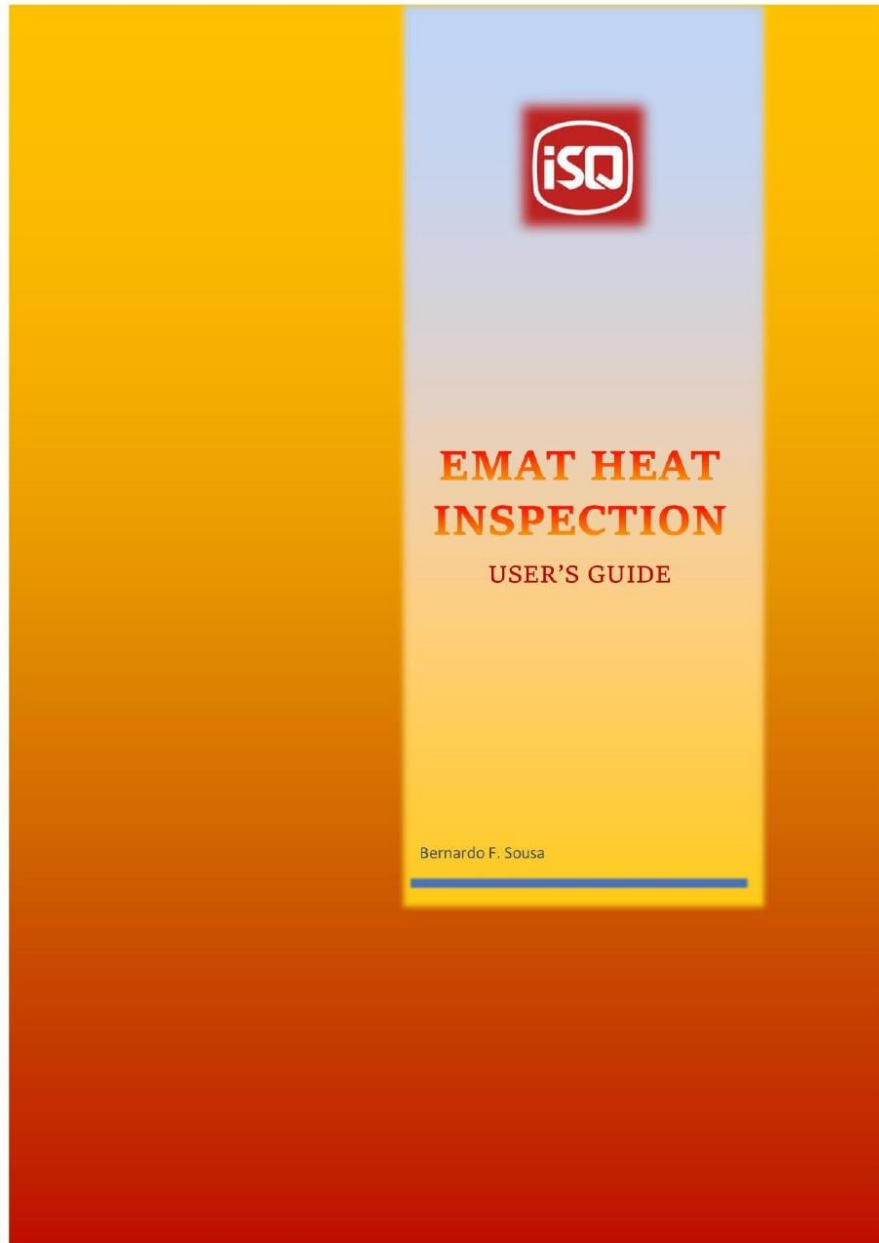
**IN-SERVICE NON-DESTRUCTIVE INSPECTION OF INDUSTRIAL EQUIPMENTS AT HIGH TEMPERATURE, PRESENTING RESULTS IN A RAPID AND EFFICIENT MANNER**

This inspection solution presents a portable scanner and a dedicated digital interface, allowing lower setup time and rapid test of high temperature Carbon Steel equipments, for corrosion mapping in both flat and tubular surfaces, and bottom, vertical or upside-down positions. It can inspect a wide range of industrial critical equipments, at full work, without the need to shut down the factory. Thereby, with the generated reports is possible to understand the condition of the equipments and better prepare the shut downs.

 <b>400°C</b> TEMPERATURES LEVEL	 MATERIALS Carbon Steel	<b>10 to 30mm</b> THICKNESS	<b>tubular minimum Ø 350mm to flat surfaces</b> INDUSTRIAL EQUIPMENTS GEOMETRY	<b>Ø 16mm minimum defect detection</b> CORROSION MAPPING
<b>BENEFITS</b>	EARLY DETECTION OF DEFECTS WHILE EQUIPMENT IS IN FULL OPERATION	DECREASE THE DOWNTIME OF CRITICAL EQUIPMENT	SAVE TIME AND RESPECTIVE COSTS OF MAINTENANCE STOPPAGE	PORTABLE SOLUTION, WITH LOW SETUP TIME

[www.isqgroup.com](http://www.isqgroup.com) • [comercial@isq.pt](mailto:comercial@isq.pt)

#### 7.4. *EMAT Heat Inspection User's Guide*



## Contents

1.	Introduction .....	1
2.	Safety precautions.....	1
	Rechargeable Li-Ion battery.....	1
	PowerBox H unit.....	2
	AC adapter .....	2
	Scanner.....	2
3.	The Scanner.....	3
	The Probe.....	4
	The Encoder.....	3
	Structure.....	3
	Cables and Connections.....	4
4.	The <i>PowerBoX H</i> .....	5
	Li-Ion battery .....	5
	AC adapter .....	5
	Cables and Connections.....	5
5.	Setting the equipment.....	6
6.	Calibration .....	7
	Calibrating the probe .....	7
	Calibrating the encoder.....	7
7.	Packing the units.....	8
8.	Performing an Inspection.....	8
9.	Report generation.....	9
10.	Maintenance.....	9
	Scanner Maintenance.....	9
	PowerBox H Maintenance .....	10



## 1. Introduction

*EMAT Heat Inspection* is a solution developed by *IST* in partnership with the *Non Destructive Testing Laboratory of ISQ (Instituto de Soldadura e Qualidade)* which aimed to create a product that is portable, ergonomic and of easy use, to perform corrosion mapping inspections on high temperature Carbon Steel surfaces with lower setup times, higher cadencies and quicker report generations, in order to enable *ISQ* to render inspection services which better serve the needs of its customers, in a time when simple and efficient options are highly praised.

The intent of this guide is to instruct the user on how to handle the equipment that constitutes *EMAT Heat Inspection* on a safe and most productive way.









*EMAT Heat Inspection* is roughly formed by two separate units:

- The scanner, which is used to perform corrosion inspections in high temperature surfaces due to its EMAT probe and an incremental rotary encoder.
- The *PowerBox H*, a computer-like portable device which transmits desired signals to the scanner probe for it to pulse a certain wave mode in the inspected surface. *PowerBox H* also receives, treats and saves the signals from the scanner (probe & encoder).

This guide also shows how to pack the units in its travel case, how to set up and calibrate the probe and the encoder, how to operate the equipment during an inspection and also how to perform regular maintenance actions on the equipment in order to maintain its proper functioning.

## 2. Safety precautions





In order to prevent the user from injury and damaging the equipment, the following explanations use various symbols, which meanings are the following:

	Forbidden action		Action that must be done
	Risk of fire		Touching is prohibited
	Risk of electric shock		Potentially hazardous situation
	Disassembling is forbidden		Exposure to water is forbidden

### Rechargeable Li-Ion battery



#### Rechargeable Li-Ion battery

	<p>Never use the battery for any purpose other than recharging your <i>PowerBox H</i> unit. DO NOT recharge or leave the battery near a fire, heaters, direct sunlight or locations with temperatures above 80°C. Disobeying could result in excessive current or abnormal chemical reaction in the battery. DO NOT use if it is damaged or leaking. DO NOT solder any connections to the battery. DO NOT directly connect the battery to a household electrical supply.</p>
	<p>DO NOT insert the battery into a different <i>PowerBox H</i>, or a different battery into your <i>PowerBox H</i> unit. Disobeying may result in fire or damage. DO NOT allow wires or other metal objects to come into contact with the terminals of the rechargeable battery, as they could cause an electrical short and overheating of the aforementioned metal objects.</p>
	DO NOT allow the battery to come in contact or be immersed in water.
	DO NOT disassemble, modify or attempt to repair the battery.

**PowerBox H unit**



**PowerBox H unit**

	<p>Never use the <i>PowerBox H</i> for any purpose other than performing ultrasonic inspections. DO NOT use if it is damaged. DO NOT solder any connections to the <i>PowerBox H</i>. In order to prevent damage, do not drop or hit the <i>PowerBox H</i>. DO NOT try to make any connection in the <i>PowerBox H</i> which is not compatible with the original ones.</p>
	DO NOT allow the <i>PowerBox H</i> to come in contact or be immersed in water.
	DO NOT disassemble, modify or attempt to repair the <i>PowerBox H</i> .

**AC adapter**



**AC adapter**

	<p>DO NOT use if it is damaged. DO NOT solder any connections to the adapter. In order to prevent damage, do not drop or hit the adapter. Never use an adapter which is not the original one. If the original is damaged, contact an official supplier. DO NOT connect the adapter to other products. DO NOT use the adapter in places with high humidity, such as bathrooms.</p>
	DO NOT allow the adapter to come in contact or be immersed in water.
	DO NOT disassemble, modify or attempt to repair the adapter.
	Make sure the plug is fully inserted into the power outlet.

**Scanner**



**Scanner**

	<p>DO NOT use the scanner for any purposes other than performing ultrasonic inspections. DO NOT use if it is damaged. DO NOT solder any connections to the scanner. In order to prevent damage, do not drop or hit the scanner. DO NOT connect the scanner to other products other than the <i>PowerBox H</i>, and a pressurized air source. DO NOT try to make any connection in the scanner which is not compatible with the original ones. ALWAYS perform the inspections with pressurized air in surfaces of temperature above 200°C. DO NOT perform inspections at surfaces of temperature above 200°C if ambient pressure is above 2 bar. DO NOT let the scanner in contact with surfaces of temperature above 450°C during more than 30 seconds. DO NOT let the scanner in contact with surfaces of temperature above 650°C.</p>
	DO NOT allow the scanner to come in contact or be immersed in water.
	DO NOT disassemble, modify or attempt to repair the scanner while using it.
	DO NOT touch the scanner with bare hands while or immediately after performing an inspection in surfaces of temperature above 25°C, otherwise severe burning damage could happen. Always use proper gloves while inspecting with the scanner and allow it to cool before touching it with bare hands.
	DO NOT operate the scanner with wet hands.

### 3. The Scanner

The scanner is mainly constituted of 4 parts – the probe, the encoder, the structure which holds them both and a set of cables which make the connection between the probe/encoder to the *PowerBox H*, and allow the entrance of air to the scanner and the probe in particular

Each part will followingly be described in more detail.

#### The Probe

The probe is an *High Temperature SH Spiral Sensor*, developed by *Innerspec*. Its function is to send electromagnetic pulses (which are generated by synergy of a polarized magnet and a spiral coil in which passes electric current) to the inspected material that are converted to ultrasonic waves when it passes the material surface. Then, the probe receives the ultrasonic waves that come back from the material and are converted to electromagnetic pulses by the probe.

The next table shows the probe's technical data:

Part Number	274A0126
Sensor Type	SH Lorentz Permanent Magnet
Temperature Ranges	From 25°C to 200 °C – Continuous with air From 200°C to 450°C – Continuous with air at 2 bar From 450°C to 650°C – 30 seconds with air
Connector	2 Pin <i>Lemo</i> 0B
Coil Geometry	Spiral
Coil OD	18.25 mm
Coil ID	6.25 mm
Dimensions	D 64 mm x H 70 mm
Air coupling	¼" NPT
Anchor Points	M5 threaded holes
Best frequency for transmitted signal	3800 kHz

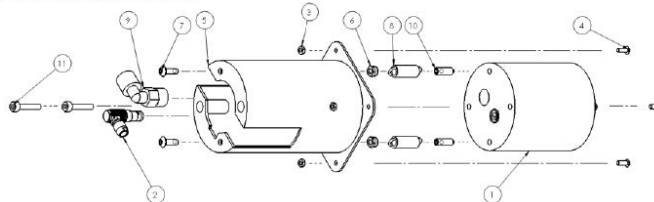
#### The Encoder

The encoder is of the incremental rotary type, with reference *R132-O/360AR.14KB*, and was manufactured by *Hengstler*. After being properly calibrated, each fraction of rotation the encoder performs is converted to linear position when it is connected to the *PowerBox H*. Its main characteristics are:

- Low torque
- IP40 Protection rating
- Operating temperature: -10 to +60°C
- Shaft diameter: 5 mm
- Push-pull short circuit proof output
- Cable radial type of connection
- Maximum Voltage: 5 V
- Maximum Rotation Speed: 6000 rpm

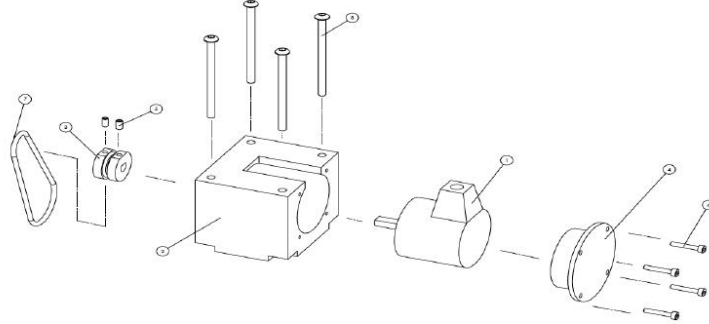
#### Structure

The probe is held by a Stainless Steel retention cup, to which it gets suspended due to a set of traction springs, as can be seen on the following exploded view:



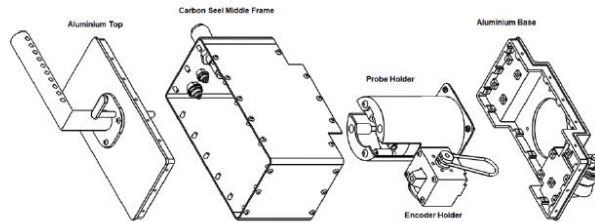
Being 1 – probe; 2 – *Lemo FGG.0B.302.CLAD52Z* plug; 3 – nuts to fix the cup; 4 – screws to fix the cup; 5 – cup; 6 – washers to fix the springs; 7 – screws to fix the springs; 9 – L air connector; 10 – set screws to fix the springs; 11 – long screws.

The encoder fits in a Teflon holder which protects it from higher temperatures, and has a plug attached to its spindle in which a Viton O-Ring (19,5 x 2 mm) is held. This O-Ring is high-temperature resistant (max. 230°C) and is held both in the encoder, and in the scanner front wheel which is above the encoder.



Where 1 – encoder; 2 – encoder holder; 3 – plug which fits in the encoder spindle; 4 – encoder holder lid; 5 – screws to fix the plug; 6 – screws to fix the encoder lid; 7 – O-Ring; 8 – screws to fix the encoder holder.

All these are assembled in the scanner by a mixed structure of an Aluminium base, a Stainless Steel middle frame and an Aluminum top and handler, as generally explained on the scheme below:



## Cables and Connections

Inside the scanner is a set of cables to connect the probe and encoder to their respective panel connectors, and a punctured air hose to bring in pressurized air to both the scanner interior and the probe.

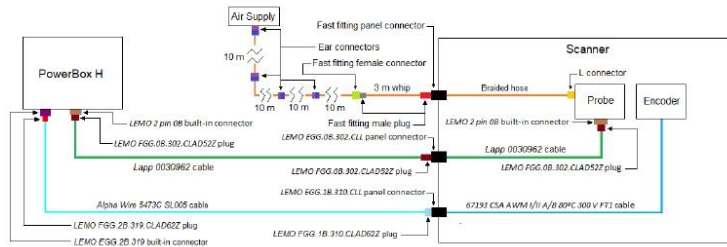
The mentioned electrical connectors and plugs are all manufactured by *Lemo*. Unless referenced, all hoses diameters are internal.

The scanner cable is a *Lapp 0030962* (1 pair of wires, S/UTP shielding, exterior layer of polyurethane, 250 V, pyro-retardant), and has a 2 pin *FGG.0B.302.CLAD52Z* plug in one of its endings. It plugs to a 2 pin *0B* connector which is embedded in the probe. The other ending is a 2 female *EGG.0B.302.CLL* panel connector, attached to the scanner frame.

The encoder has a built-in cable (*67193 CSA AWM VII A/B 80°C 300 V FT1*, of 4 wires), which connects to a 10 female *EGG.1B.310.CLL* panel connector embedded on the scanner frame. The four wires of the encoder cable are soldered to the panel connector according to the following scheme:



There is also a braided air hose, in which one ending simply connects to a rapid fitting metal connector (Ø8 mm, 1/8" thread), built in the scanner frame, and the other simply connects to a male L air metal connector of mechanical fitting (Ø8 mm, NPT thread) which is on the probe. The hose is punctured on purpose, for it can provide pressurized air to cool the probe, and also to the scanner interior. The following picture shows a schematic of all the connections:



The air hose set is composed by:

- A braided Ø12 mm (outer diameter), 3 m whip, with a fast fitting metal male plug (Ø8 mm, DN9) on both endings. One connects to a female fast fitting metal connector (Ø8 mm, DN9) embedded in the scanner frame; the other connects to a female fast fitting metal connector (Ø8 mm, DN9) embedded in a Ø18 mm (outer diameter) braided 10 m hose.
- A Ø18 mm (outer diameter) braided 10 m hose (mentioned in the above paragraph) with a female fast fitting metal connector (Ø8 mm, DN9) on one ending and an ear metal connector on the other.
- 3 sets of Ø18 mm (outer diameter) braided 10 m hose with an ear metal connector on both endings. One of the hoses connects to the aforementioned 10 m hose and another connects to an industrial pressurized air source.

#### 4. PowerBox H

*PowerBox H* is a portable computer-like device, developed by *Innerspec* for ultrasonic inspections. It enables the user to configure it in great variety of ways to perform many kinds of applications, but for sake of pragmatism, this guide will approach only the configuration used in *EMAT Heat Inspection*.

The *PowerBox H* has a transmitter function - one can choose the desired setup to generate different pulses and wave modes in the EMAT probe. It also has a receiving function - it receives the electric signals from the probe regarding echoes of the ultrasonic transmission, and electric signals from the encoder regarding position. With this data it treats and generates the results in a A + C Scan (A-Scan shows Amplitude vs. Time and C-Scan shows the position in a grid-based color code where each colour corresponds to a certain A-Scan Amplitude) in which the user can interpret and observe for the presence of defects within the inspected material.

#### Li-Ion battery

*PowerBox H* has a Li-Ion battery which in full charge enables 4 - 5 h of inspection before recharging, taking just 2 h to be charged.

The Li-Ion battery should be in full charge before going to perform a given inspection with the equipment.

#### AC adapter

In order to recharge the battery, an AC adapter to connect the *PowerBox H* to a power source is provided.

Although possible, it is not advisable to operate the *PowerBox H* without the Li-Ion battery and only with the AC adapter plugged.

#### Cables and Connections

The mentioned electrical connectors and plugs are all manufactured by *Lemo*. Unless referenced, all hoses diameters are internal.

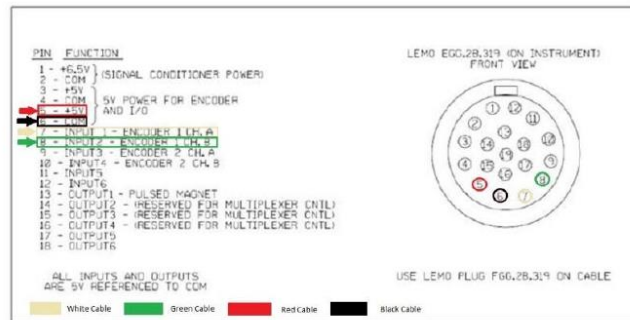
The probe cable is a *Lapp 0030962* (1 pair of wires, S/UTP shielding, exterior layer in polyurethane, 250 V, pyro-retardant), and has a 2 pin *FGG.0B.302.CLAD52Z* plug in one of its endings which connects to the 2 pin *0B T/R* (Transmitter/Receiver, that is the used mode that was described on the previous paragraph) connector which is embedded in the *PowerBox H*.

The other ending of the probe cable has also a 2 pin *FGG.0B.302.CLAD52Z* plug which connects to the 2 female *EGG.0B.302.CLL* panel connector, attached to the scanner middle frame.

The encoder cable is an *Alpha Wire 5473C SL005* (3 pairs of wires, F/UTP shielding, outer layer in PVC, 300 V, pyroretardant). One of its endings has a 19 pin *FGG.2B.319.CLAD62Z* plug, which connects to the 19 female *EGG.2B.319 I/O* connector embedded on the *PowerBox H*. The other ending has a 10 pin *FGG.1B.310.CLAD62Z* plug, which connects to the 10 female *EGG.1B.310.CLL* panel connector embedded on one of the scanner frames.

See scheme in Chapter 3 for more information on connections.

The pinout scheme for 19 pin *FGG.2B.319.CLAD62Z* plug is the following:



The probe cable, encoder cable and air whip form a couple surrounded by a 2 m heat resistant sleeve (*Insultherm Ultraflex Pro Ø38,1mm*) inside which is also a 1 m steel cable which connects to the *PowerBox H* and to the scanner through its respective cable holders. The objective of this steel cable is to prevent the electrical connectors to stress out. The assembly of cables referenced in this paragraph is therefore referred as umbilical cord.

## 5. Setting the equipment

Before doing any kind of calibration, a base of settings needs to be established in the *PowerBox H*, having it connected to the scanner. This will depend on various factors, including the material, its depth, etc., but a common configuration for a Carbon Steel 10 mm block is the one which will be furtherly described.

First, make sure the Li-Ion battery is charged and insert it on the *PowerBox H*.

Now one can turn the *PowerBox H* on (keep pressing the "POWER" button until the screen lights on). Wait for it to fully load in.

It is advised to save everything on a SD card. In order to do that, insert an SD card on the *PowerBox H*, and when necessary press "Save" and perform the setup saving. Some functions, like "Record", save data automatically to a certain directory. In order to choose where to place the saved files, go to "System" and choose from "Record Media".

Then open the setup configuration *TM\_MC\_SH\_1\_50mm.cfg* (toggle "OPEN", and go to "Setups"). Now this will be configured for the 10 mm Carbon Steel block.

*Duration* – is the duration when the magnet is on (suggested value is 120  $\mu$ s).

*Voltage* – is the transmit voltage (1200 Vpp is full power).

*Burst Frequency* – is the frequency of the transmitted signal (3800 kHz is the optimum value for the probe).

*Number of Cycles* – is the number of cycles per burst (leave at 1.0).

*Set PRF* – is the theoretical Pulse Repetition Frequency (suggested value is 100 Hz, because above this there are no changes on the signal, as it depends on the probe's characteristics, so the PRF maximum for this probe should be around 100 Hz).

*RX Delay* – sets the time space which will be omitted in the A-Scan (for example, if 8  $\mu$ s is set, the A-Scan will omit the first 8  $\mu$ s of the chart, being good to eliminate parasitic ramp-up echoes, although the usage of RX Delay in order to omit these echoes or not will be left to the user's discretion).

*RX Gain* – is the echo gain (values vary with temperature and test specimen, but a common value could be around 90 dB).

*Initial Mag Delay* – time to enable the magnet, to ramp up the magnetic field (suggested value is 5  $\mu$ s).

*Data Window* – the same as *DAQ Range* (is the range of the A-Scan time axis, suggested value is 40  $\mu$ s).

*Coincidence* – represents an algorithm to prevent the influence of external noise on the signal (suggested value is 5).

*Average* – represents an algorithm that makes the average of various signals along a certain time frame, and presents the averaged signal in the A-Scan (suggested value is 16).

*Gate 2* – is the only one that should be turned on (start, range and threshold are left to the user's discretion).

On *Gate 2*, select the "..." on Menu.

Untick "Track Back wall" and "Circle Tracking gate". The algorithm used in "Mode / Algo" depends on the user's preference, although it is suggested to choose between "Peak to Peak" or "First Peak". When using "Peak to Peak", the gate detects the two highest values within its time range (so the gate threshold has no influence when using this algorithm) and

presents the distance between those two. When using "First Peak", the gate detects the first peak within its range which crosses the threshold, and calculates its relative distance to the scan origin (which is the inspected material's surface).

*DAQ Range* – is the range of the A-Scan time axis (suggested value is 40  $\mu$ s).

*Sampling Frequency* – is the sampling frequency of the received signal (suggested value is 50 MHz considering the dimensions of the probe's coil).

*Probe Zero* – adjusts probe time offset due to electronic delays (suggested value is 0  $\mu$ s).

*Axis 1 (Start/Stop/Pitch)* – when performing a C-Scan, it is mandatory that this option is enabled for the encoder to record (fill the "Start" and "Stop" with the desired values of the inspection length, for example, if in a 1000 mm tube you want to inspect between 100 mm and 300 mm, put 100 mm on "Start" and 300 mm on "Stop"; suggested Pitch value for this encoder is between 0,5 and 1); as this equipment only works in linear scanner movements (Axis 1), Axis 2 "Start" should be 0, "Stop" and "Pitch" should have the same value as the inspected width.

Make sure "Views" is on "50% A+C Scan", and the following fields are ticked: "Thickness Measurement", "H Ruler", "V Ruler", "Rectification", "DAC". If using C-Scan, make sure C-Scan Content is on "TOF" and Measurement Bar is on "Active View".

After this configuration one can now start to perform proper calibrations on the probe and encoder.

## 6. Calibration

Before performing any inspection, the scanner and encoder need to be properly calibrated. This section will explain how it could be done. Make sure proper configuration like the one presented on chapter 5 was previously done.

Use the SD card for savings as in Chapter 5.

Make the proper connections between the *PowerBox H* and the scanner before starting.

### Calibrating the probe

The scanner calibration for inspection on high temperature surfaces will obviously depend on the temperature of the surface to be inspected. For this, one can use the heating box and calibration blocks properly created for this purpose, following these steps:

- Put the desired calibration block on top of the heating box.
- Turn on the heating box and wait until the block reaches the desired temperature (regulate the power potentiometer and use the thermocouple to check the block's temperature).
- Depending on the temperature, use high temperature gloves, plug the air connection to the scanner and turn the pressurized air on.
- When it reaches the desired temperature, put the scanner on top of the block. Press "Play" on the *PowerBox H*. Depending on the mode used ("First Peak" or "Peak to Peak") configure the gate accordingly.
- Now, on the *PowerBox H*, choose "Calibrate Velocity".
- Untick "Temperature Ref", set the block's depth (10 mm) and click "Add". If it is a Carbon Steel block, depending on the temperature it should be around 3.3 mm/ $\mu$ s for 25°C and 3 mm/ $\mu$ s for 400°C. If the calibrated velocity or the thickness value is not according to expected, click "Clear", set the depth again and click "Add" (if "First Peak" is being used, it's necessary to calibrate in more than one point – apply the same procedure for the first point, then move the scanner to another point and do the same as with the first one; if any value is wrong, click "Clear All" and start again).
- If the calibration is correct, click "OK".
- Save your changes.

The probe calibration is complete.

### Calibrating the encoder

To calibrate the encoder it is necessary to do the following:

- Choose a plain, smooth and clean surface.
- Measure and mark a desired distance on the surface (for example, 500 mm – mark the 0 and the 500 mm)
- At *PowerBox H*, tick the "Encoder" option on Trigger Source. Fill the distance on "Encoders Calibration" (first section, because this equipment only works with Axis 1).
- Place the probe center on the 0 mark of the calibration surface, then press "Play" on the *PowerBox*.
- Move the scanner linearly until the center of the probe reaches the desired mark (500 mm), then press "Set".
- Save the changes.

The encoder is now calibrated.

## 7. Packing the units

The EMAT Heat Inspection units are transported in a 63 cm x 50 cm x 31 cm hardcase with foamed interior, according to the following presentation:



Being:

1. Scanner
2. *PowerBox H*
3. SD card box (with SD card included)
4. Umbilical cord with
  - a. Scanner cable
  - b. Encoder cable
  - c. Air whip (3 m)
  - d. Protective steel cable

One should maintain the same disposition as presented when packing the units in the hardcase.

When travelling, it should not be put below excessive weights (i.e. 60 Kg or above), and along with the case there should be the set of four 10 m braided hoses as described in Chapter 3, in order to make the necessary air connections on the inspection site.

## 8. Performing an Inspection

Before going and inspect a certain piece, one must first calibrate the equipment using a proper calibration block, of the same material, thickness and temperature of the piece to be inspected (see Chapter 6).

First thing to do is to take the scanner, *PowerBox H* and the umbilical chord off the case, and perform the necessary connections (turn the cooling air on if necessary). Secondly, one should turn on the *PowerBox H* and load the respective setup (see Chapter 5).

Take the SD card off its case and insert in the *PowerBox H*. Set the saving directory as in Chapter 5.

Wear high temperature gloves if necessary.

Then, the scanner should be placed on top of the inspected piece, with the probe center above the point to start the inspection. Don't forget to set the distance of inspection on "Stop" in "Encoder Sequence", "Axis 1" (as explained in Chapter 5) and to perform the inspection in "50% A+C Scan" ("Display", then "Screen Layout", and finally "Views").

Push the presser down, for the probe to be pushed down and make contact with the inspected piece surface.

Press "Record", on the *PowerBox H* (having the *PowerBox H* paused, press and hold "Play", for five seconds or until a red dot keeps blinking on the top right corner of the screen, then release).

The inspection can be performed with one hand on the scanner, and another on the *PowerBox H*, as seen:



Perform the inspection, and when the probe center reaches the desired distance, press "Pause" on the *PowerBox H*. Scanning data was automatically recorded.



The recorded data can easily be accessed on site. One can simply press "Open", and then "Recordings" to choose the desired recording.

After the inspection is done, one should turn off the *PowerBox H*, recover the SD card and put it back in its box, and finally unpack the equipment back to its original disposition in the case.

Please allow the scanner to cool before handling it or packing it in the case.

## 9. Report generation

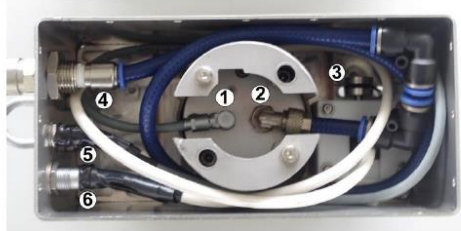
When with a PC, one can simply insert the SD card with the recorded inspections and run the program *PowerBox H PC Viewer* by *Innerspec*. Then by pressing "Ctrl + O" and navigating to the SD card directory, one can open the desired recorded inspection and analyze it (the user interface is similar as in *PowerBox H*). This program makes the user able to see the data recordings just as with the actual *PowerBox H*.

## 10. Maintenance

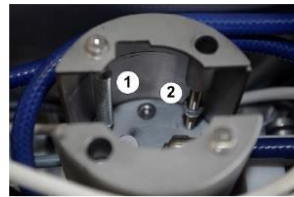
### Scanner Maintenance

Some items of the scanner are prone to be damaged by long term exposure to high temperatures.

The scanner top should be correctly disassembled as shown:



Being: 1 – *Lemo* probe connector; 2 – air probe connector; 3 – encoder O-ring; 4 – air panel connector; 5 – *Lemo* probe panel connector; 6 – *Lemo* encoder panel connector.



Where 1 – probe traction spring; 2 – probe long screw.

The item most prone to be damaged is the Viton O-Ring, which can degrade in temperatures above 230 °C. When this happens one should remove it by unscrewing the scanner top, and replace the O-Ring. Pick the O-Ring by the top and by the bottom and remove it. Then, put the new O-Ring by the same way.

One should check the O-Ring after each inspection.

The wheels roller bearings are also prone to degradation, thus they should also be replaced as follows - remove the wheel support, remove the retention rings and push the roller bearings out. Then, insert the new roller bearings and perform the inverse procedure.

If the encoder connection gets damaged, one can solder it using the pinout schemes presented in Chapter 3 and Chapter 4.

If the probe connection gets damaged, it can be easily soldered as there is no specific scheme for that particular 2 pin connection.

On the eventuality of the traction springs getting damaged, one can unscrew the scanner top and probe retention cup, and with the aid of a hook, one can take the springs out and replace for new ones, assembling everything back in the end:

If the high temperature shield gets damaged, one should adopt similar procedures to remove the probe, in order to replace the shield.

And everything should be assembled back together.

This is how one should remove the items more prone to damage.

## PowerBox H Maintenance

*PowerBox H* also needs regular updates, which can be downloaded by contacting an *Innerspec* official supplier and following this procedure:

The instrument's software is designed to be easily updated by the user. After receiving the new .upd file from Innerspec Technologies, follow these instructions carefully:



- Copy the firmware update (.UPD file) into the root (main) directory of the USB drive provided with the unit, or on a USB drive from an approved vendor. See section 6.3 for details.
- Connect AC Power Supply to instrument. Only perform updates when the instrument is connected with the external power supply.
- Plug the USB drive (use micro USB adapter included with the equipment if needed) into the mini USB port, and turn the instrument ON.
- When the Innerspec logo splash screen shows up, hold down the left arrow button in the keypad to bring up the Main Update menu.
- In the Main Update menu, navigate to the "Install Update" option using the scroll wheel, and select it by pressing the OK button.
- A file menu opens up with all the available files in the different storage media. Select USB media, and highlight the correct software update file. Press SEL in the keypad to navigate to the "Install Update" button in the GUI. Start installation by selecting "Install Update".
- Each update file may also contain some important messages about the update file.
- The installation takes a few minutes, and should end with a message reporting success. Turn OFF the device by pressing the power button once.
- Turn ON the device again and enter the update menu by keeping the left arrow button pressed.
- Select the "Uninstall Application" menu option. This opens up another file menu with a single entry - "PowerBox-H". Press SEL in the keypad to navigate to the "Uninstall" button in the GUI. Press OK after selecting "Uninstall".
- Go back to the Main Update menu using the "MENU" button in the GUI.
- Select "Install Cartridge" menu option and press OK. This step installs the software application for the cartridge. At the end of this step, a "Done" message appears along with a "Start Application" button.
- The software is fully updated. You may start the application or turn OFF the device.

If there is some technical malfunctioning with the *PowerBox H*, please contact an *Innerspec* official representative.